Quasi-near field terahertz spectroscopy

Proefschrift

ter verkrijging van de graad van doctor
aan de Technische Universiteit Delft,
op gezag van de Rector Magnificus Prof. ir. K. C. A. M. Luyben,
voorzitter van het College voor Promoties,
in het openbaar te verdedigen op

woensdag 27 januari 2010 om 12:30 uur

door

Reshmi CHAKKITTAKANDY

Master of Technology (Applied Optics)
Indian Institute of Technology, Delhi, India
geboren te Melady, India

Dit proefschrift is goedgekeurd door de promotor:
Prof. dr. P. C. M. Planken

Samenstelling promotiecommissie:

Rector Magnificus,	voorzitter
Prof. dr. P. C. M. Planken,	Technische Universiteit Delft, promotor
Prof. dr. H. P. Urbach,	Technische Universiteit Delft
Prof. dr. ir. A. Gisolf,	Technische Universiteit Delft
Prof. dr. W. J. van der Zande,	Radboud Universiteit Nijmegen
Prof. dr. H. J. Bakker,	FOM Institute, AMOLF, Amsterdam
Dr. ir. A. J. L. Adam,	Technische Universiteit Delft
Ir. J. A. W. M. Corver,	IMA Edwards Freeze Drying Solutions, Dongen
Prof. dr. ir. P. Kruit,	Technische Universiteit Delft, reservelid

This research was supported by the research program of the " Stichting voor Fundamenteel Onderzoek der Materie (FOM) ", which is financially supported by the " De Nederlandse Organisatie voor Wetenschappelijk Onderzoek (NWO)."

ISBN 978-90-78314-13-4

Printed in The Netherlands by Ipskamp Drukkers.

Contents

1 Introduction

This chapter gives an overview of terahertz (THz) spectroscopy and some other spectroscopic techniques in general. We will the discuss basics of terahertz radiation and various mechanisms to generate THz radiation. After short descriptions of certain important spectroscopic techniques used for material characterization, we will discuss THz time-domain spectroscopy (THz-TDS) and its advantages over other techniques, such as Fourier-transform spectroscopy (FTS) and Raman spectroscopy. The chapter concludes with a description on how this thesis is organized.

1.1 Motivation

THz technology is very attractive, from the point of view of industries as diverse as the semiconductor industry [1–4], medical industry [5, 6], manufacturing industry, space and defense industry [7–9]. The invention of high power sources and more sensitive detectors has opened up a plethora of applications such as, tomographic imaging [3, 10–12], label-free genetic analysis [13–16], and chemical and biological sensing [6, 17–20].

Among the various applications of THz technology, THz imaging applications have received a lot of interest. The most prominent advantage that THz imaging offers is the ability of THz radiation to penetrate a wide range of materials: paper, wood, plastics, fabric, ceramics, semiconduc-

tors, and many others that are often opaque to visible and near-infrared (NIR) radiation. The THz photon energy is roughly six orders of magnitude smaller than that of an X-ray photon making THz imaging very attractive for imaging of biological specimens, as it does not cause any detectable damage to the specimen. Contrary to X-rays, T-rays as they are sometimes called, constitute non-ionizing radiation. In Fig. 1.1, some examples of THz images recorded in Delft University of Technology are shown.

One of the primary motivations for the development of THz technology is its potential to extract material properties that cannot be measured or not easily be measured by other techniques [21, 22]. Terahertz spectroscopy allows a material's far-infrared optical properties to be determined as a function of frequency. This information can yield insight into material characteristics, such as, for example, carrier density or presence of THz absorbing phonons, for a wide range of applications. In the past, astronomy and space research have been the drivers for THz research [23–25]. THz spectroscopy has been used by chemists and astronomers in the spectral characterization of the rotational and vibrational resonances, and thermal emission lines of simple molecules [26].

Another exciting application of THz-TDS, as described in this thesis, is the identification of polymorphs [27]. Polymorphism is very common in pharmaceutical products. Drug manufacturing is a complicated process which involves several steps. Every single step in the manufacturing process should be approved by the Unites states Food and Drug Administration (FDA). Quality tests are done on the finished product and if it does not meet the quality standards, the whole batch is discarded. If the end product does not meet the quality standards, it is hard to tell which process parameter is to blame. Recently the FDA started a new initiative, called process analytical technology (PAT). In the PAT initiative, analytical tools are used during every step of the manufacturing process of a drug, to provide the manufacturer with real-time information about the state of the product. Different optical techniques are used as tools for PAT such as, infrared spectroscopy, Raman spectroscopy, X-ray diffraction, and recently, THz-TDS. No single technique is sufficient to monitor the quality of the product and each technique has its own advantages and disadvantages. The identification of polymorphs, present in pharmaceutical products, with THz-TDS as described in Chapter 5 of this thesis, makes THz-TDS a very attractive PAT tool.

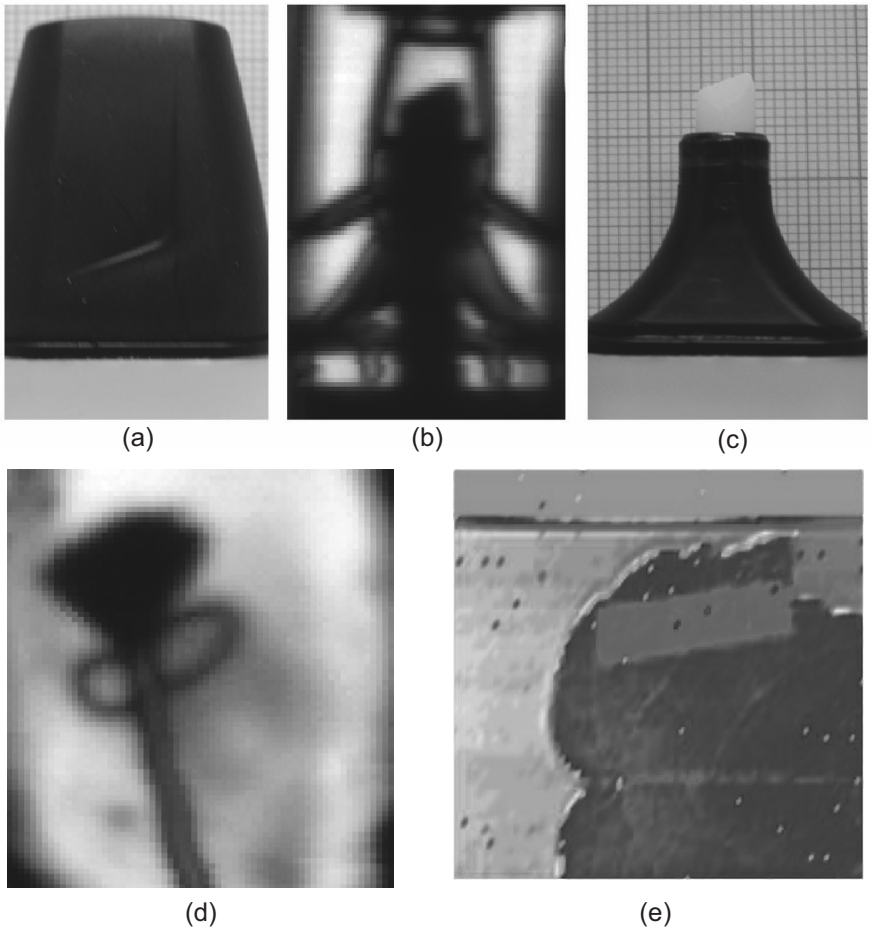

Figure 1.1: Examples of THz transmission imaging. (a) Optical image of a marker pen. (b) THz image of the same marker pen with cap on. THz image reveals the inside without opening the cap. (c) Optical image of the same marker pen with cap off. (d) THz image of a ”Kindersurprise” egg taken without opening the egg, revealing what is inside the egg. (e) THz phase image of a leaf at 1.55 THz. The dark blue color indicate the high absorption of THz radiation by the leaf water content.

1.2 Spectroscopic techniques for material characterization

There exist different spectroscopic techniques to study materials and their interaction with electro-magnetic radiation. Some commonly used spectroscopic techniques are, microwave spectroscopy [28,29], infrared spectroscopy, Raman spectroscopy [30], NMR spectroscopy, X-ray spectroscopy, Fourier transform spectroscopy (FTS) and terahertz spectroscopy [31].

The energies associated with the transitions between the rotational energy levels of molecules lie in the microwave and terahertz region. Rotational spectroscopy in the microwave region has been carried out for more than 60 years and a wealth of literature is available on this subject [32]. Rotational spectroscopy, gives information about the molecular structure and rotational states of a molecule. For example, linear polyatomic molecules, such as carbonyl sulphide (OCS), have large moments of inertia, which give rise to rotational transitions in the microwave region [33]. As the molecules get bigger with more atoms per molecule, the absorption spectra become more complicated.

Apart from rotational motions, there exist vibrational and rotational-vibrational motions of molecules. The transitions between the vibrational states of molecules in general, lie in the mid-infrared part of the electromagnetic spectrum. Every molecule has its distinct vibrational spectrum and for this reason the vibrational spectrum of a molecule is called the vibrational fingerprint of a molecule [34–36]. Infrared and Raman spectra are used to study these vibrational modes of the individual atomic bonds in a molecule [37, 38].

Raman spectroscopy [39–41] is a spectroscopic technique based on inelastic scattering of monochromatic light (usually from a laser source) by molecules. The scattered light is frequency-shifted with respect to the excitation frequency, the magnitude of this shift is independent of the excitation frequency and is related to the energy spacing between the vibrational energy levels of the molecule. Therefore, the Raman signal gives a direct measure of the vibrational energies of a molecule. Raman spectroscopy can be used to study solid, liquid and gaseous samples. It is commonly used in chemistry, because the vibrational spectrum of a molecule is specific to the chemical bonds and symmetry of the molecules. The Raman spectrum therefore provides a fingerprint by which the molecules can be identified.

The Raman signal from spontaneous Raman emission is very weak.

When illuminated with UV light, many molecules will fluoresce and the weak Raman signal is often swamped by this strong fluorescence. For stimulated Raman emission, the samples have to be illuminated with laser pulses of high intensity and this can cause damage to the sample, induce phase changes or initiate photochemical reactions. It is very difficult to detect low-frequency Raman modes in the range below 3 THz, because the scattered light has a wavelength very close to the main laser line and is therefore difficult to filter out.

X-ray spectroscopy is another common analytical technique with a broad range of applications, particularly in determining crystal structure and elemental analysis of solid samples. Having a wavelength of the order of interatomic distances allows X-rays to be diffracted, producing diffraction patterns (XRD) characteristic of the crystal structure [42]. The X-rays used in this XRD technique constitute ionizing radiation and exposure to such ionizing radiation can pose health hazards.

Fourier transform (FT) spectroscopy was one of the most popular spectroscopic techniques before the advent of THz time-domain spectroscopy (THz-TDS). The classical FT spectrometer consists of a broadband source of radiation, a Michelson interferometer, and a broadband detector. The type of sources and detectors used depends on the frequency region of interest. Instead of recording the amount of energy absorbed as a function of frequency, the light is sent through an interferometer. The signal measured after passing through the sample is the interferogram. The detector records the interferogram while the mirror is moved. The Fourier transformation of this resulting interferogram gives frequency domain information [43]. With a broadband source, the FT spectrometer (FTS) is capable of measuring spectra from the far-infrared to the near-infrared part of the electromagnetic spectrum [44]. No single source and detector can be used for this entire frequency range.

Unlike a dispersive instrument, i.e. a grating monochromator or spectrograph, an FT spectrometer collects all wavelengths simultaneously. The broadband sources of infrared radiation used in a FT infrared (FTIR) spectrometer are the "Globar " or high pressure mercury lamps. Globar is a ceramic alloy that can be heated to 1500 K . This temperature is equivalent to a black body radiating light with a peak frequency at 80 THz. The mercury lamp is used for mid-infrared and IR spectroscopy. The detectors used in FTIR spectrometers are generally pyroelectric detectors and bolometers. These detectors have to be operated at very low temperatures, often as low as a few K. A far-infrared FT spectrometer has high SNR at high THz

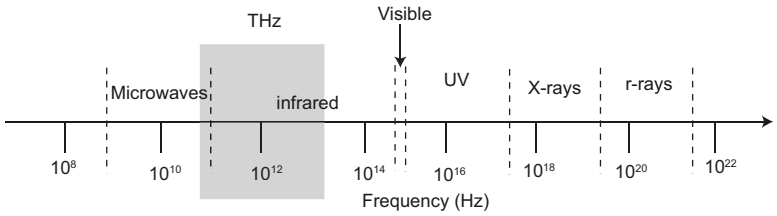

Figure 1.2: Schematic diagram of the electromagnetic spectrum with the position of the terahertz region indicated in gray. The frequency axis is on a logarithmic scale.

frequencies but its SNR is very poor below 3 THz. The incoherent thermal detectors used in an FT spectrometer can be overwhelmed by the IR radiation emitted by the hot materials while studying samples at high temperature. An FT spectrometer operating in the THz frequency range has to be flushed with dry nitrogen to get rid of any water vapor, in order to avoid the absorption of THz radiation by the water vapor. Fourier transform spectroscopy suffers from the formation of standing waves which makes the spectral analysis complicated.

1.3 History and development of Terahertz technology

Terahertz radiation is the part of electromagnetic spectrum which lies between the microwave and infrared regions of the electromagnetic spectrum as shown in Fig. 1.2. The THz region marks the transition between these two regions. The far-infrared or terahertz frequency range has been investigated for more than 120 years. THz radiation is loosely defined as the frequency range from 0.1 to 10 THz, which corresponds to wavenumbers between 3.33 and 333 cm^{-1}, wavelengths between 3 mm and 30 μm. Due to lack of efficient sources and sensitive detectors, this frequency range was known as the 'THz gap'. Interesting compilations of the history of the THz research are given in [45, 46]. The Mercury arc lamp in a quartz envelop was an excellent source of long-wavelength infrared radiation after Rubens and Baeyer discovered it in 1911. The bolometer, invented by Langley in 1880 was almost universally used as the detector and this remained a good detector of far-infrared radiation for decades. The 1960s was a flourishing decade for THz technology, as it saw the creation of much of the instrumentation which is still widely in use today. The first

high power far-infrared source, the water vapor laser, was developed in this time period [47]. Probably, the most important single development responsible for the tremendous growth in the THz frequency region in recent years is the invention of the mode-locked Ti:sapphire laser. These lasers are capable of generating extremely short pulses of light at a high repetition rate. These pulses are partially converted into THz light using means described in this thesis. The development of the THz time-domain spectrometer in the form known today, became possible through the combination of the development of femtosecond lasers and new electro-optic materials.

1.4 Generation of terahertz radiation

THz sources can be broadly classified as incoherent thermal sources, broadband pulsed sources and narrowband continuous-wave sources. Incoherent thermal sources are, for example, arc lamps or SiC globar elements. The high operating temperature of these devices results in the emission of a very broad range of frequencies, among which are THz frequencies. Most broadband pulsed THz sources are based on the excitation of different materials with ultrashort laser pulses. In general, THz radiation from the photo-excited semiconductor surface can be emitted by a dipole that is induced due to a fast changing photocurrent in the material [48–50]. The electrons and holes that are optically generated in the semiconductor material due to the inter-band absorption of the femtosecond pulses are spatially separated by the built-in electric field, externally applied electric field or due to the photo-Dember effect. This results in a transient photocurrent varying on a sub-picosecond time scale [51–53]. This transient current generates THz radiation. This mechanism of THz generation is known as the photocurrent surge effect. Optical rectification is an alternative mechanism for pulsed THz generation [54]. Optical rectification is possible only in crystals without inversion symmetry and having sufficiently large values of the nonlinear susceptibility.

There exist a number of techniques for generating *narrowband* THz radiation. The techniques mostly used for low power (<100 μW) continuous wave THz radiation are up-conversion techniques. These up conversion techniques generally make use of electronic methods to generate THz frequencies from lower frequencies namely, microwave frequencies [55–60]. This is typically achieved by using a chain of planar GaAs Schottky-diode multipliers [57, 61]. Gas lasers such as methanol and hy-

drogen cyanide lasers are also very popular narrowband THz sources. Optical techniques such as photo-mixing in a non-linear crystal can generate continuous wave THz radiation [62]. Tunable continuous wave THz radiation has been demonstrated by mixing of two frequency-offset lasers in low-temperature grown GaAs (LT-GaAs) and by mixing two frequency modes from a single multimode laser [63].

Semiconductor deposition techniques are so advanced that it is possible to construct multiple quantum-well semiconductor structures for laser emission. Such lasers, known as quantum cascade lasers, have been demonstrated at THz frequencies [64, 65]. This has the advantage that it can produce powers in the milliwatt range in a device of small dimensions that can potentially be produced cheaply. These features make the quantum cascade laser a good candidate for commercial applications. But, these lasers require operating temperatures of 70 K or lower [66–68].

Intense terahertz sources are based on the acceleration and deceleration of high energy electron beams in strong magnetic fields. Free electron lasers (FEL) and backward wave oscillators (BWO) fall in this category. FELs are capable of generating intense THz radiation [69, 70] and BWOs can produce coherent radiation with a slightly tunable frequency. To operate, however, BWOs require a highly homogeneous magnetic field of approximately 10 kG. The power levels that can be reached with such a device rapidly decrease with frequency to values of the order of micro watts [71].

Currently, conversion efficiencies of all these sources are very low. In the case of THz generation by photoconductive antennas, the radiated energy mainly comes from the electrical power supply and the THz radiation energy scales with the bias voltage and optical fluence [72]. The breakdown field of the material determines the maximum bias voltage that can be applied [73]. Photoconductive emitters are capable of generating relatively large average THz powers of about 100 μW and bandwidths as high as 6 THz [74, 75]. In optical rectification, the energy of the emitted THz radiation comes directly from the exciting laser pulse. The conversion efficiency in this case depends on the nonlinear coefficients of the material and on the phase matching conditions. The power of THz radiation generated by optical rectification is lower than the THz powers generated from photoconductive antenna, but optical rectification can provide very large bandwidths up to 60 THz [76–78].

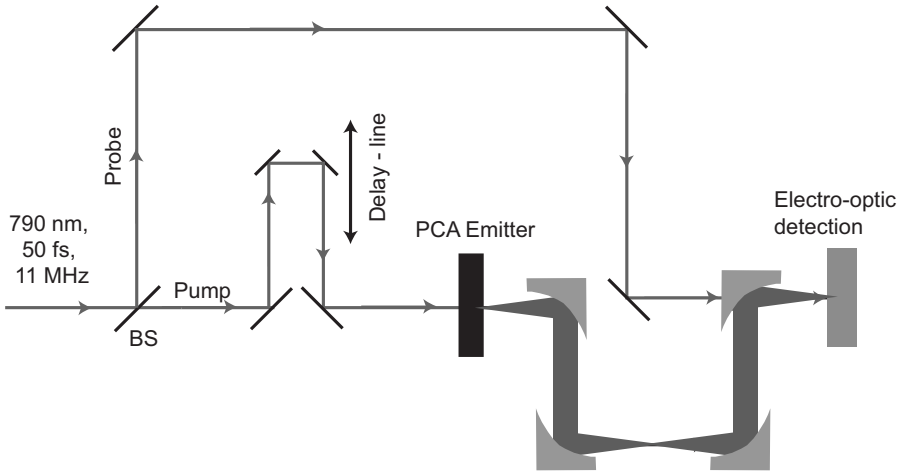

Figure 1.3: Schematic experimental setup for a THz time domain spectroscopy.

1.5 Terahertz time domain spectroscopy (THz-TDS)

In THz time domain spectroscopy (THz-TDS), all the measurements are taken in the time domain. The THz electric field is measured as a function of time. The ultrashort pulses make it possible to measure the electric fields oscillating at THz frequencies by stroboscopic, time gated detection. The Fourier transform of a THz pulse gives a THz spectrum, and because the electric field rather than intensity is measured, both the amplitude and phase of the field are known, providing information on both the refractive index the absorption coefficient of the sample at many frequencies simultaneously.

THz-TDS is very promising for its unique time resolved feature and high signal-to-noise ratio. In time gated detection, the detector is kept off for the time between two detection events, thus making the detection process insensitive to thermal background radiation. This can be very advantageous under high temperature experimental conditions. The coherent detection gives a noise equivalent power of about $10^{-16}\mathrm{WHz}^{1/2}$, which is 4 orders better than helium cooled bolometer and 6 orders better than a pyro-detectors generally used in FT spectrometers. THz-TDS does not suffer from the formation of standing waves as in an FT spectrometer.

For applications such as, identification of materials with THz resonances, or polymorph identification, THz spectroscopy is preferred because unlike X-rays, terahertz radiation is non-ionizing radiation and does not pose any health hazards. The average power of THz radiation used

for the measurements is below 1 μW and hence no thermal strain is induced in the sample. In Raman spectroscopy, the illumination of samples with laser pulses of high intensity can cause damage to the sample, induce phase change or initiate photochemical reactions.

A typical THz-TDS setup is described in Fig. 1.3. Historically, water vapor was the first molecule measured with THz -TDS simply because of its strong absorption and abundance in a laboratory atmosphere [31]. Fig. 1.4 shows the THz transmission spectrum of water vapor [79]. Water molecules have a lot of absorption bands in the THz frequency range. This means that, long THz beam path through air in a typical THz-TDS setup necessitates that the beam path be flushed with dry N_2 gas to reduce the absorption of the THz radiation by water vapor molecules in the atmosphere. This setup also requires parabolic mirrors to collimate, steer and focus the THz radiation onto the detection crystal making the alignment difficult, especially considering that THz radiation is invisible. The THz beam diffraction and absorption at the reflecting surfaces in the THz beam path will lead to reductions in the THz power. One way to overcome all these above mentioned problems is by placing the THz source and detector very close to each other, in the quasi-near field geometry as described in Chapter 3 of this thesis.

1.6 This thesis

The goal of this thesis work is to develop and apply THz spectrometer with a high SNR and a broad bandwidth. This spectrometer can eventually be used to study the THz absorption spectra of different materials. In Chapter 2, an explanation of THz generation from photo-conducting antennas is discussed. We discuss the saturation effects occurring in photoconducting antennas due to the focussing of high intensity laser pulses on the emitter. We explain our results with existing phenomenological models describing emitter saturation. Chapter 3 discusses the quasi-near field spectrometer which does not require complicated alignment that is usually present in THz-TDS setups and also need not to be flushed with dry nitrogen gas. We will also describe the theory behind THz generation by optical rectification and detection of THz radiation by electro-optic detection in this chapter. Some applications of the quasi-near field spectrometer will be discussed in Chapter 4. This chapter will contain the THz absorption spectra of some amino acids, and some other materials in the frequency range of 0.5 - 7 THz. Chapter 5 will give a potential industrial

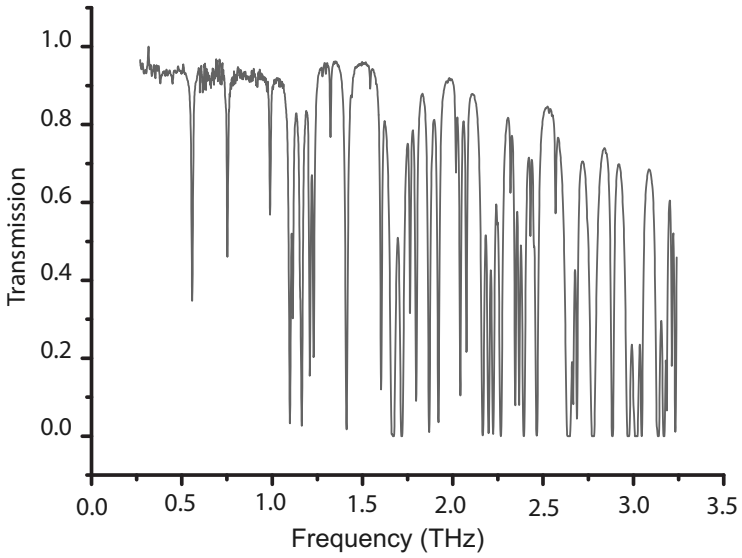

Figure 1.4: Measured transmission spectrum through a 1 m long air column with a 40% relative humidity [79]

application of the quasi-near field spectrometer, namely the identification of polymorphs in freeze dried products. Conclusions and future prospects are given in Chapter 6.

2

THz generation using photo-conductive antenna

2.1 Introduction

There exist various techniques to generate terahertz (THz) radiation. In general, these techniques can be divided into two, namely, optical methods and electronic methods. Common to all optical techniques is an ultrafast change in polarization triggered by a femtosecond laser pulse. In photo-conductive antennas (PCA's), such a time-dependent polarization is formed when charge carriers, created by a femtosecond laser pulse, are accelerated in an externally applied electric field. PCA's are capable of generating broadband pulses with a fairly high power. Such a photo-switch, or Auston switch as it is sometimes called, is usually formed by depositing two electrodes on a suitable semiconductor material with the right bandgap. This technique was originally developed by Auston [48], and later Grischkowsky developed it into a free space THz spectrometer [80]. In this chapter, the THz generation mechanism in a PCA and saturation effects in the THz generation are discussed.

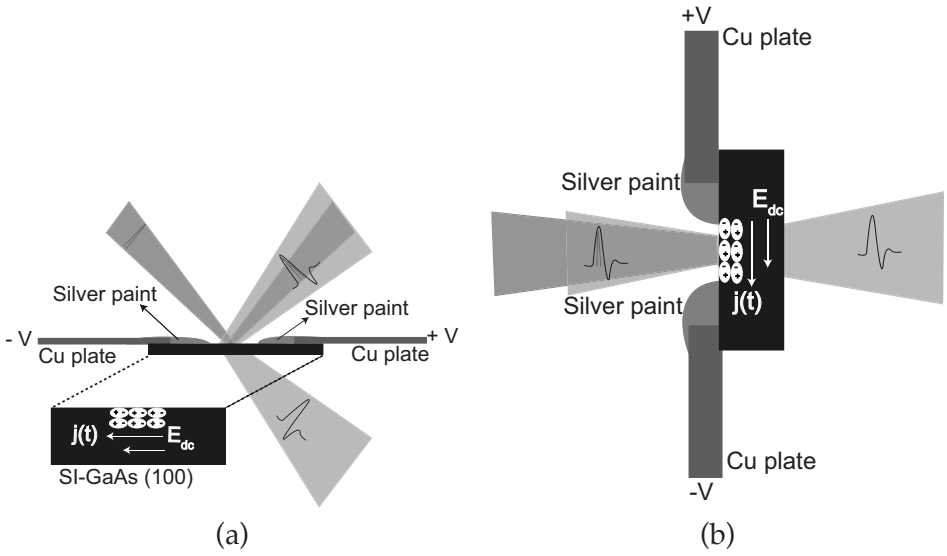

Figure 2.1: THz generation in a photo-conductive antenna. Femtosecond pulses are focussed onto the semiconductor between the two electrodes, which are biased with a high voltage. The THz radiation is emitted both in the direction of the reflected laser pulses and in the original propagation direction of the laser pulse. The depth into the semiconductor where electron-hole pairs are created depends on the wavelength of the pump and on the semiconductor used. For a wavelength of 800 nm, this depth is about 0.6 μm in GaAs [81]. (a) Femtosecond pulses are incident at an angle on the semiconductor. This method is mainly employed when the THz pulses are collected in reflection. (b) The femtosecond pulses are normally incident on the semiconductor surface.

2.2 Photo-conductive antenna

A PCA consists of a semiconductor with two electrodes attached to it. The semiconductor can be biased by an externally applied voltage. The distance between the electrodes can range from several microns to several centimeters. The first antennas used electrode separations of about 100 μm on which lasers were focused to a spot size of about 10 μm [48]. When a short laser pulse, with a photon energy larger than the band gap energy of the semiconductor, hits the biased region of the semiconductor surface, electron-hole pairs are created. Thus, the semi-insulating semiconductor becomes a conductor. The applied voltage causes a current through the semiconductor to rise on a sub-picosecond time scale and to

fall on a slower time scale as the carriers get eventually trapped and recombine. In the far field (at distances much larger than the wavelength of emitted radiation or the size of the antenna), the radiated THz electric field is proportional to the first temporal derivative of the photo-current in the emitter. The resulting radiation is polarized along the direction of the applied bias field. The schematic description of a PCA is given in Fig. 2.1. The figure shows two configurations: (a) when the incident angle of the laser pulse with respect to the surface normal is 45°, and (b) when the laser pulses are normally incident on the semiconductor surface. The THz radiation is emitted both in the direction of the reflected laser pulses and in the original propagation direction of the laser pulse. The depth into the semiconductor where the electron hole pairs are created depends on the wavelength of light and the type of semiconductor used. When laser pulses with a central wavelength of 800 nm are used to illuminate a GaAs surface, this absorption depth is about 0.6 μm [81].

2.3 A simple model for THz generation with PCA

Here, we describe THz generation from a PCA with a simple analytical model from Duvillaret et al. [82]. Under optical illumination, a photo-current is generated in the dc-biased PCA and the resulting rapidly changing current radiates a THz pulse. The time dependent photo-current density in the emitter can be described as the convolution of the optical pulse with the material response for the current in the photo switch [82].

$$j(t) = P(t) \otimes [n(t)qv(t)] \tag{2.1}$$

where, $\otimes$ denotes the convolution, $P(t)$ is the pulse envelope and q, $n(t)$ and $v(t)$ are respectively the charge, density, and the velocity of photo-generated carriers. The dynamics of the photo-generated free carriers in semiconductors are well described by the classical Drude model. According to this model, the average velocity of free carriers obeys the differential equation

$$\frac{dv(t)}{dt} = -\frac{v(t)}{\tau_s} + \frac{q}{m^*}E(t) \tag{2.2}$$

where τ_s is the carrier scattering time and m^* is the effective mass of the carriers. We assume the envelope of the laser pulse to be a Gaussian and the bias field, $E(t)$ to be a constant E_{dc} over the whole illuminated region of the photo-conductive region. We neglect the screening field induced by the spatial separation of the photo-electrons and holes. This assumption

is valid only for carrier densities smaller than about 10^{18} cm^{-3} [83]. Using equations 2.1 and 2.2 and using the following exponential functions for $n(t)$ and $v(t)$,

$$n(t) \propto \exp\left(-\frac{t}{\tau_c}\right) \tag{2.3}$$

$$v(t) \propto \frac{\tau_s}{m^*}\left(1 - \exp\left(-\frac{t}{\tau_c}\right)\right)E_{dc} \tag{2.4}$$

where, τ_c is the carrier life time of the semiconductor, we finally get,

$$j(t) \propto \int_0^{+\infty} \frac{\mathrm{P(t)}}{\tau} \exp\left(-4\ln 2\frac{(t-t')^2}{\tau^2}\right)\exp\left(-\frac{t'}{\tau_c}\right)\frac{\tau_s}{m^*}\left(1 - \exp\left(-\frac{t}{\tau_c}\right)\right)E_{dc}dt' \tag{2.5}$$

$$\begin{aligned} j(t) \quad \propto \quad & \left\{\exp\left(\frac{\tau^2}{4\tau_c} - \frac{t}{\tau_c}\right)\mathrm{erfc}\left(\frac{\tau}{2\tau_c} - \frac{t}{\tau}\right) - \exp\left(\frac{\tau^2}{4\tau_c'} - \frac{t}{\tau_c'}\right)\right. \\ & \left.\mathrm{erfc}\left(\frac{\tau}{2\tau_c'} - \frac{t}{\tau}\right)\right\}\frac{PE_{dc}\tau_s}{m^*} \end{aligned} \tag{2.6}$$

where, τ is the pulse width of the optical laser pulse and τ_c' is given by

$$\frac{1}{\tau_c'} = \frac{1}{\tau_c} + \frac{1}{\tau_s} \tag{2.7}$$

Here, only one type of carrier (electrons) is considered. In principle, a complete expression for the generated photo-current could be obtained by adding the contribution from the holes as well. In the far field, the radiated electric field by this transient current is proportional to the first time derivative of it.

$$E_{THz}(t) \propto \frac{dj(t)}{dt} \tag{2.8}$$

Figure 2.2 (a) shows the calculated current response of the PCA excited by a short laser pulse. The photo-current in the emitter shows a longer decaying tail for increasing carrier life times. The rising edge in the photo-current is determined by the pulse width of the incident laser pulse. Figure 2.2 (b) shows the THz electric field generated from the transient current shown in Fig. 2.2(a). It is clear from Fig. 2.2(b) that the influence of τ_c on the generated THz electric field is relatively small. The emitted THz radiation is mostly generated during the rising edge of the photo-current and thus the carrier life time, τ_c, has only a relatively small effect on the

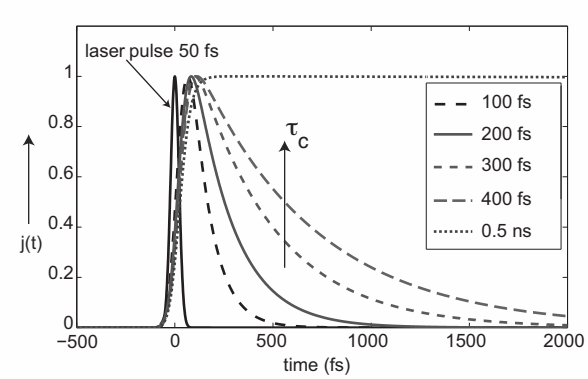

(a)

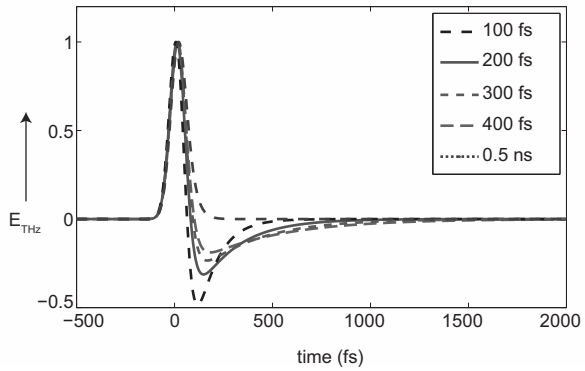

(b)

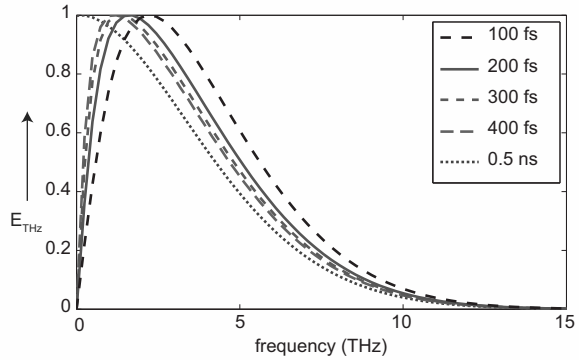

(c)

Figure 2.2: (a) Photo-current response j(t) of a PCA excited by a short laser pulse of 50 fs duration. The photo-currents are calculated with τ_s = 30 fs [84] and τ_c ranging from 100 fs to 400 fs. (b) THz pulses generated by the photo-current, j(t). (c) THz spectra of the THz pulses shown in (b).

THz pulse shape. Also, the fairly modest influence of τ_c on the generated THz electric field is clear from the spectrum of the generated THz electric field shown in Fig. 2.2 (c). The bandwidth of the generated THz radiation does not vary tremendously for τ_c=100 fs, 200 fs, 300 fs, 400 fs and 0.5 ns. As τ_c increases from 100 fs to 0.5 ns, the frequency at which the THz spectrum has its maximum shifts to lower frequencies. The bandwidth of the generated THz spectrum is largely determined by the pulse width of the laser. Figures 2.3 (a) and (b) respectively show the THz signal calculated for τ_s = 30 fs, τ_c = 500 fs, for various values of the pulse width of the exciting laser and the corresponding THz spectrum. The shorter the pulse duration of the exciting laser pulse, the shorter the duration of the generated THz pulse, and the broader the spectrum. This means that the pulse width of the exciting laser pulse largely determines the bandwidth of the generated THz spectrum. Therefore, in spite of the relatively long carrier life time in semi-insulating GaAs (SI-GaAs) (~ 1 ns), it is still an excellent material for the generation of THz pulses. Shorter carrier life times in low temperature grown GaAs (LT-GaAs) allow for higher bias voltages but this is offset by the lower carrier mobility. As a result, there is little difference between the maximum THz amplitude generated from SI-GaAs and LT-GaAs [74]. LT-GaAs only has a slight advantage that the frequency where the spectrum reaches its maximum shifts to somewhat higher values.

From Fig. 2.3 (a), it can be seen that width of the main peak of the THz pulse is similar to the pulse width of the exciting laser. However, as we will see later, in Fig. 2.7 the THz pulse main peak width is ~1 ps which is greater than the pump pulse width. Apart from these differences in pulse widths, the measured THz pulse shape is also different from what is seen in Fig. 2.3 (a). This is at least partially explained by the fact that the model does not take into account the details of the scattering processes taking place. In spite of this, this phenomenological model is helpful to explain the main features of the emitted THz radiation such as the small dependence of the bandwidth on carrier lifetimes.

2.4 Far field THz generation and detection setup

A basic THz generation and detection setup is shown in Fig. 2.4. It uses a PCA for the THz generation and electro-optic sampling for THz detection. Both for the generation and detection processes, femtosecond pulses are used. These femtosecond pulses are derived from the same laser (Femtosource Scientific XL, Femtolasers). The laser delivers pulses of nearly 50

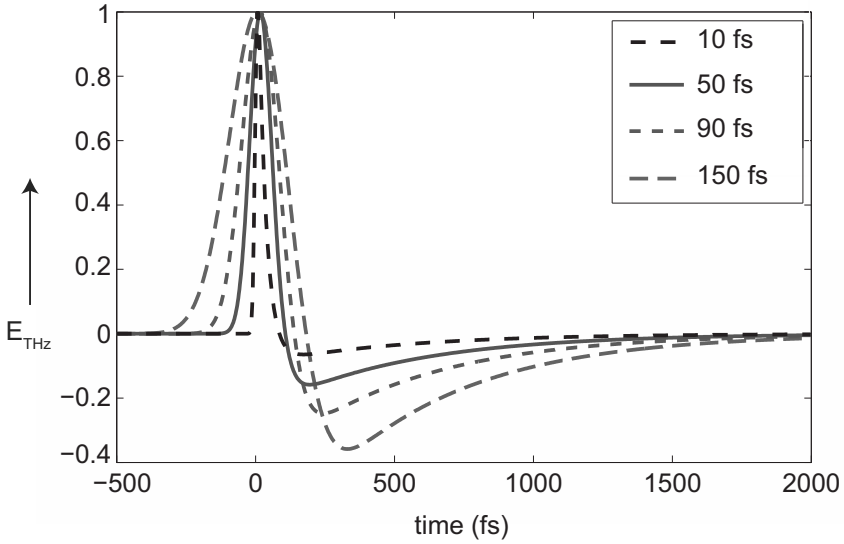

(a)

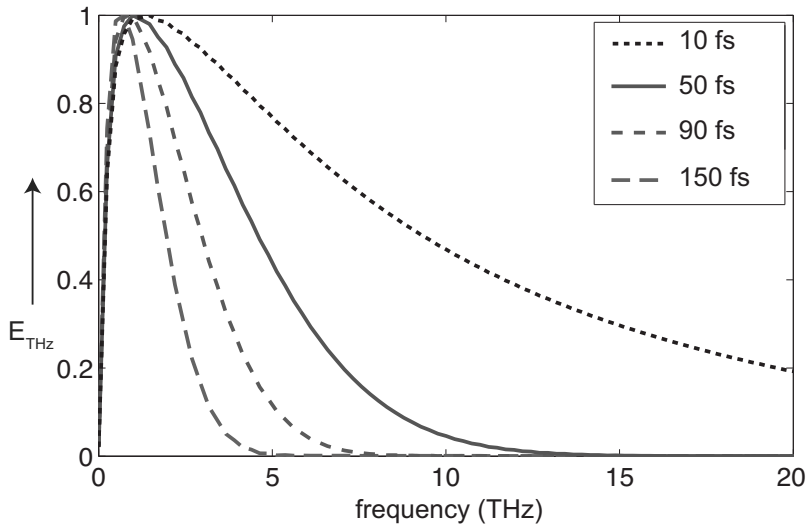

(b)

Figure 2.3: (a) THz pulses emitted from a PCA with τ_s = 30 fs, τ_c = 500 fs and for four values of the pulse width of the exciting laser. (b) Spectra of the THz pulses shown in (a). The THz pulse shape and the bandwidth of the THz spectrum are largely determined by the pulse duration of the exciting laser.

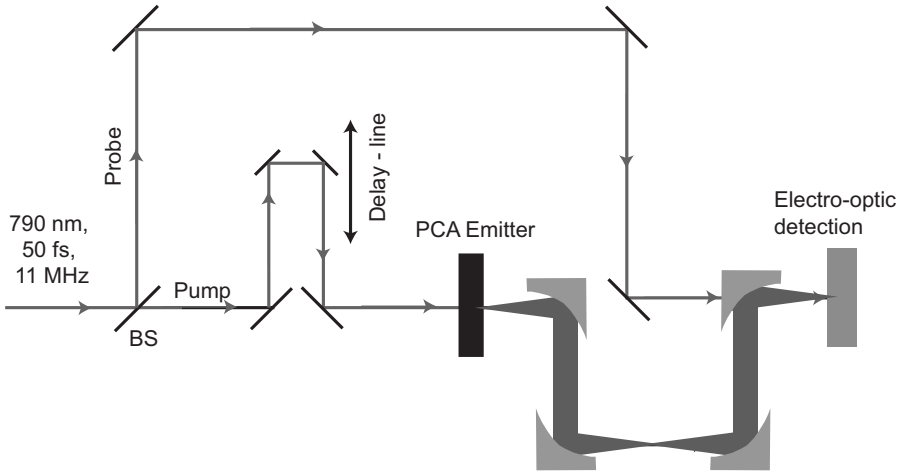

Figure 2.4: Schematic diagram of a conventional THz generation and detection setup.

fs duration with an average power of 960 mW and a repetition rate of 11 MHz. The peak power of the laser is more than 1.3 MW and the output energy is more than 80 nJ. Gold-coated 90° off axis parabolic mirrors are used to collect, collimate and focus the THz radiation. Here, we use a biased semi-large aperture PCA made on a SI-GaAs [85].

A schematic diagram of the emitter is shown in Fig. 2.5. The emitter consists of a SI-GaAs crystal of (100) orientation, which has a dark resistivity of more than $5 \times 10^7 \Omega$cm. Two crescent-shaped silver paint electrodes are painted on the surface of the semiconductor with a smallest separation of ≈ 300 μm (the smallest separation can be between 300 μm to 1.5 mm). The electrodes are "glued" onto two thick copper strips with silver paint. The copper strips are separated by 2 mm. Each copper strip forms contact with one silver paint electrode only. The copper strips serve as good electrical contacts to the voltage source and also provide a good heat sink for any generated heat in the GaAs crystal. The copper strips are connected to a water cooled copper block using an electrically insulating and thermally conductive sheet. Instead of applying a constant bias voltage, we have used a 50 kHz, ±200 V square wave ac bias voltage. When the voltage changes from +200 V to -200 V, the THz signal changes sign as well. The emitted THz pulses are modulated at 50 kHz and lock-in detection is done at 50 kHz. The signal detected by the lock-in detector is twice the signal one would get when the applied voltage switches between 0 to 200 V only. To couple THz pulses efficiently into free space, a silicon lens is

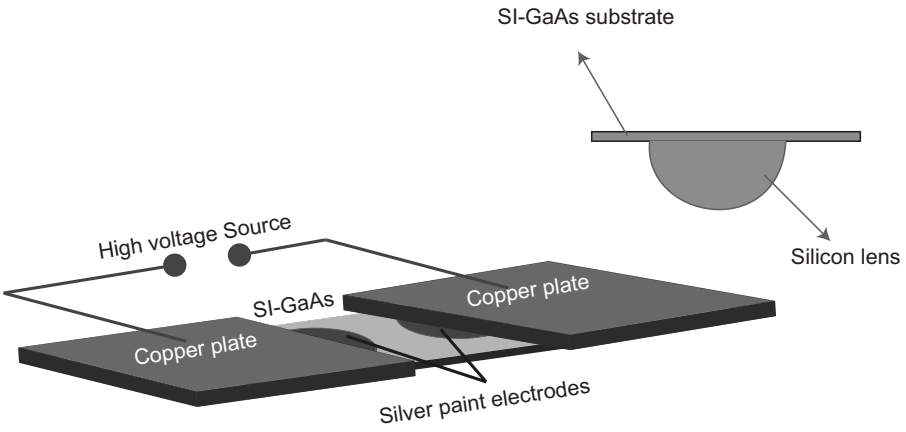

Figure 2.5: A semi-large aperture PCA. The two crescent-shaped electrodes are made with silver paint. The SI-GaAs with silver electrodes is attached to the copper strips with silver paint. The copper plates act electrical contacts to the high voltage source and as heat sink.

placed on the back side of the SI-GaAs as shown in Fig. 2.5. If no substrate lens is used, a large part of the generated THz pulse is reflected from the back of the SI-GaAs and also less light is collected by the parabolic mirror. This silicon lens is an aplanatic hyper hemispherical lens. Silicon is chosen because it has a very low absorption and nearly uniform refractive index (n = 3.42) between 0.2 and 5 THz which strongly reduces chromatic aberration.

2.5 Electro-optic sampling

Figure 2.6 shows the schematic drawing of an electro-optic detection setup. The generated THz pulses are collected, collimated and focussed onto an electro-optic detection crystal with a set of four 90° off-axis gold-coated parabolic mirrors. The probe pulse, derived from the same laser, is focussed along with the THz pulse onto the detection crystal through a hole in the last parabolic mirror. The THz pulse and the probe pulse co-propagate in the detection crystal, a (110) ZnTe crystal of thickness 0.5 mm. When there is no THz electric field, the initially linearly polarized probe beam will remain linearly polarized after passing through the detection (ZnTe) crystal. This linearly polarized probe beam is circularly polarized

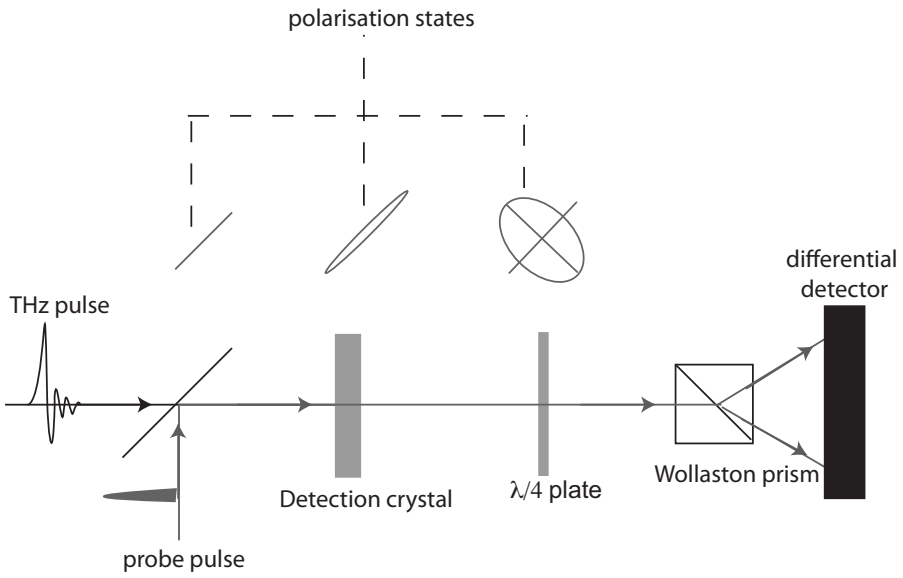

Figure 2.6: Schematic representation of an electro-optic detection setup.

by the quarter-wave plate, and the Wollaston prism splits the probe beam into two orthogonal polarizations of equal intensity. The output of the differential detector is then zero. The THz electric field induces birefringence in the crystal which makes the linearly polarized probe beam elliptically polarized after propagating through it. The probe beam then passes through a quarter wave plate, which introduces a phase shift of $\pi/2$ between the two orthogonal components of the incident electric field. The beam then passes through a Wollaston prism that splits the beam into two beams having orthogonal polarizations. These two beams are focussed onto the two photo-diodes of the differential detector, which gives an output signal that is proportional to the difference in intensity of the two beams and thus the instantaneous THz electric field. A full 20 ps long THz electric field transient is obtained by varying the optical delay between the probe pulse and the THz pulse.

2.6 Signal-to-noise ratio (SNR)

In Fig. 2.7 the measured THz electric field as a function of time is shown. The electric field consists of a nearly single cycle pulse, followed by an oscillatory tail caused by the absorption, and subsequent re-emission of

THz radiation, by water vapor molecules in the air. The inset shows a measurement with the THz beam blocked. We define the signal to noise ratio (SNR) as the ratio of the peak-to-peak amplitude of the THz signal to the root mean square value of the noise when the THz beam is blocked. We obtained very good signal to noise from our setup. A SNR of 15000 was very easily achieved from our system in a measurement time of 10 ms, which is considered very good for a THz generation and detection setup based on a Ti:sapphire laser oscillator. When THz beam and probe beam have the same or orthogonal polarizations, the instantaneous THz electric field can be calculated from the following equation [86],

$$E_{THz} \propto \frac{\triangle P c}{P_{probe} \omega n^3 r_{41} L} \tag{2.9}$$

where, $\triangle P = P_1 - P_2$ is the difference in intensity on the two diodes of the differential detector and $P_{probe} = P_1 + P_2$ is the intensity of the probe beam. r_{41} = 3.9 pm/V is the electro-optic coefficient for ZnTe, n = 2.8 is the near infrared refractive index for ZnTe, c is the velocity of light in vacuum, ω is the near IR angular frequency, and L is the thickness of the detection crystal. Using Eqn. 2.9, the calculated peak electric field value was about 140 V/cm. These values are obtained with bias voltages of ±200 V.

The SNR and THz electric field measured with our setup based on a low repetition rate, high peak power, 50 fs laser compares favorably with what has been reported in literature so far from THz generation detection setup based on a Ti:sapphire laser oscillator.

2.7 Saturation effects

The Ti:sapphire laser delivers pulses of 50 fs duration at a low repetition rate of 11 MHz at an average power of 960 mW. This means that the pulses have a very high peak intensity of about 1 MW and a pulse energy of about 80 nJ. These high values of peak intensity and pulse energy results in the saturation of the PCA emitter. In this section, we will study the effect of increasing pump power and pump fluence on the emitted THz radiation.

The smallest separation between the crescent shaped silver paint electrodes is about 1.25 mm. With this electrode separation and laser spot size, the emitter can be called a semi-large aperture emitter [85]. The pump beam is focussed on the PCA between the two silver paint electrodes by a plano-convex lens of focal length 15 cm. By changing the distance between the PCA and the pump laser, the spot size on the PCA can be changed.

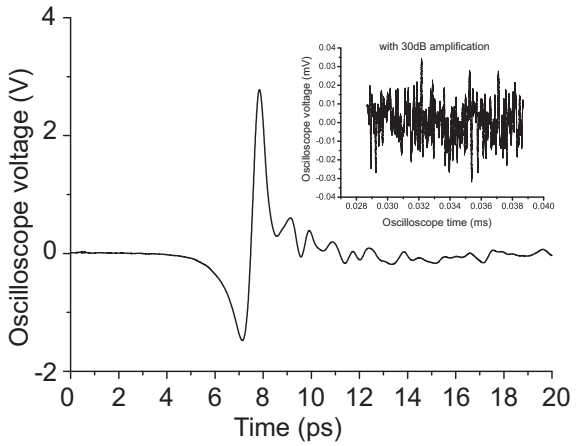

Figure 2.7: THz signal from a PCA biased with ±200 V. The noise measured after blocking the THz beam is shown in the inset. The THz signal is measured without any amplification whereas the measured noise is amplified by 30 dB by the amplifier. The SNR of this measurement is ~15000 in a total measurement time of 10 ms.

Here we show the results for two different spot sizes of the pump laser corresponding to two different positions of the lens. One, when the PCA is placed at the focal point of the lens, the emitter is then called in-focus emitter. Second, when the distance between the lens and the PCA is smaller than the focal length of the lens, the emitter is then called out-of-focus emitter. The in-focus spot size is about 50 μm and out-of-focus spot size is about 400 μm. It is made sure that the parabolic mirrors collect all the THz radiation emitted by THz emitter, so that the increased divergence of the emitted THz radiation from the in-focus emitter does not contribute to the decrease in the measured signal amplitude. the Optical fluence is defined as the ratio of average power to the area of illumination. When we change the pump laser spot size on the emitter, it is the optical fluence on the emitter that is changing.

Figures 2.8 (a) and (b) show the measured peak-to-peak THz electric field as a function of optical fluence on the emitter for the in-focus and out-of-focus emitter respectively. Thus, Fig. 2.8 (a) shows the dependence of emitted THz electric field on the pump fluence when the optical fluence on the emitter is quite high and Fig. 2.8 (b) shows the dependence of emitted THz amplitude on the pump fluence when the optical fluence on the emitter is relatively low. The vertical scales in Figs. 2.8 (a) and (b) can

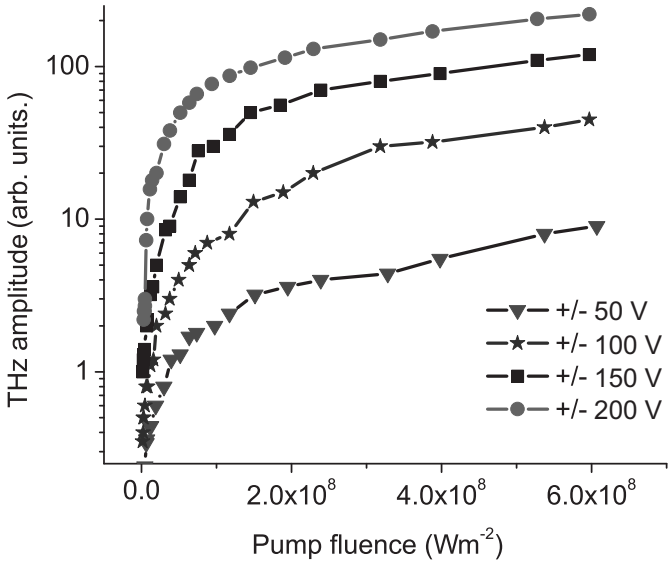

(a)

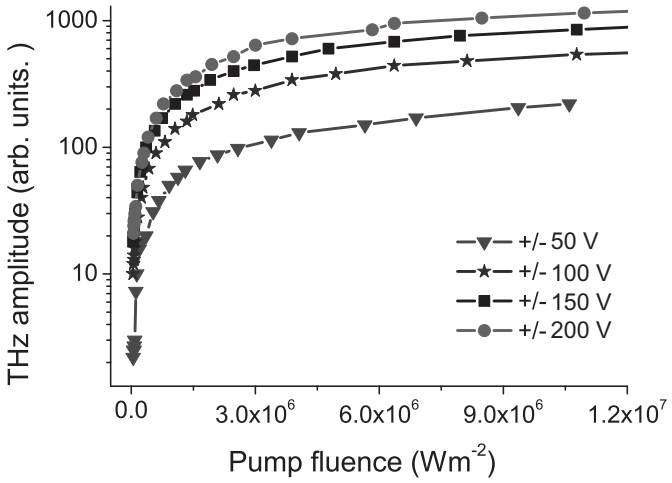

(b)

Figure 2.8: Measured peak-to-peak THz electric field as a function of pump fluence (a) emitter in-focus, pump beam spot size on the emitter is about 50 μm (b) emitter out-of-focus, pump beam spot size on the emitter is about 400 μm. The vertical scales can be directly compared.

be directly compared and it can be seen that the lower pump fluence on the emitter gives a higher amplitude for the emitted THz radiation. The experiment is repeated for four different emitter bias voltages. In all cases the peak-to-peak THz amplitude increases quickly in the beginning and then slowly saturates as the pump fluence increases.

Figures 2.9 (a), (b), (c) and (d) show the peak-to-peak THz electric field as a function of optical intensity for bias voltages of ± 50 V, ± 100 V, ± 150 V and ±200 V respectively, for both the in-focus and out-of-focus emitter. Even though the optical fluence can go to very high values when the emitter is at in-focus, the peak-to-peak THz electric field is much smaller than the peak-to-peak THz electric field from the emitter when it is placed at out-of-focus. It is clear from the figure that for a particular value of optical fluence on the emitter, a larger spot size on the emitter gives a hundred times bigger peak-to-peak THz electric field. This is caused by the saturation of the emitter at high optical fluence.

The saturation effect in the small/semi-large aperture antenna is explained by Kim et al. [87]. The saturation of the emitted THz electric field is due to two effects; Coulomb field screening (space charge screening) and radiation field screening. When the photo-conductor is excited by the optical pulses, electron-hole pairs are created. As the electrons and holes drift in opposite directions, net positive and negative space-charges develop. The electric field induced by this space charge is in a direction opposite to the applied bias field and thus partially screens it. This is called Coulomb or space-charge screening. Apart from the space charge screening, the electric field of the emitted THz radiation itself will screen the applied bias field, which is known as radiation-field screening. As the optical fluence on the emitter increases, more and more electron-hole pairs are created and the emitted THz electric field also increases. This leads to an increase in both the space charge screening and radiation field screening. The saturation of the generated THz field is due to the collapse of the applied electric field by the combined effect of Coloumb field and radiation field screening. For a Gaussian shaped laser spot, Coulomb screening near the edges of the laser spot is weaker than at the center, whereas the radiation field near the edges of the spot closer to the electrodes is stronger than anywhere else since the carriers near these edges move faster than those elsewhere because of the weak Coulomb screening field.

For a fixed optical power, as the excitation-spot size increases (optical fluence decreases), the average carrier density and thus both the radiation and Coulomb screening decrease. Thus for a given excitation level,

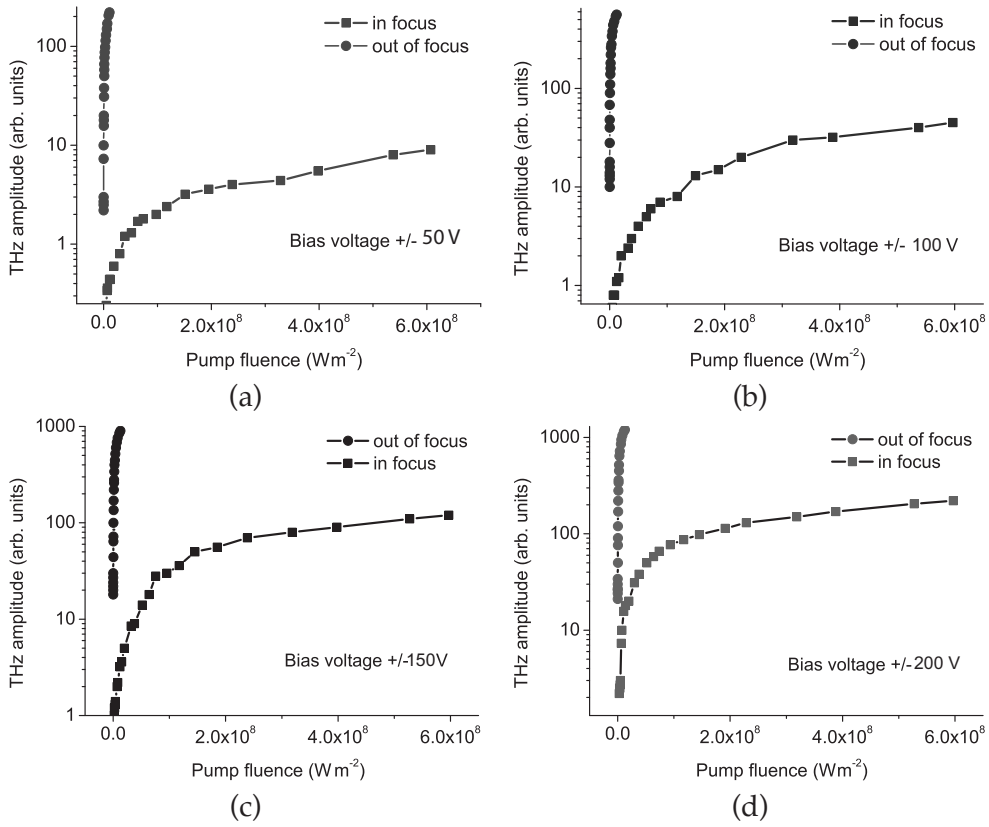

Figure 2.9: Peak-to-peak THz electric field as a function of pump fluence for both tightly and loosely focussed pump beam on the emitter. (a), (b), (c) and (d) show measurements done when the emitter is biased with ±50 V, ±100 V, ±150 V and ±200 V respectively.

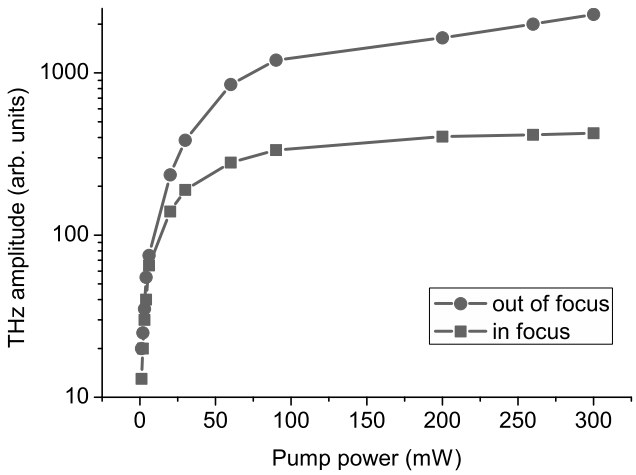

Figure 2.10: Peak-to-peak THz electric field as a function of pump power for two different laser spot sizes on the emitter.

increasing the excitation spot size will lead to an increase in generated THz field. This is clear from Fig. 2.10, where we have the plotted optical power versus peak-to-peak THz field for two different laser spot sizes on the emitter, one for in-focus and one for a much larger out-of-focus spot size. For the same pump power, the larger spot size on the emitter gives rise to a much bigger THz electric field compared to the in-focus spot size case. In the case of the in-focus spot size on the emitter, the THz output is saturated at 100 mW of pump power, where as in the case of the larger laser spot size on the emitter, the THz output is still very slowly increasing with pump power even at the highest pump power.

2.8 Conclusions

The THz generation and detection setup with the photo-conductive antenna as the THz source and electro-optic sampling as the THz detector gives a very high SNR of ~15000, in a measurement time of 10 ms, which is very high for a system based on an oscillator. Even though our 800 nm femtosecond laser pulses have a very high peak power, the generated THz power could not be increased with increasing laser pump power on

the emitter, because of emitter saturation. Increasing the laser spot size on the emitter gave higher THz peak power than in the case of a tightly focussed pump beam.

3 Quasi-near field terahertz spectrometer

3.1 Introduction

Currently, there are several approaches for generating THz beams such as photo-conductive emission as discussed in Chapter 2, optical rectification [88], four-wave mixing in laser generated plasmas, quantum cascade lasers, free-electron lasers (FEL) and synchrotron emission. In the photo-conductive approach high-speed photo-conductors are used as transient current sources which radiate THz light. The optical rectification approach uses electro-optic crystals as a rectification medium, and it is a second order (difference frequency generation) nonlinear optical process. It has been shown that ultra broadband THz radiation in the frequency range of 0.3 - 20 THz can be generated from photoconductive antenna made of LT-GaAs [89]. In principle, by optical rectification, shorter THz pulses can be generated by shorter laser pulses. Using this technique, ultra-broadband THz pulses with a spectrum extending from 100 GHz to 60 THz have been generated in materials like GaSe [90, 91]. In this chapter, we describe a method to generate and detect THz radiation using electro-optic crystals. In this method, the generation and detection crystals are placed close to each other. The THz pulses are generated and detected with, initially counter-propagating, pump and probe beams. This makes this setup ex-

tremely simple, compact and at the same time gives a large bandwidth and an excellent signal-to-noise ratio (SNR) without having to use any lock-in detection.

This chapter is organized as follows. The theory behind optical rectification and the electro-optic effect will be discussed in the first part followed by the drawbacks of the conventional THz generation and detection setup. We will then describe our quasi-near field setup and the experimental results. We will also describe the setup with a simple model and then show the effect of counter propagating probe and THz pulses on the detected signal.

3.2 Optical rectification and electro-optic effect

Optical rectification [54] and the electro-optic effect are nonlinear optical processes which can be used for the generation and detection of subpicosecond THz pulses. Physically, optical rectification is the creation of a quasi-DC or low-frequency polarization in a nonlinear optical crystal in response to an ultra-short laser pulse. This polarization, in fact, follows the envelope of the laser pulse [92]. The electro-optic effect, also known as the Pockel's effect, is physically similar to optical rectification. It describes a change in the high frequency optical refractive index inside a crystal induced by an applied DC/low frequency electric field.

Optical rectification was reported in 1962 [54] as a DC polarization accompanying the passage of 694 nm CW ruby laser beam in potassium dihydrogen phosphate (KDP) and potassium dideuterium phosphate (KD_dP) crystals. Free-space THz frequency generation with a bandwidth of 1 THz by optical rectification was produced by femtosecond colliding-pulse mode locking (CPM) dye laser in $LiNbO_3$ [93]. Here, we will discuss briefly the theory behind optical rectification and electro-optic detection [94]. When an intense laser beam is focussed onto a nonlinear crystal, the electric polarization $\boldsymbol{P}$ in a nonlinear medium will be [94],

$$P^i = \epsilon_0 \sum_j \chi^{(1)}_{ij} E_j + \sum_{j,k} \chi^{(2)}_{ijk} E_j E_k + \sum_{j,k,l} \chi^{(3)}_{ijkl} E_j E_k E_l + \cdots \tag{3.1}$$

where, P^i is the component of polarization $\boldsymbol{P}$ in the $\boldsymbol{i}$ direction. ϵ_0 is the permittivity of free space. $\{\boldsymbol{i}, \boldsymbol{j}, \boldsymbol{k}\}$ are the unit vectors in the Cartesian co-ordinate system. In the component form, the electric field $\boldsymbol{E}$ can be written as, $\boldsymbol{E} = E_i\boldsymbol{i} + E_j\boldsymbol{j} + E_k\boldsymbol{k}$, $\chi^{(1)}$, $\chi^{(2)}$ and $\chi^{(3)}$ are the electric nonlinear susceptibilities of first, second and third order respectively. For the laser

powers that we are dealing with, we can neglect all terms except the first two in the Eqn. 3.1 and $\boldsymbol{P}$ can be written as the sum of linear ($\boldsymbol{P_L}$) and nonlinear ($\boldsymbol{P_{NL}}$) terms,

$$\boldsymbol{P} = \boldsymbol{P_L} + \boldsymbol{P_{NL}} \tag{3.2}$$

For a short and intense laser pulse with a central frequency at ω_0, the nonlinear polarization is given by,

$$\boldsymbol{P_{NL}}(\omega) = \epsilon_0 \int_{-\infty}^{+\infty} \sum_{jk} \chi^{(2)}_{ijk}(\omega; \omega_0, -\omega_0 + \omega) E^j_L(\omega_0) E^k_L(\omega_0 - \omega) d\omega_0, \tag{3.3}$$

where, $\boldsymbol{E_L}$ is the high intensity laser electric field causing the nonlinearity and $\omega << \omega_0$ is the frequency of the THz field. The wave equation for the THz field $\boldsymbol{E_{THz}}$ is

$$\left(\nabla^2 - \frac{\epsilon(\omega)}{c^2}\frac{\partial^2}{\partial t^2}\right)\boldsymbol{E_{THz}}(z,t) = \mu_0 \frac{\partial^2 \boldsymbol{P_{NL}}}{\partial t^2} \tag{3.4}$$

If the Rayleigh lengths[1] of both the laser and THz fields are longer than the crystal thickness, Eqn. 3.4 can be reduced to a one dimensional equation. Eqn. 3.4 can then be written as,

$$\left(\frac{\partial^2}{\partial z^2} - \frac{\epsilon(\omega)}{c^2}\frac{\partial^2}{\partial t^2}\right)\boldsymbol{E_{THz}}(z,t) = \frac{1}{c^2}\chi^{(2)}(\omega)\frac{\partial^2}{\partial t^2}|\boldsymbol{E_L}(\boldsymbol{z},\boldsymbol{t})|^2 \tag{3.5}$$

Assuming the envelope of the laser electric field to be a Gaussian in time, the optical laser pulse can be expressed as,

$$E_L(z,t) = \frac{E_0}{2}\exp\left[-\frac{\left(t - z/v_g\right)^2}{2\tau^2}\right]\exp\left[-i\left(\omega_0 t - k_0 z\right)\right] + c.c., \tag{3.6}$$

where, E_0 is the electric field amplitude of the pump pulse. The pulse width at half maximum intensity, (τ_{FWHM}) of the laser pulse is $2\sqrt{\ln 2}\tau$. Here, we have assumed that the laser pulse width does not change during the propagation through the generation crystal. v_g is the group velocity of the laser pulse for the frequency, ω_0. Substituting Eqn. 3.6 in Eqn. 3.5

$$\left(\frac{\partial^2}{\partial z^2} - \frac{\epsilon(\omega)}{c^2}\frac{\partial^2}{\partial t^2}\right)\boldsymbol{E_{THz}}(z,t) = \frac{E_0^2\chi^{(2)}}{2c^2}\frac{\partial^2}{\partial t^2}\left[\exp\left(-\frac{t - z/v_g}{\tau^2}\right)\right] \tag{3.7}$$

[1]Rayleigh length is the distance along the propagation direction of a beam from the waist to the place where the area of the cross section is doubled.

By taking the Fourier transform of Eqn. 3.7, we get,

$$\left(\frac{\partial^2}{\partial z^2} + \omega^2 \frac{\epsilon(\omega)}{c^2}\right) = -\frac{E_0^2 \chi^{(2)} \omega^2 \tau}{2\sqrt{2}c^2} \exp\left(i\omega z/v_g\right) \exp\left(-\frac{\omega^2\tau^2}{4}\right) \tag{3.8}$$

Using the boundary conditions, $E_{THz}(z=0,\omega) = 0$ and $\frac{\partial}{\partial z}E_{THz}(z=0,\omega) = 0$, Eqn. 3.8 can be solved yielding,

$$\begin{aligned} E_{THz}(z,\omega) &= \frac{E_0^2 \chi^{(2)} \tau}{2\sqrt{2}(n_{THz}^2 - n_g^2)} \exp\left[-\frac{\omega^2\tau^2}{4}\right]\left[\frac{1}{2}\left(1 - \frac{n_g}{n_{THz}}\right)\exp\left(-\frac{i\omega n_{THz} z}{c}\right) + \right. \\ &\left. \frac{1}{2}\left(1 + \frac{n_g}{n_{THz}}\right)\exp\left(\frac{i\omega n_{THz} z}{c}\right) - \exp\left(\frac{i\omega n_g z}{c}\right)\right] \end{aligned} \tag{3.9}$$

where, $n_g = c/v_g$ is the group index of the laser pulse at ω_0 and $n_{THz}(\omega) = \sqrt{\epsilon(\omega)} = n + i\kappa$ is the complex refractive index of the material in the THz frequency region. In the THz region, the nonlinear susceptibility $\chi^{(2)}$ is related to ϵ by the relation, $\chi^{(2)} \propto \epsilon(\omega) - 1$ [94]. Eqn. 3.9 contains three terms; the first term is a backward propagating field at velocity $v_{THz} = c/n_{THz}$. It has a lower amplitude and can be neglected. The second term is a forward propagating field with phase velocity v_{THz}, and the third term is again a forward propagating field at $v_g = c/n_g$. The shape of the THz waveform is determined by the interference between these three terms.

The linear electro-optic effect (Pockel's effect) follows from Eqn. 3.3. Unlike optical rectification in which a high frequency field creates a DC field, in the electro-optic effect, it is the low frequency THz field which mixes with the laser electric field. The susceptibility tensor for the electro-optic effect will be $\chi^{(2)}(\omega_0; \omega, \omega_0 - \omega)$ instead of $\chi^{(2)}(\omega; \omega_0, -\omega - \omega_0)$. The Pockel's effect is generally described by an electro-optic tensor of the material rather than the susceptibility tensor and describes the changes in refractive indices proportional to the applied electric field,

$$\triangle\left(\frac{1}{n^2}\right)_{ij} = \sum_k r_{ijk} E_k \tag{3.10}$$

The linear electro-optic coefficient, r_{ijk} and susceptibility tensor for the electro-optic effect, $\chi^{(2)}_{ijk}$ are related to each other. Efficient generation and detection of THz radiation by the optical rectification and the electro-optic effect requires a medium with a high second-order nonlinearity or high electro-optic coefficients, a proper crystal thickness, and the correct crystal orientation with respect to the linear polarization of the THz radiation.

The surfaces of the crystals should be optically flat for the pump wavelengths.

The THz generation and detection bandwidth is limited by the optical phonon resonances and the phase-matching in the crystals. The generated THz radiation will be strongly absorbed at phonon resonances, which limits the the generation and the detection bandwidth. In addition, these resonances give rise to a more complicated spectrum with reduced power at frequencies around the resonance frequencies.

To enhance the efficiency of optical rectification and the electro-optic effect, the phase-matching condition should be satisfied in the material. The phase-matching condition for optical rectification, i.e. for collinear difference frequency mixing is given by [95],

$$\triangle \boldsymbol{k} = \boldsymbol{k}(\omega_0 + \omega) - \boldsymbol{k}(\omega_0) - \boldsymbol{k}(\omega) = 0 \tag{3.11}$$

which leads to the condition, $\left(\frac{dk}{d\omega}\right)_{\omega_0} \approx \frac{k(\omega)}{\omega}$ or $v_g = v_{THz}$ where, $\omega_0 + \omega$ and ω_0 are two frequencies within the spectrum of the optical laser pulse. This equation implies that phase-matching is achieved when the phase-velocity of the THz wave is the same as the group velocity of the optical pulse. However, the magnitudes of v_g and v_{THz} are generally not equal. The efficiency of THz generation and detection decreases with the increase in the mismatch between these velocities. The distance over which a slight velocity mismatch can be tolerated is called the coherence length, l_c

$$l_c(\omega) = \frac{\pi c}{\omega \left| n_g - n_{THz} \right|} \tag{3.12}$$

Efficient THz generation and detection at a particular THz frequency occurs for crystals with thickness equal to the coherence length for that particular frequency. The strength of the emitted THz electric field and electro-optic detection sensitivity increases with crystal thickness, whereas the THz emission and detection bandwidth decrease with crystal thickness because of the phase-matching effects.

Several nonlinear optical materials are capable of generating THz radiation by optical rectification of a femtosecond near infrared laser pulse, such as those with the zincblende crystal structure. These crystals have only one nonlinear optical coefficient $r_{41} = r_{52} = r_{63}$. The orientation of the crystal is important for optical rectification. For (100) oriented zincblende crystals, there is no optical rectification light in the propagation direction (as the non-vanishing second order optical coefficients r_{41}, r_{52}, r_{63} are not

involved). Among zincblende crystals, the most popular one for the generation of THz radiation by optical rectification is ZnTe [95]. For femtosecond pulse at 800 nm, the phase-matching condition is satisfied at 2 THz in ZnTe, which results in a generated spectrum centered at 2 THz [96]. The bandwidth is limited by the strong phonon resonance at 5.3 THz. GaP is another popular zincblende crystal for THz generation and detection. GaP has a smaller electro-optic coefficient compared to ZnTe, but the phonon resonance for GaP is at 11 THz, thus in principle allowing for a broader bandwidth for THz generation and detection.

Gallium Selenide (GaSe) is another attractive candidate. It is a uniaxial semiconductor with hexagonal structure with a large electro-optic coefficient. It has a high damage threshold and a low absorption coefficient. The disadvantage of GaSe is its softness which makes it fragile and difficult to handle. The central frequency of the generated/detected THz radiation can be tuned by tilting the crystal about a horizontal axis which is perpendicular to the direction of the probe beam [97].

There exist some organic electro-optic crystals with suitable properties for generation and detection of THz radiation. 4-N-methylstilbazolium tosylate (DAST) is an organic electro-optic crystal with a high electro-optic coefficient >400 pm/V at 820 nm [50]. DAST has been shown to perform well at higher frequencies with a generation bandwidth of up to 20 THz from a 100 μm thick crystal. It has a strong phonon resonance at 1.1 THz and two weaker ones at 3 and 5 THz. Another organic crystal that is used for THz generation and detection is N-benzyl-2-methyl-4-nitroaniline (BNA). Like DAST crystals, BNA also gives very intense THz radiation, but BNA has a strong phonon mode at 2.3 THz, limiting the bandwidth of generation and detection to 2.1 THz. The disadvantages of using these crystals are that they have low damage thresholds, and absorption bands in this frequency region, and it is very difficult to get well-polished crystals. Relevant properties of some very commonly used crystals for optical rectification and the electro-optic effect are listed in table 3.1.

We have used GaP crystals for our experiments because its phonon resonance is at 11 THz, thus allowing for a broader bandwidth than ZnTe crystals. Also, GaP has a higher damage threshold compared to ZnTe crystals. The dielectric function of the crystal in the THz frequency domain $\epsilon(\omega)$ is given by [99]

$$\epsilon(\omega) = \epsilon_{el} + \frac{\epsilon_{st}\omega_{TO}^2}{\omega_{TO}^2 - \omega^2 + 2i\gamma\omega} \tag{3.13}$$

Material	Optical phonon resonance (THz) at 300K	electro-optic coefficient (pm/V) r_{41}
GaP	11 [98]	0.97 [92]
ZnTe	5.3 [98]	3.9 [92]
GaSe	7.1 [78]	14.4 [92]

Table 3.1: Some very commonly used materials for THz generation and detection along with their properties.

where, ϵ_{st} is the static dielectric constant, ϵ_{el} is the electronic dielectric constant, ω_{TO} is the angular frequency of the TO phonon resonance, and γ is the damping factor. For GaP crystal ω_{TO} = 11.0 THz [98], ϵ_{st} = 2.03 [100], ϵ_{el} = 9.09 [100] and γ = 0.129 THz [100]. In the visible and near infra-red frequency region, the dielectric constant for GaP is given by [100],

$$\epsilon(\zeta) = 1 + \frac{S_{e1}v_{e1}^2}{v_{e1}^2 - \zeta^2} + \frac{S_{e2}v_{e2}^2}{v_{e2}^2 - \zeta^2} + \frac{S_{e3}v_{e3}^2}{v_{e3}^2 - \zeta^2} \tag{3.14}$$

where the values of the constants are, s_{e1} = 2.570, s_{e2} = 4.131, s_{e3} = 1.390, v_{e1} = 29000, v_{e2} = 42700, v_{e3} = 58000 and ζ is the wave number for the VIS-NIR frequency region expressed in cm^{-1}. Figure 3.1 shows the refractive indices at THz frequencies and the group refractive indices for the optical pulse in the GaP crystal. The phase-matching condition cannot be satisfied in GaP for optical pulses at 800 nm, but it is possible at 6 THz for optical pulse centered at 925 nm. The material properties for crystals to be used as a medium for optical rectification/frequency mixing, can be summarized as the following,

- The materials should possess a high second-order non-linear susceptibility $\chi^{(2)}$.
- They should be transparent at all frequencies involved, otherwise the effective interaction length will be limited by absorption.
- The damage threshold for the materials should be high enough to withstand the high laser intensities involved.
- There preferably should not be any other non-linear process that competes with the desired process.
- There should be a good phase-matching between the pump light and the generated radiation in the material.

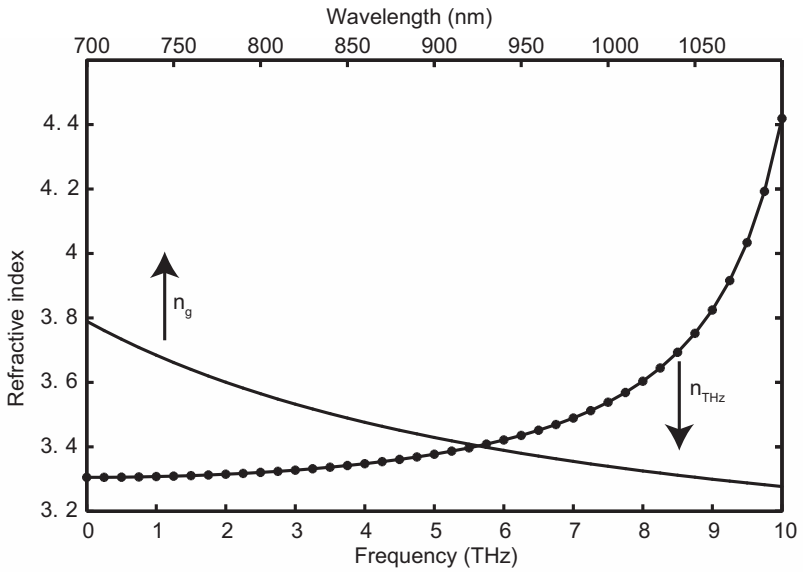

Figure 3.1: Group refractive index of the optical pulse n_g and phase refractive index n_{THz} of THz radiation in a GaP crystal as a function of wavelength/frequency.

3.3 Need for a better spectrometer

A typical THz-TDS setup as described in Fig. 2.4 suffers from a number of problems. First, a typical THz-TDS setup requires parabolic mirrors to collimate, steer and focus the THz radiation onto the detection crystal [101]. Unfortunately, parabolic mirrors are notoriously difficult to align, especially considering that THz radiation is invisible. Second, the long THz beam path through air in a typical THz-TDS setup requires that the beam path be flushed with dry N_2 gas to reduce the absorption of the THz radiation by water vapor molecules in the atmosphere. Third, since optical rectification is usually not very efficient in converting laser light into THz light, losses in the THz beam by diffraction and by absorption at reflecting surfaces in the THz beam path lead to further reductions in the THz power. Fourth, to improve the signal-to-noise ratio (SNR), the pump beam intensity is typically modulated in conjunction with lock-in-detection. However, modulation techniques often cause other problems, such as pulse lengthening when the laser pulses are sent through an acousto-optic modulator, or they cause vibrations when a mechanical chopper is used.

3.4 Quasi-near field THz generation and detection.

One way to overcome these problems is by placing the THz source and detector very close to each other, in the quasi-near field. Quasi-near field THz generation and detection setup makes use of electro-optic crystals for generation and detection of THz radiation. The generation and detection crystals are placed close to each other and the THz pulses are generated and detected with, initially, counter-propagating pump and probe beams. Such a setup does not require parabolic mirrors to steer the THz beam, is intrinsically easy to align and does not suffer from the problems associated with the absorption of THz radiation by the water vapor molecules in the atmosphere. We demonstrate that such a quasi-near field setup gives us relatively strong, broadband signals and allows us to achieve a high SNR without using lock-in detection and without the need to flush the setup with dry nitrogen gas. This kind of setup can easily be used for spectroscopic purposes by placing a sample between the generation and detection crystals.

Figure 3.2 shows the experimental setup. THz radiation is generated by optical rectification of 50 fs, 800 nm pulses from a Ti:sapphire oscillator (Scientific XL, Femtolasers) having a repetition rate of 11 MHz and an average power of 960 mW. The beam from the oscillator is split into two equal parts by a 50/50 beam splitter. One part (pump) is used to generate THz pulses and the other part (probe), is used to detect it. The pump beam is sent to an in-plane retro-reflector mounted on a loudspeaker oscillating at 50 Hz, and is then focused onto a GaP generation crystal. Both generation and detection crystals have an anti-reflection (AR) coating on one surface and a high-reflectivity (HR) coating on the other surface for wavelengths between 700 and 900 nm. The generation crystal has the AR coating on the surface through which the beam enters the crystal, to reduce reflection losses. It has the HR coating on the opposite surface to prevent the pump beam from reaching the detection crystal and the differential detector. THz pulses, generated in the crystal, propagate a short distance of less than 1 mm through air, before entering the detection crystal. From the back of the detection crystal, a synchronized probe pulse is focused onto the front surface, where the THz beam enters the crystal. The THz electric-field elliptically polarizes the probe beam with an amount equal to the instantaneous THz electric-field value [102]. The AR coating on the entrance surface of the detection crystal prevents the probe beam from getting reflected from that surface. The probe beam then goes through the crystal and gets reflected at the HR coating on the front surface after which it is

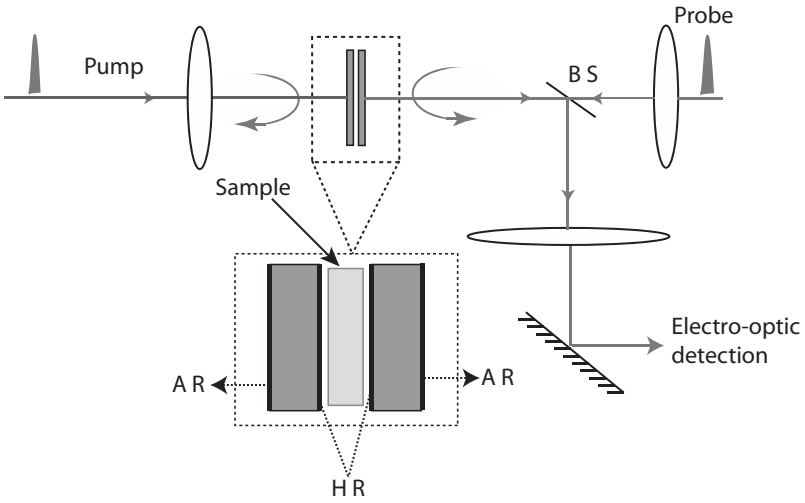

Figure 3.2: Experimental setup to generate and detect THz radiation in the quasi-near field. Both the generation and detection crystals have a high reflectivity (HR) coating on one surface and an anti reflection (AR) coating on the other surface. The detection crystal is placed very close to the generation crystal with the HR surfaces facing each other. The probe beam is reflected back from the HR surface of the detection crystal and a beam splitter (BS) sends the pulse to a conventional electro-optic detection setup.

sent to a differential detector setup. The differential detector setup consists of a quarter-wave plate, a Wollaston prism and a differential detector. Unlike a conventional THz generation detection system, where the THz radiation is focussed onto the detection crystal, here we have a diverging beam entering the detection crystal. This means that the the strength of the signal reaching the detection crystal decreases with increasing distance between the generation and detection crystals. In the detection crystal, the THz electric field elliptically polarizes the probe beam. The optical delay between the pump pulse (and thus the THz pulse) and the probe pulse oscillates at 50 Hz, and a full 20 ps long THz electric-field time-trace is obtained every 20 ms [74]. This setup does not require any modulation of the signal for lock-in-detection and no dry nitrogen flushing is necessary.

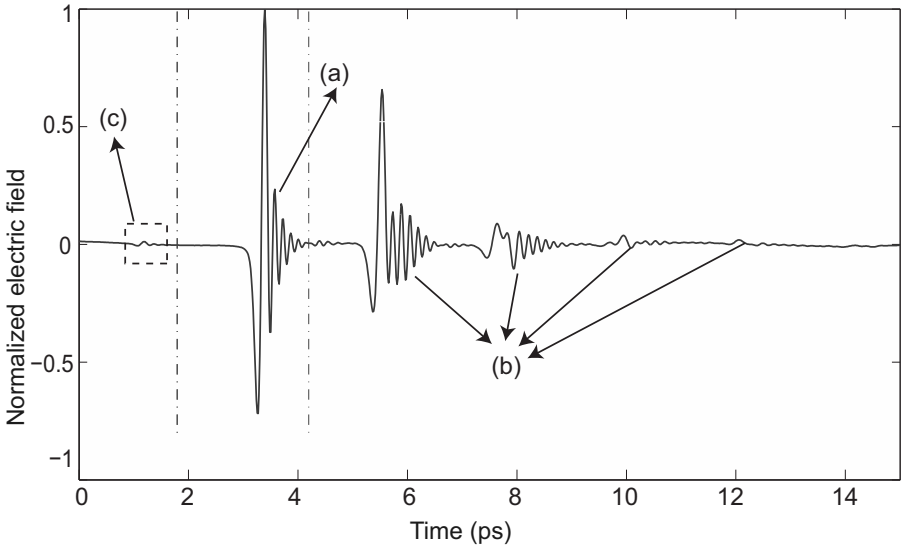

Figure 3.3: A typical THz pulse from the quasi-near field THz generation and detection setup. This pulse is generated and detected using 100 μm (110) oriented GaP crystals. (a) The main THz pulse, (b) the reflections of the THz pulse in the generation and detection crystals, and (c) is the THz pulse sampled by the reflection of probe pulse in the detection crystal.

3.5 Experimental results

We used (110) oriented GaP crystals for the generation and the detection of the THz pulses. A typical THz waveform from the quasi-near field setup is shown in Fig. 3.3. This pulse is generated and detected by (110) oriented GaP crystals of thickness 100 μm. The main THz pulse is marked as (a) and the pulses marked as (b) appearing after the main pulse are from multiple reflections of the THz pulse in the generation and detection crystals. The tiny pulse marked as (c) appearing before the main pulse is the THz pulse sampled by the delayed reflection of the probe pulse in the detection crystal.

Figures 3.4(a)-(c) show the temporal waveforms of the THz pulses detected with a GaP crystal of thickness 300 μm, and generated using GaP crystals of thicknesses 100 μm, 300 μm and 500 μm respectively. Figures 3.4(d)-(f) show their corresponding amplitude spectra. In Fig. 3.5, we plot similar temporal wave forms and spectra to those shown in Fig. 3.4 except,

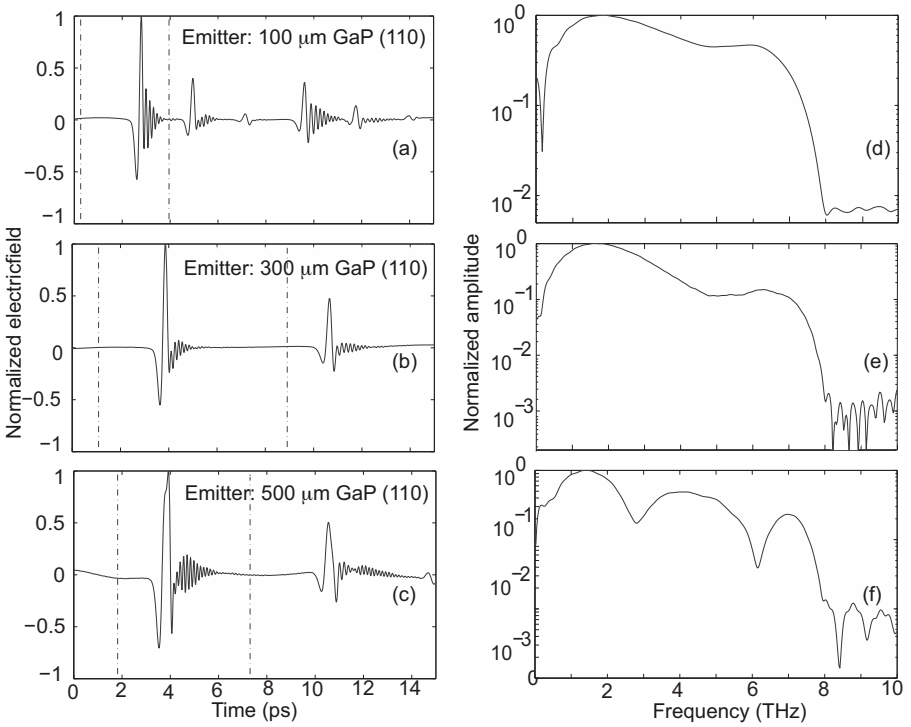

Figure 3.4: (a)-(c) Measured temporal wave forms of THz pulses generated by GaP (110) crystals of different thicknesses and detected very close to the generation crystal with a 300 μm thick GaP (110) crystal and (d-f) their corresponding spectra. The figures are normalized to their maximum.

.

in this case, the THz pulses are detected in a 100 μm thick crystal. In all these cases, the detected THz electric field consists of a nearly single cycle initial pulse, followed by a rapidly oscillating decaying tail. As we will discuss below, this rapidly oscillating tail is due to phase-mismatch in the generation crystal, where the phase velocity of the THz radiation is different from the group velocity of the pump pulse. As mentioned before, the pulse "echoes" appearing after the main pulse are from the reflection of the THz pulse in the generation and detection crystals. These reflections in the time domain will cause periodic oscillations in the frequency domain,

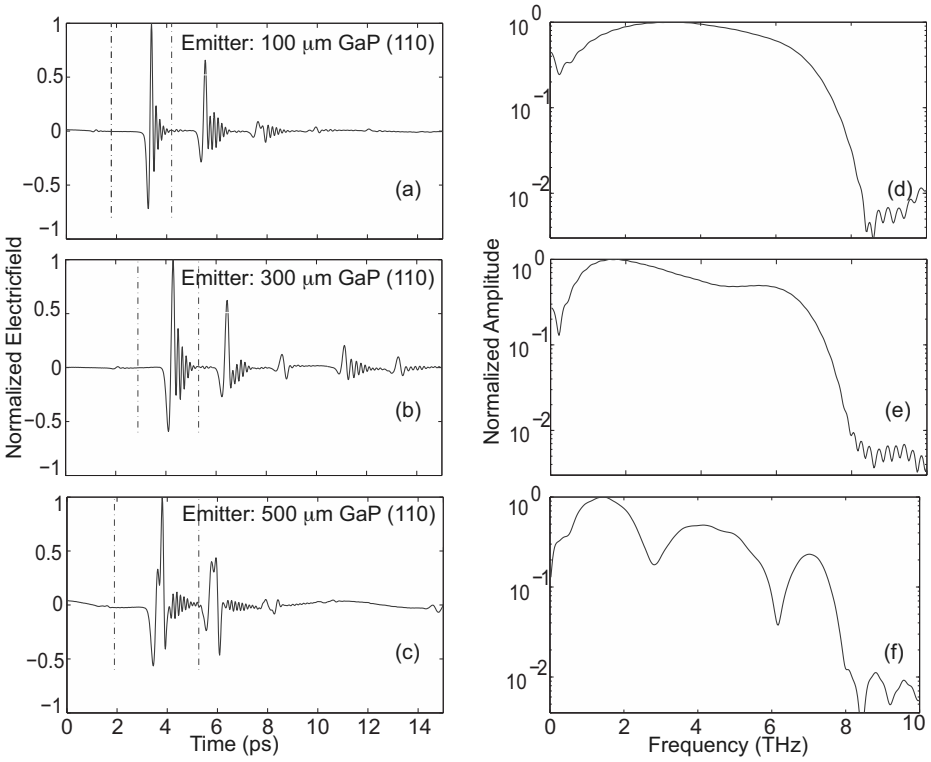

Figure 3.5: (a-c) Measured temporal wave forms of the THz pulses generated by GaP (110) crystals of different thicknesses and detected very close to the generation crystal using a 100 μm thick GaP (110) crystal and (d-f) their corresponding spectra . The figures are normalized to their maxima.

thus complicating the analysis of any spectroscopic measurement. While calculating the spectra we have removed all reflections by taking only the data visible between the two doted lines in Fig. 3.4(a-c) and Fig. 3.5(a-c), and then zero-padded the data out to 40 ps before performing a Fast Fourier Transform (FFT) to calculate the spectra. This gives a step size of 25 GHz in frequency domain. The actual frequency resolution is determined by the actual duration of the pulse in the time domain before zero padding.

A comparison of Figs. 3.4 and 3.5 shows that GaP crystals of 300 μm thickness for both the generation and detection give a similar broad and flat spectrum up to 7.5 THz, compared to the spectra obtained using gen-

eration and detection crystals of 100 μm thickness. The main difference being that the 300 μm crystals have a somewhat attenuated response at the highest frequencies. Even with generation crystals as thick as 500 μm and using a detection crystal of 300 μm, we observe frequencies extending up to 7.5 THz, although the presence of minima in the frequency domain is now very obvious. These are caused by phase-mismatching in the generation crystal [103]. THz radiation originating from different parts of the generation crystal may not necessarily add up constructively because the phase velocity of THz radiation and group velocity of the pump pulse are not equal. This temporal walk-off becomes more dominant as the crystal thickness increases and can cause complete cancellation at some frequencies [103]. For practical purposes, the use of crystals of 300 μm or thicker, is clearly an advantage compared to the use of the more fragile 100 μm crystals. The slow quasi-oscillatory background visible in Fig. 3.4(c) and Fig. 3.5(c) is caused by a slight movement of the pump beam by the loud speaker. Some of this "modulated" pump light reaches the detector and gives rise to a background signal which is synchronous with the loudspeaker. After calibration and fourier transformation, this slow oscillation will appear as low frequency content below 40 GHz in the THz spectrum as seen on Figs. 3.4 and 3.5.

GaP crystals have their transverse optical (TO) phonon resonance at 11 THz, making GaP a very good candidate for generation and detection. The reason for the cut-off seen around 7.5 - 8 THz is not related to phase-matching. Rather, this is caused by the onset of absorption by the TO phonon resonance at 11 THz and the finite duration of the optical laser pulse.

We emphasize that the results are obtained without using any lock-in technique and without flushing the setup with dry nitrogen gas. Notably absent in our measurement is the ringing in the time domain caused by the absorption and re-emission of the THz radiation by water vapor molecules. The optical path length of 1 mm between the two crystals is too small to observe any significant water vapor absorption. The closeness of the two crystals might wrongly suggest that the detection crystal is almost in the near-field region of the emitter. However, for the frequencies from 0.5 - 7.5 THz, this distance is several wavelengths, and thus clearly beyond the near-field. The term quasi-near field is therefore more appropriate. If we define the signal-to-noise ratio (SNR) as the ratio of peak to peak THz electric-field to the root mean square (rms) value of the noise when THz beam is blocked, we achieved a SNR of ≈ 450 in a total measurement time

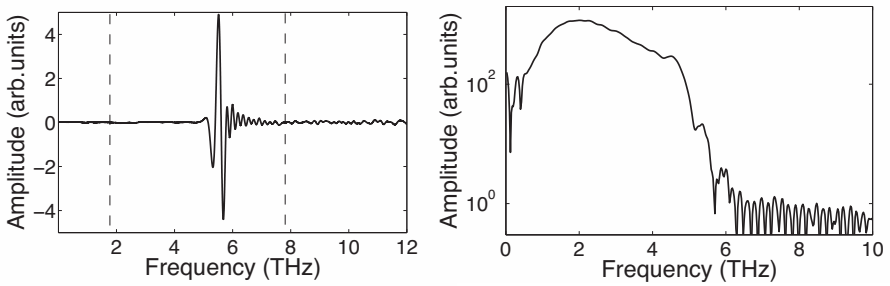

Figure 3.6: THz spectrum generated and detected with GaP crystal of thickness 300 μm in the far-field conventional geometry.

of less than a minute.

We have compared our measurements with a conventional THz generation and detection setup using the generation and detection crystals, tens of centimeters apart, with a standard set of four parabolic mirrors in between. After a difficult alignment and optimization procedure, we then obtained a maximum SNR only half as large as with the quasi-near field method. In addition, this setup required vigorous flushing with dry N_2 gas to reduce THz absorption by water vapor molecules. Fig. 3.6 shows the THz electric field versus time (left) and the spectrum (right), generated and detected with a 300 μm GaP(110) crystal in the far field geometry as shown in Fig. 2.4 in Chapter 2.

3.6 Theoretical modeling

To understand the origin of the shape and the width of the THz amplitude spectrum, we have adapted a recently published model for THz pulse generation and detection [94]. The model includes: (i) the phase matching effects in both generation and detection crystals, (ii) absorption and dispersion of THz radiation in the generation and detection crystals, (iii) Fabry-Perot reflections at the crystal surfaces, (iv) transmission of THz radiation at the crystal-air and air-crystal interfaces. Since our pump and probe pulses are $\approx$ 50 fs long, the dispersion of the generating pulse in the generation crystal is negligible. The THz radiation generated in the

nonlinear medium by optical rectification is given by Eqn. 3.9,

$$E_{Tg}(\omega) = \frac{\sqrt{2}\pi\chi^{(2)}(\omega)}{n_T(\omega)^2 - n_g^2}\tau_p E_0^2 \exp\left[-\frac{\omega^2\tau_p^2}{4}\right]\left[\frac{1}{2}\left(1 + \frac{n_g}{n_T(\omega)}\right)\exp\left(i\omega n_T(\omega) l_g/c\right) + \frac{1}{2}\left(1 - \frac{n_g}{n_T(\omega)}\right)\exp\left(-i\omega n_T(\omega) l_g/c\right) - \exp\left(i\omega n_g l_g/c\right)\right] \quad (3.15)$$

where, l_g is the thickness of the generation crystal. The dielectric function of the crystal in the THz frequency domain $\epsilon(\omega)$ is given by [99]

$$\epsilon(\omega) = \epsilon_{el} + \frac{\epsilon_{st}\omega_{TO}^2}{\omega_{TO}^2 - \omega^2 + 2i\gamma\omega} \quad (3.16)$$

where, ϵ_{st} is the static dielectric constant, ω_{TO} is the angular frequency of TO phonon resonance, and γ is the damping factor. For GaP crystal, ω_{TO} = 11 THz, ϵ_{st} = 2.03, ϵ_{el} = 9.09 and γ = 0.129 THz. Eq. 3.15 takes into account the phase-matching, absorption and dispersion of THz radiation in the generation crystal. While exiting the generation crystal the THz radiation will be partly transmitted and partly reflected at the generation crystal-air interface. This is true for the THz radiation entering the detection crystal, at the air-crystal interface. The coupling of THz radiation out of the generation crystal and coupling into the detection crystal can be described by the transfer functions. The reflection and transmission coefficients for the THz electric field at the crystal-air interface are:

$$R_{in}(\omega) = \frac{\sqrt{\epsilon(\omega)} - 1}{\sqrt{\epsilon(\omega)} + 1}$$
$$T_{in}(\omega) = \frac{2}{\sqrt{\epsilon(\omega)} + 1}$$

At the air-crystal interface the coefficients are:

$$R_{out}(\omega) = \frac{1 - \sqrt{\epsilon(\omega)}}{1 + \sqrt{\epsilon(\omega)}}$$
$$T_{out}(\omega) = \frac{2\sqrt{\epsilon(\omega)}}{\sqrt{\epsilon(\omega)} + 1}$$

In electro-optic detection, the THz pulse and the probe laser pulse propagate through the nonlinear crystal. In the time domain, the detected electro-optic signal is proportional to the cross correlation between the

probe pulse and THz pulse integrated over the thickness of the crystal [104]. The electro-optic signal measured is given by [99],

$$S_{eo-counter} \propto \int_0^{l_d} dz \int_{-\infty}^{\infty} dt I_p E(z,t) \tag{3.17}$$

where, l_d is the length of the electro-optic crystal and I_p is the intensity profile of the probe pulse which is given by [99],

$$I_p = \exp\left\{-\left[z - v_g(t - t_0)\right]^2 / \left(v_g\tau\right)^2\right\} \tag{3.18}$$

where, v_g is the group velocity of the probe pulse. τ is the pulse duration of the probe pulse and τ_{FWHM} is $2\sqrt{\ln 2}\tau$, and t_0 is the delay between the probe and the terahertz pulse. the transfer function for the electro-optic sampling in the detection crystal is,

$$T_{eos} \propto \frac{c}{i\omega(n_T(\omega) - n_g)}\left[\exp(il_d(n_T - n_g)\omega/c) - 1\right]\exp\left(-\tau_p^2\omega^2/4\right) \tag{3.19}$$

The detected THz electric-field is then given by,

$$E_T(\omega) \propto E_{Tg} T_{out} T_{in} T_{eos} \tag{3.20}$$

where, E_{Tg} is given by Eqn. 3.15

Figure 3.7 shows the calculated spectra based on the above model. Figures 3.7(a-c) and (d-f) show THz spectra generated using 100 μm, 300 μm, 500 μm GaP (110) crystals for the generation, and 100 μm, and 300 μm GaP (110) crystals for detection. Overall, the calculated spectra show very good agreement with the experimental results shown in Fig. 3.4. Differences are observed at higher frequencies where the predicted amplitudes are higher than actually measured. A plausible explanation for this is that, in our calculation we do not take into account the group velocity dispersion of the laser pulses in both generation and detection crystals. The pulse will get broadened in the GaP crystals due to dispersion. For a particular crystal thickness, the pulse broadening increases as the pulse width decreases. Figure. 3.8 shows the increase in temporal width of the laser pulse after propagation through 100 μm, 300 μm and 500 μm GaP crystals. Figure. 3.8 shows that after propagation through a 300 μm GaP crystal, a 50 fs (FWHM) Gaussian pulse will be broadened to $\approx$ 60 fs (FWHM). This explains why higher frequencies are less efficiently generated/detected

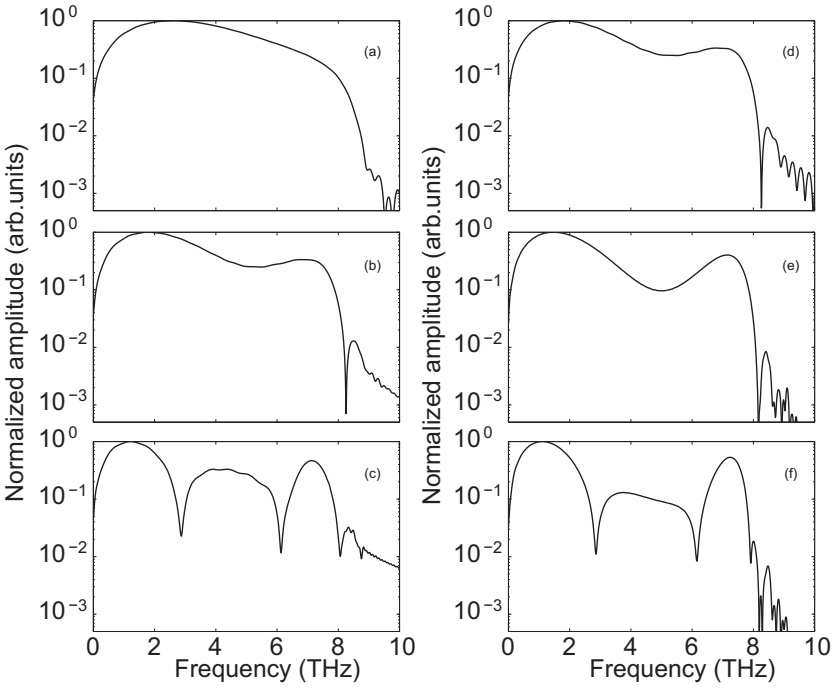

Figure 3.7: (a-c) Calculated spectra of THz radiation generated by GaP (110) crystals of thicknesses 100 μm, 300 μm and 500 μm and detected using a 100 μm thick GaP (110) crystal. (d-f) Calculated spectra of THz radiation generated by GaP (110) crystals of thicknesses 100 μm 300 μm and 500 μm and detected using a 300 μm thick GaP (110) crystal. The calculation takes into account phase-matching effects and absorption of THz radiation in both generation and detection crystals.

in the experiment compared to the calculations. If one wants to increase the generated bandwidth to frequencies above the phonon resonance frequency, then very short laser pulses and very thin crystals should be used. Unfortunately, the signal strength decreases when the crystal becomes thinner. Apart from the fact that thin crystals are difficult to handle, the frequency resolution decreases because of the reduced time separation between the THz reflections and the main THz pulse. In order to overcome this problem, a very thin crystal is typically attached to a thicker crystal of orientation (100), because (100) oriented crystals are not capable of generating or detecting THz radiation in the commonly used experimental geometries.

The dips in the spectrum for the thickest emitter crystal can now be

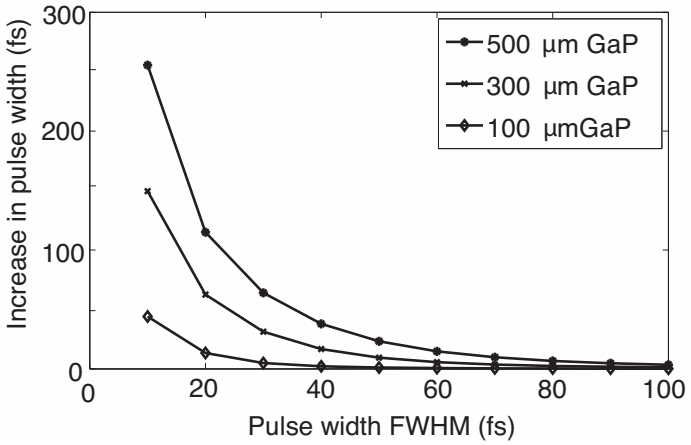

Figure 3.8: Pulse broadening in GaP crystals for crystal thicknesses of 100 μm, 300 μm and 500 μm.

identified as phase-matching minima. The bandwidth could be increased by using shorter pulses. However, shorter pulses will increasingly suffer from group velocity dispersion. This can lengthen the pulse considerably, and is, as stated before, not included in the model.

3.7 Effect of counter propagating probe pulse on the detected THz pulse.

Another important point to note is that the probe and the THz pulses are initially counter propagating and, after reflection, co-propagating in the detection crystal. The detected signal should therefore consists of a counter- and a co-propagating part. However, in our calculation of the THz spectra, shown below, we have assumed that the THz and probe pulses co-propagate in the detection crystal. The agreement between the experiment and calculation strongly suggests that the effect of the counter propagating case to the electro-optic signal is negligible. The electro-optic signal measured is given Eqn. 3.17 [99], The integral in Eq.(3.17) is valid when both the THz beam and the probe beam co-propagate in the crystal. But in this geometry, the THz pulses are initially counter propagating and, after reflection, co-propagating. When the THz beam and probe beam are

counter propagating, I_p is given by,

$$I_p = \exp\left\{-\left[z + v_g\left(t - t_0\right)\right]^2 / \left(v_g\tau\right)^2\right\} \tag{3.21}$$

Some insight can be gained by considering a very simple model in which we assume a delta function $\delta(z + v_g t)$ for the temporal intensity profile I_p of the probe pulse and a plane wave $E(z,t) = \cos(\omega t - k_T z)$ for the THz electric-field. k_T is the THz wave vector along the z axis. If we assume, for the sake of argument, that the magnitudes of THz phase velocity and group velocity of the probe pulse are equal inside the detection crystal and, that the time delay t_0 between the THz pulse and probe pulse is zero, then,

$$\begin{aligned} S_{eo-counter} &= \int_0^l \int_{-\infty}^{\infty} \delta(z + v_g t) E_0 \cos(\omega t - k_T z) dt dz \\ &= \int_0^l \int_{-\infty}^{\infty} \frac{1}{v_g} \delta\left(t + \frac{z}{v_g}\right) E_0 \cos\left(\omega t - kz\right) dt dz \end{aligned}$$

$$S_{eo-counter} \propto \frac{E_0 l_d}{v_g}\left[\frac{\sin\left(2k_T l\right)}{2k_T l}\right] \tag{3.22}$$

In Fig. 3.9 we plot this contribution to the electro-optic (EO) signal, normalized against the contribution of the co-propagating case, as a function of frequency, for a 300 μm thick GaP crystal. The figure shows that the contribution from the counter propagating case is negligible at higher frequencies and shows increasingly larger amplitude oscillations versus frequency when the frequency decreases. Only for frequencies below a few hundred GHz does the contribution to the signal increase to values larger than 10% . This should, perhaps, not come as a surprise. Electro-optic detection is a second-order nonlinear optical process and when the two waves are counter propagating, this represents the largest possible phase-mismatch and thus suggests an extremely low optical conversion process for all frequencies except the lowest.

3.8 Discussions and conclusions

We have presented a simple and efficient method to generate and detect THz radiation with a large bandwidth of 7.5 THz without using any lock-in techniques. Our setup does not need to be flushed with dry nitrogen

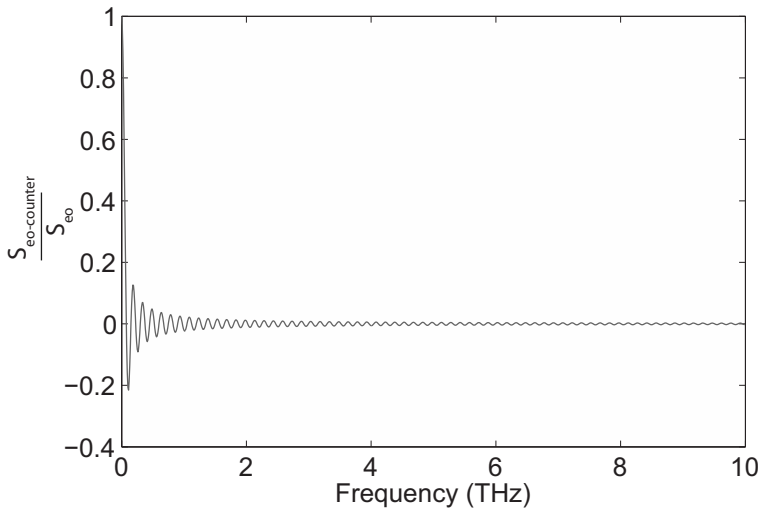

Figure 3.9: The contribution to the measured electro-optic signal from the counter propagating probe pulse, expressed as a fraction of the signal for the co-propagating pulse.

gas because it does not suffer from water vapor absorption. The observed spectra of the generated THz pulses are explained with a simple model which takes into account the effects of phase-matching and absorption of THz radiation in the generation and detection crystals. We have also shown that the effect of counter propagation of THz pulse and probe pulse in the detection crystal is negligible at higher frequencies. Finally, we would like to speculate on the application of pump beam modulation techniques to further improve the signal-to-noise ratio. As pointed out in the introduction, pump modulation techniques can create their own problems such as mechanical vibrations or pulse lengthening. If those problems can be minimized, then modulating the pump beam with consecutive lock-in detection, may lead to further improvements of the signal-to-noise ratio. An attempt by us to implement this using an elasto-optic modulator operating at a fixed frequency of 50 kHz did not succeed due to excessive pump laser noise in this modulation frequency range. It is likely that the future use of better modulation techniques will improve our current setup even further.

4

Some applications of the quasi-near field spectrometer

4.1 Introduction

Terahertz spectroscopy is a powerful technique for material studies in the range of frequencies from a few hundred gigahertz to tens of terahertz. THz generation and detection methods based on nonlinear optics and femtosecond laser pulses have made a large number of applications of terahertz technology possible. The coherent nature of the THz generation and detection makes it possible to measure the THz electric field, rather than the intensity. This makes it possible to measure the dielectric function (absorption coefficient and index of refraction) of the materials without having to rely on fairly complicated Kramers-Kronig relations to calculate the frequency dependent absorption from the measurement of the frequency dependent refractive index or vice versa. The broadband nature of THz-TDS has been exploited for materials identification and characterization [105]. Other, early, applications of THz-TDS include moisture analysis [10, 106], package inspection [3, 10, 106], biomedical diagnostics [107] and gas sensing [108]. In many of these imaging applications, apart from getting a THz image, the measurement also gives spectroscopic information on the samples under study, which can be used to identify molecular crystals, for example.

THz spectroscopy bridges the gap between microwave spectroscopy and mid-infrared spectroscopy. In the gas phase, a number of molecules have rotational absorption lines: for example, dichloromethane has rotational lines with transitions up to 2.5 THz. In the solid crystalline phase the atoms or molecules are held close to their equilibrium positions by attractive and repulsive forces. This leads to collective lattice vibrations, or phonons, of the crystals at certain frequencies. The vibrational modes in the THz frequency region are characteristic for the molecule and are influenced by the environment it finds itself in. Usually, the feature-rich dielectric spectra observed in crystalline or poly-crystalline materials are most likely due to the combination of phonons and intramolecular modes of the molecules.

In amorphous materials, spectrally localized features rarely exist at THz frequencies due to strong coupling between the random environment and intramolecular modes [109]. Long range order in the solid state is necessary to observe sharp spectral features at THz frequencies. This means that THz spectroscopy also provides information on the crystallinity of a material. Water and liquids in general have a fairly featureless absorption spectrum on a background increasing with frequency over the THz frequency range. This background is due to the superposition of a continuum of rotational modes in liquids [110–112]. In spite of the lack of spectral features in the THz absorption spectrum of amorphous materials and aqueous solutions, there have been reports that it is possible to identify the ingredients and their concentration in solution [113]. Fig. 4.1 shows the part of the electromagnetic spectrum around the THz region, showing the frequencies at which different excitations can occur. We measured the THz absorption spectra of 8 amino acids in the form of polycrystalline powder. The spectra are measured in the frequency range of 0.5 - 7 THz, using the quasi-near field spectrometer described in Chapter 3.

4.2 Data analysis in THz transmission spectroscopy

In THz spectroscopy, the THz pulses are recorded twice. First without the sample to be characterized and then with the sample. The measured signal is proportional to the electric field of the THz pulse, $\boldsymbol{E(t)}$. To get the frequency domain information, we Fourier transform the signal $E(t)$

$$E(\omega) = \frac{1}{2\pi} \int_{-\infty}^{+\infty} e^{-i\omega t} E(t) dt. \tag{4.1}$$

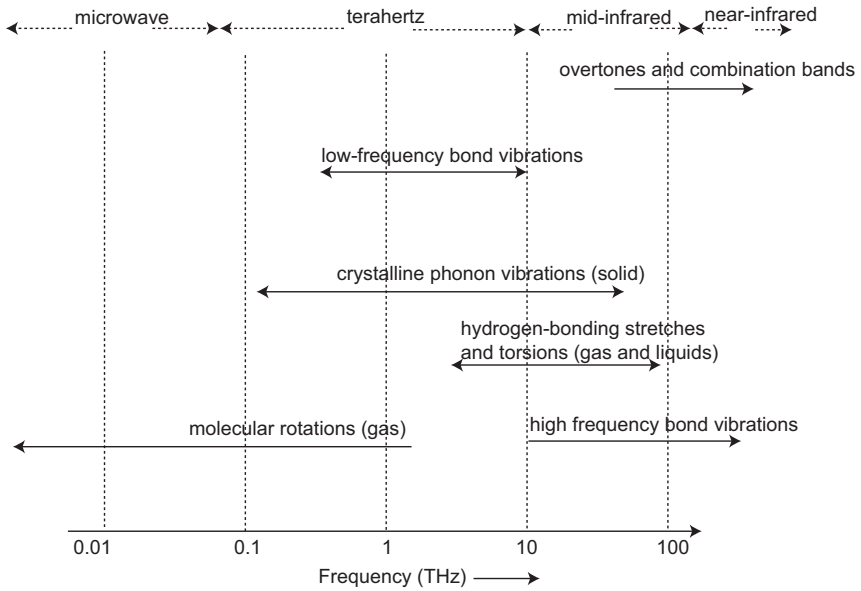

Figure 4.1: The electromagnetic spectrum in the THz region showing the regions where different excitations can occur [114].

We call the pulse propagated through the sample, the sample pulse, E_s and the pulse propagated through a volume of air of equal thickness, the reference pulse, E_r. Instead of E_r being measured in air, it can be measured in any other reference material with known dielectric function. From the Fourier transforms of the sample pulse, E_s and the reference pulse E_r, it is possible to extract the information about the dielectric function (absorption coefficient and refractive index) of the sample. Fig. 4.2 shows the schematic representation of THz-TDS in a transmission geometry. The THz signal is transmitted through a sample of thickness d. The sample signal carries information about both the absorption coefficient and the refractive index of the sample. The basic assumptions made in this geometry are

- The sample is a homogenous slab with two flat, smooth and parallel surfaces and has a well defined thickness. The scattering of the THz radiation from the surface of the sample is negligible.
- THz pulses are normally incident on the sample.
- Both the reference signal and sample signal are measured under the

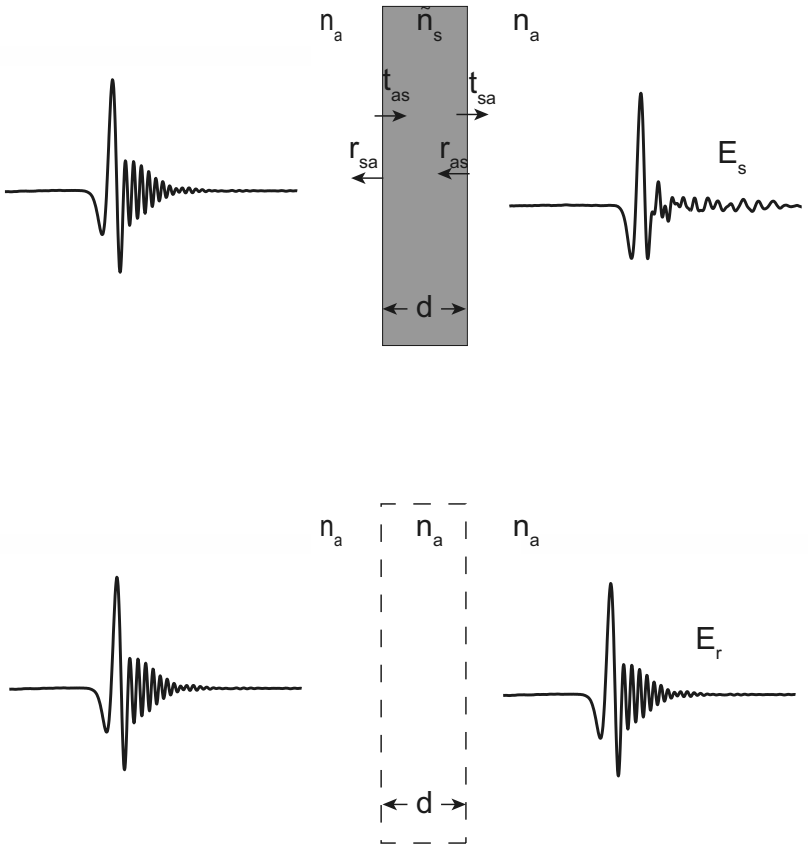

Figure 4.2: The basic scheme of a THz-TDS transmission experiment. The sample has a thickness d and complex refractive index $\tilde{n}_s$. The sample signal, E_s is the signal transmitted through the sample of thickness d and the reference pulse, E_r is the signal transmitted through an equal thickness of air or any other material whose complex refractive index is known. r_{sa}, t_{as}, r_{as} and t_{sa} are the amplitude reflection and transmission coefficients at the front and back of the sample, respectively. n_a is the refractive index of air.

same conditions.

- The electromagnetic response of the medium is linear.
- The medium surrounding the sample is air and has a refractive index of n = 1 and zero absorption.

t_{as} and t_{sa} are the the Fresnel amplitude coefficients for the transmission of electric field from air to sample at the air-sample boundary and sample to air at the sample-air boundary respectively. The Fresnel amplitude coefficients for transmission t_{as} and t_{sa} are given by [115] ,

$$t_{as} = \frac{2}{1 + \tilde{n}(\omega)} \tag{4.2}$$

$$t_{sa} = \frac{2\tilde{n}(\omega)}{1 + \tilde{n}(\omega)} \tag{4.3}$$

where, $\tilde{n}(\omega)$ is the complex refractive index of the sample. The real part of $\tilde{n}(\omega)$ gives the refractive index of the sample and the imaginary part is related to the absorption coefficient. In the frequency domain, the electric field transmitted through the sample is,

$$E_s(d, \omega) = E_0(\omega) t_{as} P_s(d, \omega) t_{sa} \tag{4.4}$$

$E_0(\omega)$ is the THz electric field incident on the sample. The phase factor is given by,

$$P_s(d, \omega) = \exp\left(-i\phi_s(d, \omega)\right) \tag{4.5}$$

with $\phi_s(d, \omega)$ the phase acquired by the THz pulse after being propagated through the sample of thickness d:

$$\phi_s(d, \omega) = k_s(\omega) d \tag{4.6}$$

where $k_s(\omega)$ is the wave vector of the sample pulse, and it is given by $k_s(\omega) = k_s'(\omega) + ik_s''(\omega) = \tilde{n}_s(\omega)\omega/c$. $\tilde{n}_s$ is the complex refractive index of the sample, whose real part is the refractive index of the sample and whose imaginary part is related to the absorption coefficient of the sample. Substituting for the Fresnel amplitude transmission coefficients from Eqns. 4.2 and 4.3, the THz electric field transmitted through the sample is,

$$E_s(d, \omega) = \frac{4\tilde{n}(\omega)}{(1 + \tilde{n}(\omega))^2} E_0(\omega) \exp\left(-ik_s(\omega) d\right) \tag{4.7}$$

In almost all the measurements we performed, the sample is mixed with polyethylene powder (PE) to dilute the sample so that the absorption peaks are not too strong and are within the dynamic range of the system. This means that $\tilde{n}$ is the complex refractive index of the sample and PE powder mixture. PE powder does not have any sharp absorption features in the THz frequency region. For calculating the Fresnel transmission coefficients, we now assume that $\tilde{n}(\omega) = n_{PE}$, where n_{PE} is the refractive index of the PE powder. Eqn. 4.7 will now become,

$$E_s(d,\omega) = \frac{4n_{PE}}{(1+n_{PE})^2} E_0(\omega) \exp\left(-ik_s(\omega)d\right) \tag{4.8}$$

The intensity of THz pulses $I_s(\omega)$ transmitted through the sample is given by,

$$I_s(d,\omega) \propto E_s(d,\omega)E_s^*(d,\omega) \propto \exp\left(2k_s''(\omega)d\right) \tag{4.9}$$

By Lambert-Beer's law, the intensity of light after transmission through a material of thickness d and absorption coefficient α can be written as,

$$I_s(d,\omega) = I_0(\omega) \exp\left(-\alpha(\omega)d\right) \tag{4.10}$$

Now we can relate $k_s''(\omega)$ to the absorption coefficient of the sample through the equation given by,

$$\alpha(\omega) = -2k''(\omega) \tag{4.11}$$

The refractive index of the sample $n(\omega)$ can be calculated from the real part of $k_s(\omega)$ by the equation,

$$n(\omega) = \frac{k'(\omega)c}{\omega} \tag{4.12}$$

For the reference pulse there are no reflections at the interfaces and only the phase accumulated by propagating through air of thickness d has to be known. The reference pulse is given by,

$$E_r(d,\omega) = E_0(\omega)P_r(d,\omega) \tag{4.13}$$

$$P_r(d,\omega) = \exp\left(-ik_r'(\omega)d\right) \tag{4.14}$$

$k_r'' \approx 0$, because of the negligible absorption by air. The ratio of the sample pulse to the reference pulse in the frequency domain is given by,

$$\frac{E_s(d,\omega)}{E_r(d,\omega)} = K \exp\left(-i\left(k_s'(\omega) - k_r'(\omega)\right)d + k_s''(\omega)d\right) \tag{4.15}$$

where $K = \frac{4n_{PE}}{(1+n_{PE})^2}$ is a constant. Taking natural the logarithm on both sides,

$$\ln\left(\frac{E_s(d,\omega)}{E_r(d,\omega)}\right) = \ln K - i\left(k_s'(\omega) - k_r'(\omega)\right)d + k_s''(\omega)d \tag{4.16}$$

$E_s(d,\omega)$ and $E_r(d,\omega)$ are both complex valued electric fields obtained by taking the FFT of $E_s(d,t)$ and $E_r(d,t)$ respectively,

$$E_s(d,\omega) = E_s'(d,\omega) + iE_r''(d,\omega) \tag{4.17}$$
$$E_r(d,\omega) = E_r'(d,\omega) + iE_r''(d,\omega) \tag{4.18}$$

so that,

$$\ln\left(\frac{E_s(d,\omega)}{E_r(d,\omega)}\right) = \ln\left(\frac{E_s'(d,\omega) + iE_s''(d,\omega)}{E_r'(d,\omega) + iE_r''(d,\omega)}\right) \tag{4.19}$$
$$= \ln\left(Y_1 + iY_2\right) \tag{4.20}$$

where,

$$Y_1 = \frac{E_r'(d,\omega)E_s'(d,\omega) + E_r''(d,\omega)E_s''(d,\omega)}{E_r'^2(d,\omega)E_r''^2(d,\omega)} \tag{4.21}$$

$$Y_2 = \frac{E_r'(d,\omega)E_s''(d,\omega) - E_r''(d,\omega)E_s'(d,\omega)}{E_r'^2(d,\omega)E_r''^2(d,\omega)} \tag{4.22}$$

$$\ln\left(\frac{E_s(d,\omega)}{E_r(d,\omega)}\right) = \ln\left(\sqrt{Y_1^2 + Y_2^2}\exp\left(i\arctan\left(\frac{Y_1}{Y_2}\right)\right)\right) \tag{4.23}$$

Sustituting from Eqn. 4.16 we get,

$$\ln\left(\sqrt{Y_1^2 + Y_2^2}\right) + i\arctan\left(\frac{Y_1}{Y_2}\right) = \ln K - i\left(k_s'(\omega) - k_r'(\omega)\right)d + k_s''(\omega)d \tag{4.24}$$

Equating real and imaginary parts of Eqn. 4.16 and using Eqns. 4.23 and 4.12 we get,

$$\frac{1}{2}\ln\left(Y_1^2 + Y_2^2\right) = \ln K + k_s''(\omega)d \tag{4.25}$$

$$\arctan\left(\frac{Y_1}{Y_2}\right) = -\left(k_s'(\omega) - k_r'(\omega)\right)d \tag{4.26}$$

$$\alpha(\omega) = -2k_s''(\omega) = -\frac{1}{d}\ln\left(Y_1^2 + Y_2^2\right) + \frac{2}{d}\ln K \tag{4.27}$$

$$n_s(\omega) = \frac{k_s'(\omega)c}{\omega} = \frac{c}{\omega d}\arctan\left(\frac{Y_2}{Y_1}\right) + 1 \tag{4.28}$$

for a sample placed in air $\frac{k'_r(\omega)}{\omega} = 1$. Thus the absorption coefficient and refractive index of the sample can be calculated from $E_s(t)$ and $E_r(t)$. The term $\frac{2}{d} \ln K$ in the equation for absorption coefficient gives rise to a background in the calculated absorption coefficient. This background is not due to the absorption of the THz electric field by the PE powder but is due to the reflection losses at the boundaries of the sample. In order to calculate the absolute absorption coefficient one should know the exact values for the reflection and the transmission loss. We however are interested only in the positions of the absorption lines in a sample rather than the absolute value for the absorption coefficient. This means that we can ignore the term $\frac{2}{d} \ln K$ in calculating the "absorption coefficient" of the sample.

4.3 Broadband THz absorption spectra of some materials

The absorption spectra of many materials are still unknown in the frequency region from 0.1- 10 THz because of lack of efficient sources and detectors with a good SNR in this range. We have measured the absorption spectra of some materials in the frequency range of 0.5 to 7.5 THz to show the applicability of the quasi-near field THz spectrometer. Because of the finite dynamic range of the spectrometer, using pure samples may lead to too much absorption and thus to small signals outside the dynamic range of our system. Thinner samples are required in order to obtain a good spectrum. This, however, introduces at least two complications. First, thin pellets are often fragile and second, etalon reflections occur shortly after the main pulse leading to spectral artifacts. The common solution to these problems is to dilute the sample with a transparent filling material to produce a thicker and less absorbing sample. PE powder is one such filling material, which has no absorption features and negligible absorption in the THz frequency region.

The PE powder we use is Mipelon XM-220 (Mitsui Chemicals America, Inc). It has an average particle size of ≈ 30 μm. The actual sample is ground using a mortar and pestle to reduce the particle size. It is important to minimize the particle size to reduce the scattering and to minimize the Christiansen effect,[1] which leads to spectral distortions [116]. The per-

[1] When certain light is transmitted through a medium with suspended particles, for that wavelength for which the refractive index of the particle is equal to that of the medium, the system behaves like a plane-parallel, homogeneous disk and allows transmission. All other wavelength ranges of the spectrum are reflected, scattered as well as refracted at the

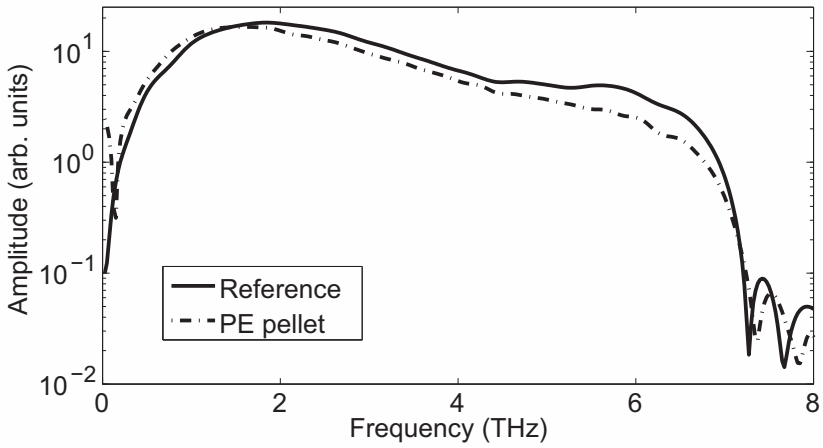

Figure 4.3: THz spectrum transmitted through a PE pellet of thickness 0.61 mm along with the reference spectrum

centage of the sample in the sample-PE powder mixture depends on how strongly the sample absorbs and this can only be determined experimentally by changing the mixing ratio. The mixture is pressed to a pellet of thickness of about 0.5 mm and a diameter of 1 cm, by applying a pressure of about 10 tons with a hydraulic press (Specac LTd, UK). Two measurements are taken, one with the pelleted sample sandwiched between the generation and detection crystal in the quasi-near field spectrometer and one without the sample. These two electric fields as a function of time are used to calculate the refractive index and absorption coefficient of the sample. The thickness of the sample is measured using a Vernier Caliper.

Figure 4.3 shows the spectrum of THz pulse transmitted through a PE pellet of thickness 0.6 mm and the reference spectrum (THz pulse transmitted through air of thickness 0.6 mm). There is some decrease in the amplitude of the THz pulses transmitted through the PE pellet, as the frequency increases. This can be due to scattering and absorption, as both increase as the frequency increases. However, no sharp absorption fea-

many interfaces between substance and liquid. The bandwidth of the transmitted light depends on the characteristic size and shape of the suspended particles. This effect is known as Christiansen effect.

tures are observed. The decrease in THz signal transmitted through the PE pellet as the frequency increases will give rise to a background which is increasing with frequency in the absorption spectra of samples which are mixed with PE powder. In principle, it is possible to get rid of this background by using the pure PE pellet which contains exactly the same amount of PE powder as in the sample pellet as a reference, instead of using air as a reference. We have not done this as it is possible to find the absorption band positions of the sample material even with this background. A measurement on such a PE pellet, however may be necessary to calculate the exact absorption coefficient of the sample.

It can be seen from Fig. 4.3 that the THz electric field amplitude measured with the sample (PE pellet) is higher than without the sample below about 1.5 THz. This will give rise to an apparent negative absorption coefficient for the sample. This is explained as follows. The THz radiation is generated locally by the focused pump beam. The THz beam diameter at the front surface of the sample will thus be determined by the diameter of the focused pump beam and is estimated to be on the order of 100 μm. As the THz beam propagates through, the beam is expected to show a frequency-dependent divergence. Lower frequencies show larger divergence than the higher frequencies. When the sample is placed between the generation and detection crystals, divergence of the lower frequency components is reduced due to a weaker diffraction. This gives rise to an increased amplitude at lower frequencies, than at higher frequencies which suffer less from diffraction to begin with. This gives an increased signal amplitude in the case of a THz pulse transmitted through the sample than through air. In principle, this effect can be reduced by using pump beams having a larger diameter or by decreasing the distance between the two crystals to a fraction of a wavelength, which will also increase the signal amplitude. It will be clear from the following examples, however, that the apparent negative absorption does not pose any problem in identifying the spectral features in the absorption spectra of samples.

4.3.1 D-tartaric acid

Tartaric acid is a white crystalline organic compound with chemical formula, $C_4H_6O_6$. It is found in many plants, grapes, banana, tamarinds, and many other fruits. It gives a sour taste to the fruits. Naturally occurring tartaric acid is a chiral molecule, meaning that its molecular structure is non-superimposable on its mirror-image. Naturally occurring forms of tartaric acid are L-tartaric acid and D-tartaric acid. The mixture of the

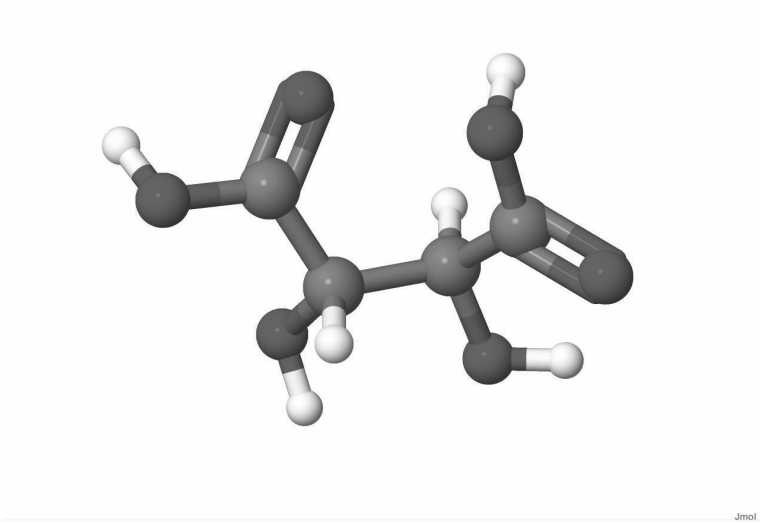

Figure 4.4: Chemical structure of D-tartaric acid molecule. The black balls represent oxygen atoms, grey balls carbon atoms and white balls hydrogen atoms. Made by Jmol: an open source Java viewer for chemical structures in 3D. http://www.jmol.org

two-forms, known as a racemic mixture, is made artificially by mixing L-form and D-form in the ratio of 1:1. The THz absorption spectra of both D-tartaric acid and L-tartaric acid in pure form are the same as the molecular structure is the same. But the racemic mixture shows a completely different absorption spectrum compared to that of their individual components [117]. Fig. 4.4 shows the molecular structure of D-tartaric acid created by the open source Java viewer Jmol. We measured the THz absorption spectra of D-tataric acid in the frequency range of 0.5 - 7.5 THz.

The D-tartaric acid crystallites are ground to a fine powder with the mortar and pestle and mixed with PE powder in the D-tartaric acid to PE powder ratio of 30:100. The thickness of the pellet was about 0.6 mm. Fig. 4.5 (b) shows absorption spectra of D-tartaric acid calculated from the spectra shown in Fig. 4.5 (a). All the spectral features are marked with arrows. It can be seen from Fig. 4.5 (a) that the electric field amplitude observed without the sample is lower than with the sample below 2.2 THz. This translates into an apparent negative absorption in Fig. 4.5 (b). As explained in the previous section, this is due to the fact that lower frequen-

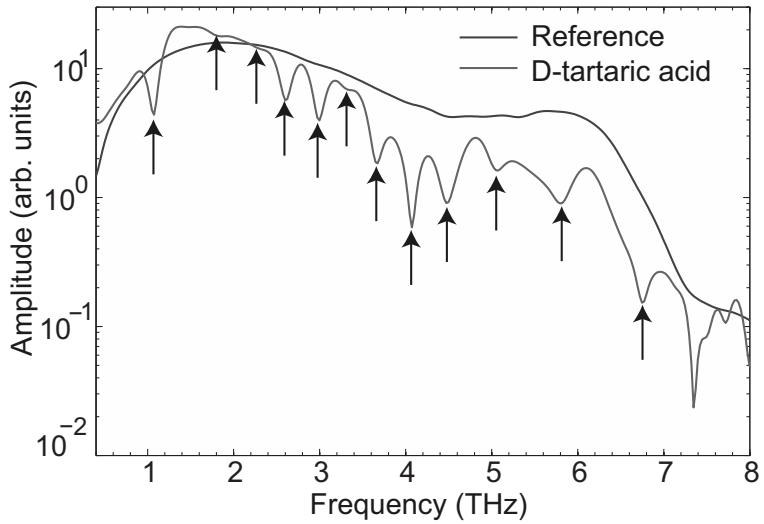

(a)

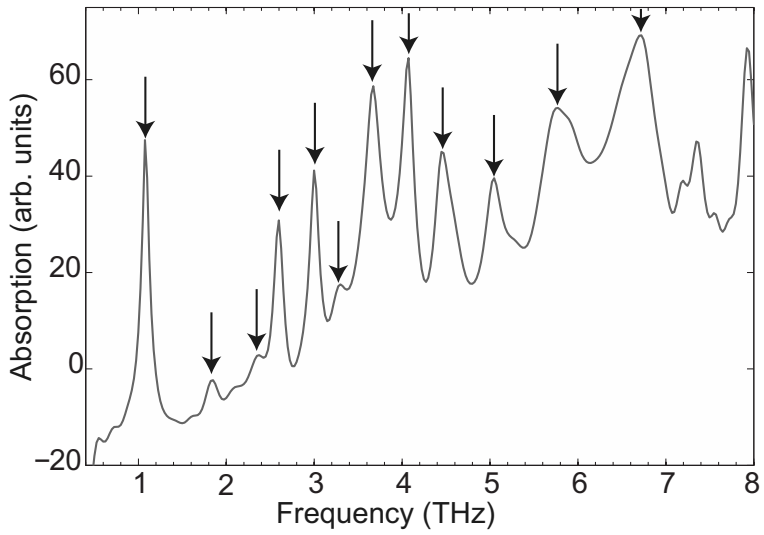

(b)

Figure 4.5: (a) The frequency spectra measured with and without the D-tartaric acid pellet placed in between the generation and detection crystals. (b) The absorption spectrum of D-tartaric acid calculated from (a). The arrows indicate the THz absorption band positions.

cies suffer less from diffraction when transmitted through the sample than through the air and are more effectively detected by the probe pulse. Our THz measurements are in agreement with earlier published spectra which however, only measured the absorption spectra of D-tartaric acid for frequencies up to 3.5 THz [6,117]. Note that our quasi-near field spectrometer covers a much larger frequency range.

4.3.2 Lactose and sucrose

Lactose and sucrose are different forms of sugar. They are disaccharides (Carbohydrates), having the same molecular formula $C_{12}H_{22}O_{11}$, but with a different molecular arrangement. Sucrose is made up of glucose and fructose while lactose is made up of glucose and galactose. Lactose is mostly found in milk and is sometimes called milk sugar. Sucrose is mostly found in plants. Figure 4.6 shows the molecular structure of lactose and sucrose. The sucrose and lactose molecules are connected with the neighboring molecules via several weak hydrogen bonds [118]. Since the molecules are heavy and bonds between them are weak, the vibrational modes of the hydrogen bonds have resonance frequencies in THz region [119]. In general the far-infrared dielectric properties of sugars in the crystalline or polycrystalline form are dominated by vibrational modes of their intermolecular hydrogen bonded network [120]. The THz absorption spectra of polycrystalline monosaccharides and disaccharides in the frequency range of 0.5 - 4 THz have been measured by THz spectroscopy [109]. Far infrared spectra of polysaccharides including lactose and sucrose have been measured with Fourier transform spectroscopy (FTS) in the frequency range of 1 - 20 THz at 100 K [121]. As described before, the lactose and sucrose samples are mixed with PE powder to obtain a sample-to-PE powder ratio of 20:100. This mixture is pressed to a pellet of thickness $\approx$ 0.6mm and 1 cm in diameter. We call this pellet the sample pellet. Fig. 4.7 (a) and (b) respectively shows the spectra of transmitted THz pulse and the THz absorption spectra of sucrose and lactose sample pellets. Even though they have the same chemical formula, the THz absorption spectra are clearly distinct from each other. Most of the spectral features shown are from lattice modes involving intermolecular hydrogen bonds [121, 122]. There are no other reports showing the absorption spectra of lactose and sucrose in the THz frequency region of 0.5 - 7 THz using THz-TDS, which is generally superior to FT spectroscopy in both sensitivity and dynamic range. The THz absorption spectrum of sucrose measured by Walther et al. at 300 K [109] with THz-TDS in the frequency range of 0.2 - 4 THz is too noisy

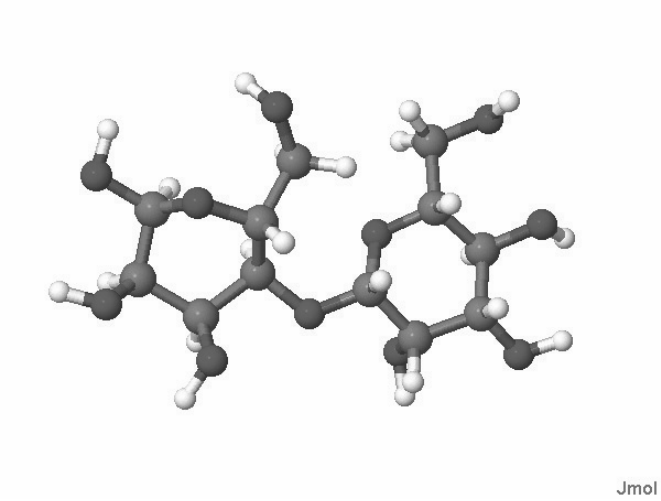

(a)

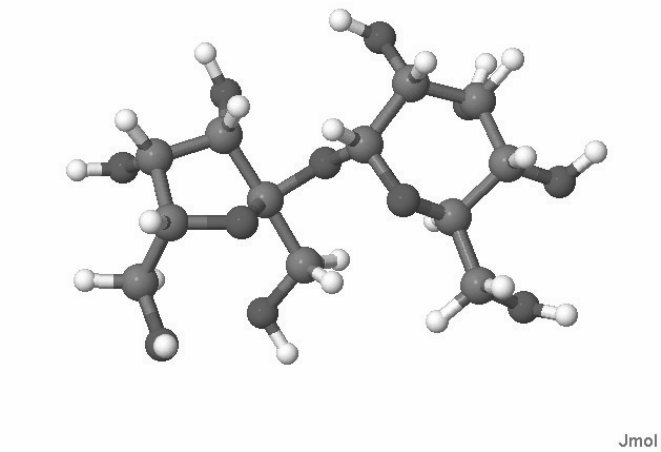

(b)

Figure 4.6: (a) Molecular structure of (a) lactose and (b) sucrose under the same viewing angle. Black balls represent oxygen atoms, grey balls carbon atoms and white balls represent hydrogen atoms.

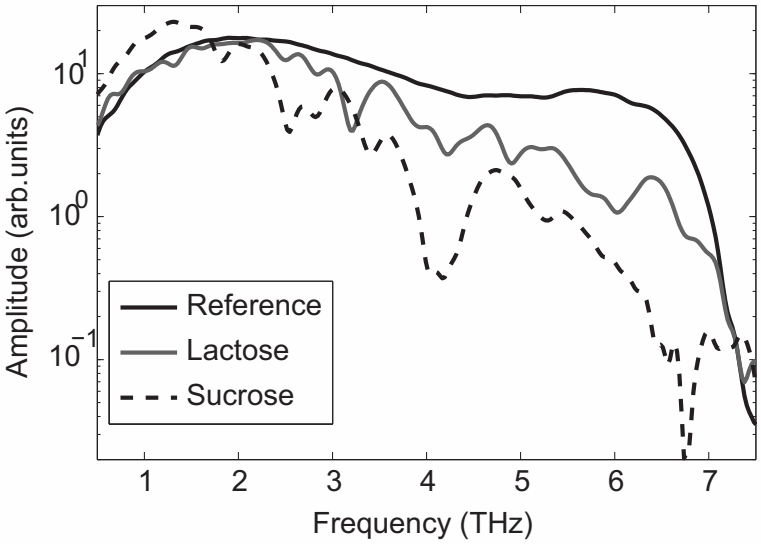

(a)

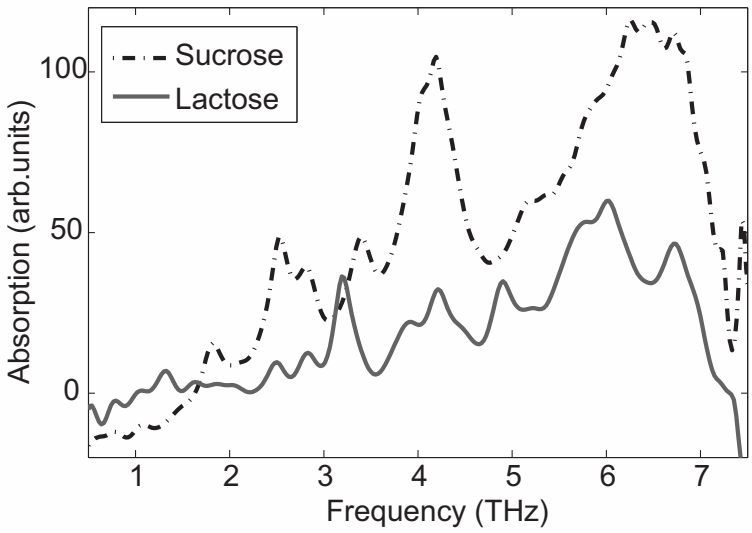

(b)

Figure 4.7: (a) THz frequency spectra of lactose and sucrose along with the reference spectrum. (b) The absorption spectra of lactose and sucrose calculated from (a).

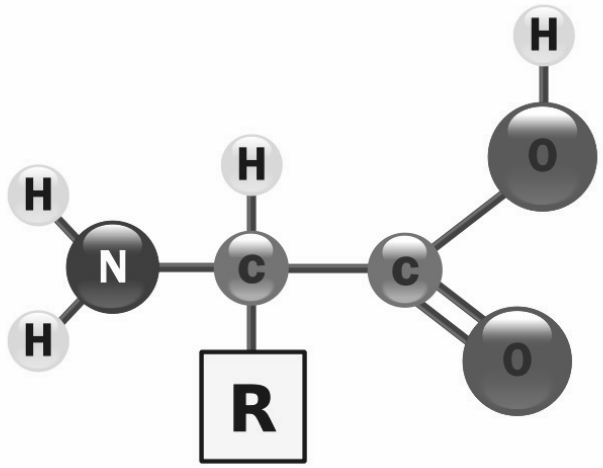

Figure 4.8: General structure of an α-amino acid with the amino group on the left and carboxyl group on the right. Amino acids differ from each other depending on the side chain R

to see any distinguishable spectral features above 3 THz. The absorption spectrum of sucrose measured by the quasi-near field spectrometer shows good agreement with the measurement done by Walther et al. [109]. This provides further evidence of the applicability of the quasi-near field spectrometer.

4.3.3 Amino acids

Amino acids are molecules containing both amine and carboxyl functional groups attached to the same carbon atom, called alpha carbon and such amino acids are known as alpha-amino acids. The alpha-amino acids have the general formula $H_2NCHRCOOH$, where R is the organic substituent. Fig. 4.8 shows the general structure of α-amino acid. The side chain R can be different depending on the amino acid. Amino acids are the back bones of proteins, which are linear chains of amino acids, and nourishing substrates in the human body. There are more than 300 amino acids listed in the practical handbook of biochemistry and molecular biology. Only 20 amino acids are used to synthesize proteins, and are known as standard amino acids. The standard amino acids are classified on the basis of the R group attached to the carbon. Almost all of the proteins contain only L-

amino acids.

THz-TDS is a very promising tool for amino acid molecules characterization because, most of these molecules possess a spectral signature in the THz region (0.1 - 10 THz). A better understanding of the proteins and their functions is possible by the detailed analysis of the structure and dynamics of the amino acids. It has been suggested that an atomic level picture of proteins and amino acids can be obtained through the accurate measurement of low frequency vibrational spectra, which lie in the THz frequency region [18, 123, 124]. It is necessary to know the THz spectra of the amino acids and other bio-molecules in their natural aqueous-phase environment, but this is not easily feasible because, the absorption features of these molecules will be masked by the stronger absorption of THz radiation by the solvent and affected by the solvent too.

Many amino acid crystals are formed from relatively independent sublattice links by the formation of intermolecular hydrogen bonds between amine hydrogen atoms and carboxylate oxygen atoms [125]. THz-TDS measurements on amino acid powder have shown the presence of the vibrational modes of weak hydrogen bonds. The lattice vibrations and hydrogen bond bending occur in the frequency region of 0.1 - 12 THz [126]. The most intense bands in the spectra belong to the molecular vibrations; lattice vibrations are present below 3 THz and they have much lower intensity [127]. Here, we measure absorption spectra of eight amino acids in a broad THz spectral region (0.5 - 7 THz). In fact, the absorption spectra of amino acids in the solid form at 100K and 298 K have been measured with FT spectroscopy (FTS) in the frequency range of 1 - 20 THz [121, 127]. Attempts were made by Korter et al. to compare the experimentally measured THz absorption spectra to calculations based on density functional theory and in the case of serine and cysteine with reasonable success. Many higher frequency internal modes were assigned but lower frequency intermolecular and phonon modes needed more advanced calculations [126].

Here we show measured THz absorption spectra of amino acids namely, L-alanine, L-cysteine, L-glutamic acid, L-leucine, L-threonine, L-tryptophan, L-tyrocine and L-valine. Figures 4.9-4.11 show the THz absorption spectrum of the 8 amino acids measured with the quasi-near field THz spectrometer at a temperature of 291 K. As mentioned before, the absorption coefficient is an effective absorption coefficient that refers to certain amount of amino acids dispersed homogeneously through the volume of the sample pellet. This absorption coefficient is linearly proportional to the bulk

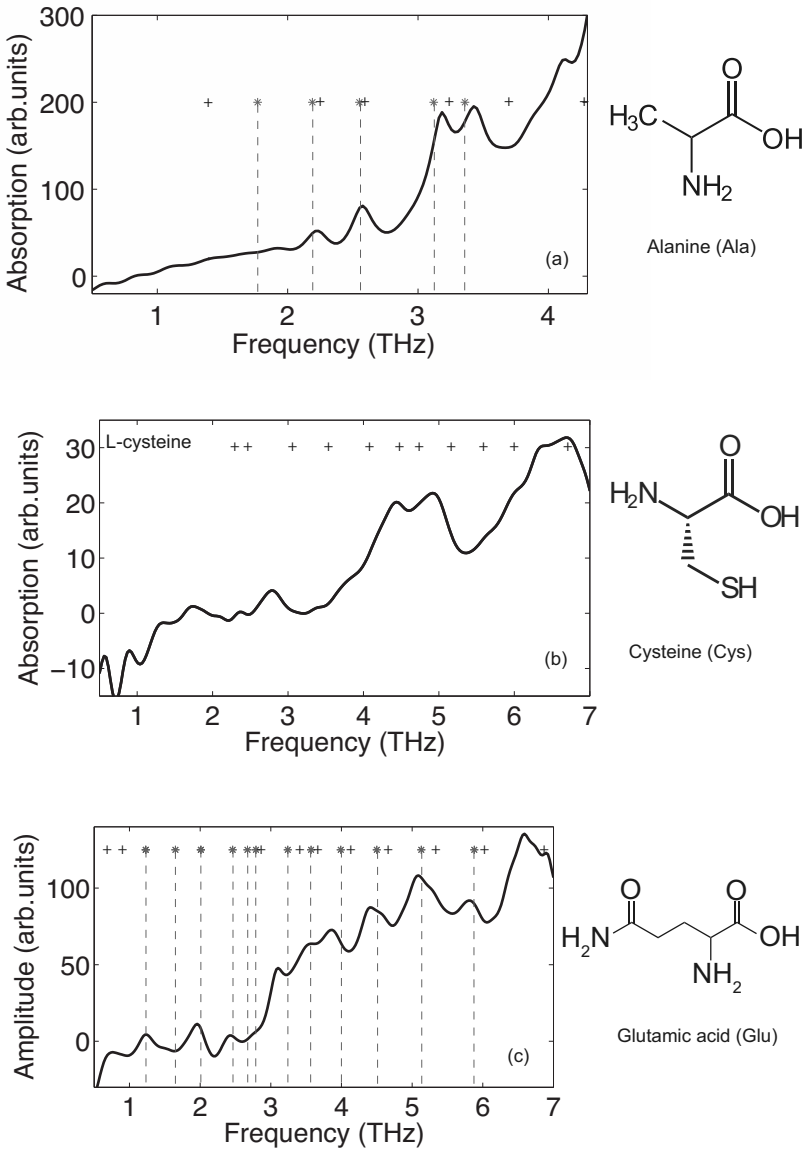

Figure 4.9: THz absorption spectra of (a) L-alanine, (b) L-cysteine, and (c) L-glutamic acid. The chemical structure of each amino acid is shown to the right of its THz absorption spectrum. The dotted line with '$*$' shows the band positions measured by Matei et al. at 298 K and '+' shows the band positions measured by Husain et al. at 100 K [121] . There was no measurement done on cysteine by Matei et al.

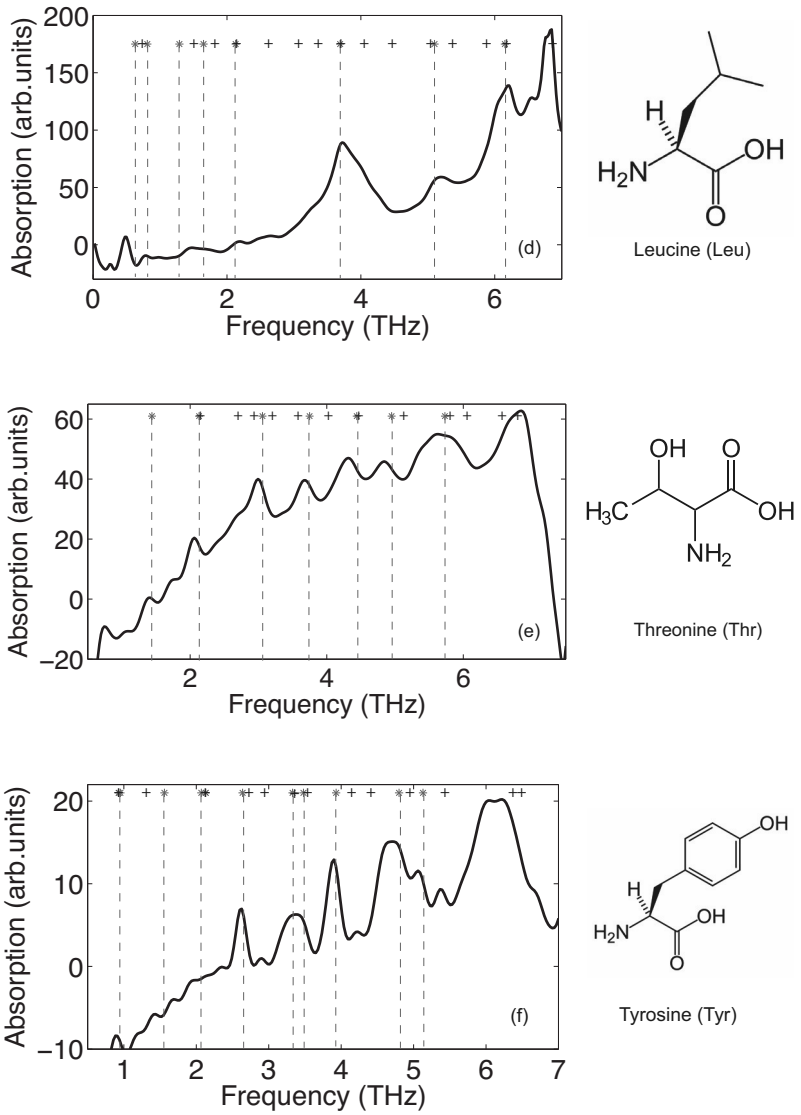

Figure 4.10: THz absorption spectra of (d) L-leucine, (e) L-threonine, and (f) L-tyrosine. The chemical structure of each amino acid is shown to the right of its THz absorption spectrum. The dotted line with '$*$' shows the band positions measured by Matei et al. at 298 K [127] and '+' shows the band positions measured by Husain et al. at 100 K [121].

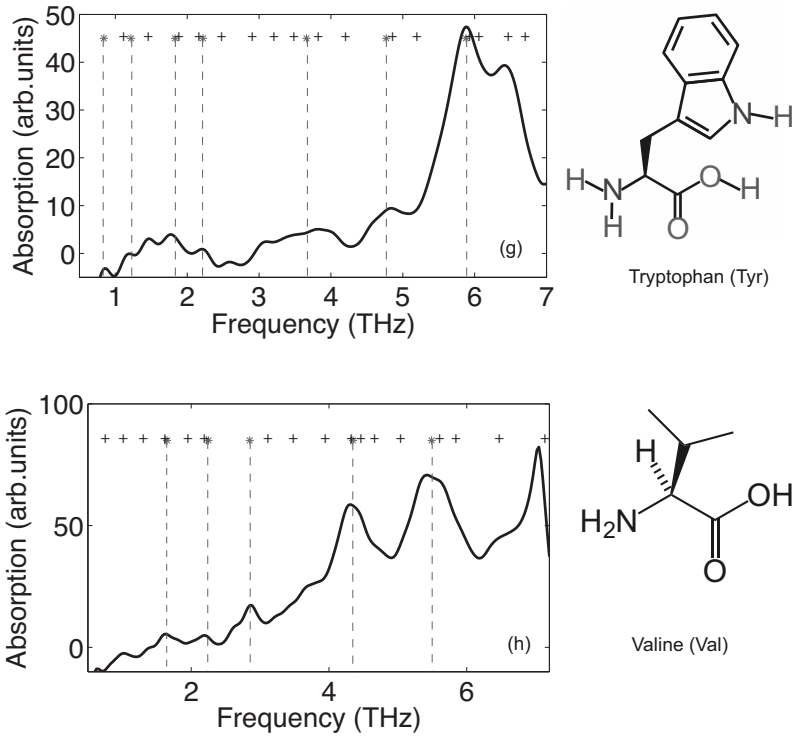

Figure 4.11: THz absorption spectra of (g) L-tryptophan, and (h) L-valine. The chemical structure of each amino acid is shown to the right of its THz absorption spectrum. The dotted line with '$*$' shows the band positions measured by Matei et al. at 298 K [127] and '+' shows the band positions measured by Husain et al. at 100 K [121].

absorption coefficient of the amino acid samples. In the Figs. 4.9-4.11, the dotted vertical lines indicate the positions of the absorption lines measured by Matei et al. at 298 K [127] using a FT spectrometer and the star markings indicate the positions of the absorption lines measured by Husain et al. at 100K [121]. The actual absorption coefficients cannot be compared. In our case, the sample is mixed with PE powder and the reference spectra are calculated from THz pulses transmitted through air in a quasi-near field THz-TDS. In the case of Matei et al. and Husain et al., the sample is mixed with PE powder and the reference spectra are calculated from the THz radiation transmitted through a PE pellet which contains the same amount of PE as in the sample pellet in a FT spectrometer. So, here we can only compare the absorption band positions.

In the case of L-alanine, when a sample pellet is made by mixing L-alanine with PE powder in the ratio of 10:100, then the absorption is too strong to yield measurable signals above 4.5 THz. This absorption spectrum did not show the two lines at 2.21 THz and 2.57 THz reported by Yamaguchi et al. [128]. The two lines at frequencies 2.21 THz and 2.57 THz were visible only in a pure L- alanine pellet. The lines at 3.7 THz and 3.43 THz show a slight shift with respect to the measurement done by Matei et al., indicated by the dotted lines. The reasons for these shifts are currently unknown. The low temperature measurement at 100 K, by Husain et al. shows bigger shifts with respect to our measurement which may be attributed to the change in temperature leading to real spectral shifts in their line positions. Comparing the absorption spectrum of the pure L-alanine pellet with a pellet made of mixing L-alanine with PE powder, did not show any indication of the influence of the presence of PE powder on the absorption spectrum of L-alanine.

The absorption spectrum of L-cysteine has been measured by Husain et al. and Korter et al. They measured at two different temperatures. Husain et al. measured at 100 K and 300 K, while Korter et al. measured at 77 K and 298 K. In the case of Husain et al. measurement was done by the FT spectrometer and Korter et al. measured low THz frequencies with a THz-TDS and higher frequencies (above 3 THz) with a FT spectrometer. It was found by Korter et al. that the absorption spectrum of L-cysteine does not show any shift as a function of temperature. A comparison of the absorption spectrum we measured at room temperature with the one measured by Husain et al. at 100 K, does show differences in the absorption band positions which cannot be explained by the frequency resolution of the system. This cannot be attributed to frequency shifts due to changes in

temperature. The Matei et al. did not measure the absorption spectrum of cysteine. Comparing the measurements done by Korter et al. and Husain et al. with our measurements, it can be seen that there are some differences between the three measurements, which cannot be attributed to temperature change. This inconsistency between the measurements shows the importance of measuring the THz absorption spectrum of L-cysteine with different techniques. The quasi-near field spectrometer provides an easy and reliable way to do this. These inconsistencies also give a clear indication that further studies are needed on this amino acid molecule.

Figs. 4.9-4.11 (c-h) show the measured THz absorption spectra of L-glutamic acid, L-leucine, L-threonine, L-tyrosine, L-tryptophan and L-valine samples. These THz absorption spectra also show good agreement with the measurement done by Matei et al. The cause of the slight differences between our measurements and measurements done by Matei et al. are currently unknown. The good agreement between our results and those done by Matei et al. again shows the applicability of the quasi-near field spectrometer. Apart from the high sensitivity and SNR of THz-TDS systems, the quasi-near field spectrometer has the additional advantage that it does not have to be flushed with dry nitrogen gas to remove water vapor because of its very short THz beam path.

4.3.4 Metal oxides

Recently, our research group found that by focussing laser pulses on an oxidized copper (Cu) plate significant amounts of THz radiation can be generated. It was also found that it is the interface between cuprous oxide (Cu_2O) and Cu which generates the THz radiation. The exact mechanism of THz radiation is still under investigation. Cu_2O is a direct-gap semiconductor with a band gap energy of 2.0 eV. To understand the generation mechanism and to understand how the generated THz radiation can be coupled to surface plasmons, it is important to know the THz absorption spectrum of Cu_2O. Also, the possibility of THz generation from other metal-metal oxide interfaces, such as silver (Ag)- silver oxide (Ag_2O) is investigated. Unlike Cu_2O, Ag_2O is a conductor in bulk form. Both Cu_2O and Ag_2O have cubic structure. Both are known to have a strong phonon mode in the frequency region of our interest, 0.5 - 7 THz. Cu_2O has its phonon resonance at 4.29 THz [129, 130] and Ag_2O has one at 2.55 THz [129]. We measured the THz absorption spectrum of these two metal oxides. Both samples were purchased from GoodFellow. Cu_2O is in the form of a reddish brown powder and Ag_2O is a powder with grayish color. Cu_2O pow-

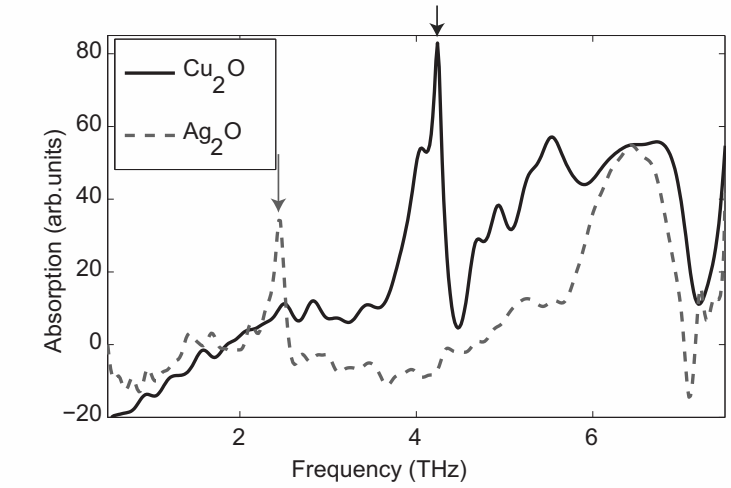

Figure 4.12: THz absorption spectrum of Ag_2O and Cu_2O. Ag_2O has a strong phonon resonance at 2.5 THz and Cu_2O has one strong phonon resonance at 4.3 THz. The arrows indicate the positions of the phonon resonances reported in literature [129, 130]

der is mixed with PE powder in the ratio of 30:100 and Ag_2O is mixed with PE powder in the ratio of 20:100. The mixture is pressed to pellets of thickness approximately 0.5 mm each. Figure 4.12 shows the THz absorption spectra of Ag_2O and Cu_2O at room temperature. There is an absorption peak at 4.3 THz in the Cu_2O spectrum and at 2.5 THz in the Ag_2O spectrum. Comparing to what has been reported in literature [129, 130] these two absorption lines at 4.3 THz and 2.5 THz respectively corresponds to phonon resonances in Cu_2O and Ag_2O. Incidentally, the perfect agreement between the measured phonon frequencies and the literature values for these phonon frequencies, indicates that, the shifts in the measured absorption band positions of amino acids compared to what have been reported in literature, is not because of any systematic error in the measurement. Apart from the strong phonon modes at 4.3 THz for Cu_2O and 2.5 THz for Ag_2O , there are other weaker absorption features due to other mechanisms which are still under investigation.

4.4 Detection of moisture content

THz radiation is strongly absorbed by water. The absorption coefficient of water at THz frequencies is as high as 150 cm^{-1} at 1 THz and increases to

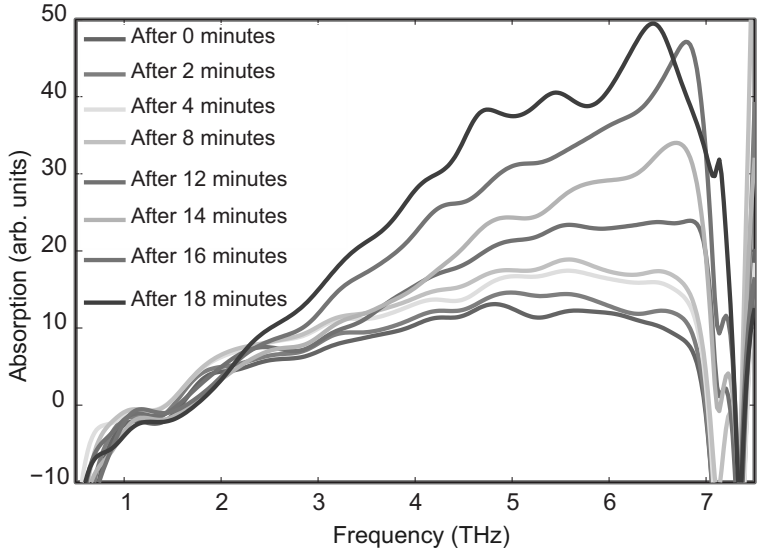

Figure 4.13: The time evolution of the absorption spectrum of a freeze dried coffee sample measured at eight time intervals after exposure to ambient air.

450 cm^{-1} at 3 THz. This strong absorption of THz radiation by water have many applications such as medical imaging, determination of water contents in leaves and in the determination of water content of materials in general [131, 132]. As the absorption of THz radiation by water increases with frequency in the THz frequency range, access to frequencies >3 THz makes it easier to measure the increase or decrease in the water content of a hygroscopic material. As an example, we show in Fig. 4.13 the absorption increase in the range from 0.5 - 7 THz of an initially freeze dried coffee sample, after being exposed to air. The freeze-dried coffee (IMA Edwards Freeze Drying Solutions) is highly hygroscopic and it transforms from a dry spongy substance to a sticky substance in less than 20 minutes if exposed to ambient air. Compared to the low frequency region, the frequency region between 3 - 7 THz gives a very clear indication of the increasing water content of the sample. In order to measure the water content quantitatively, the system should be calibrated with samples whose initial water content is known and stable, and the whole experiment should be conducted in an atmosphere with humidity control, which is beyond the scope of this demonstration experiment.

4.5 Conclusions

In this chapter, we have presented some examples of measurements of THz absorption spectra. Spectra are shown of both organic and inorganic substances. Some of the materials we used have known THz absorption spectra measured with techniques other than THz spectroscopy. This makes it possible to compare the results from the quasi-near field spectrometer to what is measured with other techniques. Our results show very good agreement with the earlier measurements of the absorption spectra of D-tartaric acid, lactose, sucrose, cuprous oxide, silver oxide, and amino acids. These agreements prove the applicability of the quasi-near field spectrometer in measuring the THz absorption spectrum of materials in the frequency range of 0.5 - 7 THz. Apart from the broad bandwidth, the spectrometer has the advantage that it need not be flushed with dry nitrogen gas to get rid of water vapor lines in the measurement. Such a spectrometer is very suitable for measuring samples with a thickness of about 1 mm. The quasi-near field spectrometer provides a quick and easy method to measure the terahertz absorption spectra of samples.

5 Freeze Drying

5.1 Introduction

This chapter describes an application of THz spectroscopy in the pharmaceutical industry. Here we show how terahertz time domain spectroscopy can be used to identify the polymorphs of mannitol, a frequently used excipient in the pharmaceutical industry. THz absorption spectra are then used to find out the dependence of the formation of mannitol polymorphs on different freeze drying methods.

Freeze drying, also known as lyophilization, is a dehydration process intended to preserve substances, that may be of biological origin. The freeze drying technique is very commonly used in the pharmaceutical, biotechnology, and food industry to increase the shelf life of perishable substances and to make them lighter for transportation. The presence of water may cause degradation because of chemical or biological influences. Many chemical processes such as certain oxidation processes require the presence of water for the reaction to occur. In freeze drying, water is removed by sublimation, that means, water goes directly from the solid phase to the gas phase without passing through the liquid phase. This makes it different from the dehydration of substances by heating, in which, water goes from the liquid to the gas phase by evaporation. There are mainly two problems with the evaporation/dehydration pro-

cess. First, it is difficult to remove all water by evaporation because most of the water is not directly exposed to air. Second, heating can cause unwanted changes in shape, texture and composition of the material. Many pharmaceutical ingredients will not survive the boiling process. The basic idea behind freeze drying is to ”freeze” the physical properties like composition, shape, texture etc, of the substance. Freeze dried substances can be stored at room temperature in sealed containers. Freeze drying offers a way to improve the stability and shelf life of many pharmaceutical compounds. Many parenteral medications such as vaccines, proteins, peptides, and antibiotics are usually freeze dried.

This chapter is organized as follows: first we will discuss the basics of freeze drying and its importance in the pharmaceutical industry. Then, the sample preparation methods will be detailed. The THz absorption spectra of individual polymorphs and that of freeze dried samples will be followed by a comparison with the Röntgen diffraction (XRD) measurements of these samples.

5.2 Freeze drying

There are several steps involved in the freeze drying process. The substance is cooled until crystallization of water and subsequently the excipients take place. The amorphous components solidify in a glassy state. Next the pressure is reduced to below the triple point of water. Next, just enough heat is provided so that the crystalline water sublimates without melting. Materials whose properties cannot be adequately preserved by freezing are not suitable for freeze drying [133]. Figure 5.1 shows the phase diagram for H_2O. The boundary between the gas and the liquid runs from the triple point to the critical point. This diagram is not to scale; a scaled version looks like the one in the inset. In the diagram, primary drying phase of freeze drying is represented by the black arrow, which takes the system around the triple point, avoiding the direct liquid-gas transition seen in ordinary drying process (dotted arrow). The reconstitution of freeze dried products is done by adding the original solvent and the intended original (bio)chemical activity is then restored. The freeze drying process is divided into three stages; freezing, primary drying and secondary drying which are described below [134].

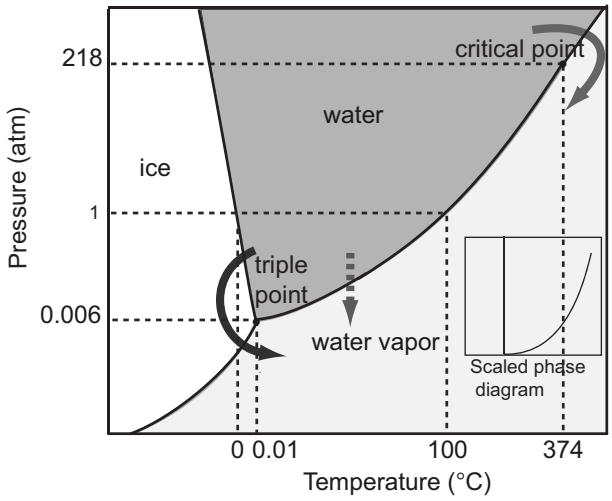

Figure 5.1: Phase diagram for H_2O. The boundary between gas and liquid phases runs from the triple point to the critical point. This diagram is not to scale; a scaled version looks like the one in the inset. Freeze drying (black arrow) brings the system around the triple point, avoiding the direct liquid-gas transition seen in ordinary drying (dotted arrow).

5.2.1 Freezing

The first step in freeze drying is immobilization of the substance by freezing. Usually, the freezing temperatures are between 243 K and 193 K. The freezing phase is critical in the whole freeze drying process, because the product can be spoiled if badly executed. Crystalline and polycrystalline materials should be frozen and kept below their eutectic point[1] during the phase of primary drying to prevent melt-back or collapse during primary drying. Amorphous (glassy) materials do not have a eutectic point, but do have a critical point, and the product should be maintained below this point. Freeze drying is a slow process. In common freeze dryers, the vials

[1]A eutectic mixture is a mixture of two or more solids, at such proportions that the melting point of the mixture is a local temperature minimum. This means that all the constituents crystallize simultaneously at this temperature from the molten liquid solution. The temperature at which this takes place is the eutectic temperature, and the composition and temperature at which it takes place is called the eutectic point.

containing the product are supported by shelves. These shelves are hollow and a heat transfer fluid is circulated through them. By cooling this fluid and thus subsequently the vials containing the product, the freezing step is effectuated. This process generally is not very fast as the shelf cools at a rate of 1 K per minute. The purpose of this slow cooling is to generate large ice crystals. Large ice crystals correspond to large pore sizes of the dried cake and therefore limit the flow resistance for the subliming vapor during the primary drying step. There might be reasons for rapid freezing related to product stability in the liquid form, but this would compromise the sublimation process speed during primary drying.

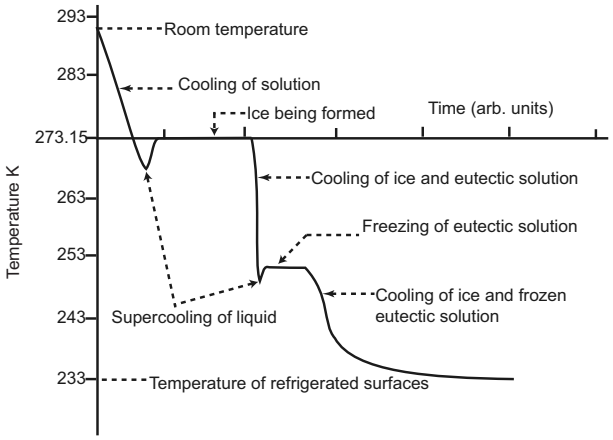

Figure 5.2: The freezing cycle of dilute solution of common salt in water [133]

Figure. 5.2 shows the freezing cycle of a dilute solution of common salt (NaCl) in water. There are two freezing points, one for pure water, and the other for the eutectic solution of salt in water at 251.6 K. The liquids supercool below their freezing point before freezing.

5.2.2 Primary drying

The second step in freeze drying is to pull vacuum to a level of typically 100 mTorr (13.3 Pa). This vacuum step is only allowed when the product is already frozen, to prevent boiling. When vacuum is applied, sublimation can occur because the system is below the triple point of water. This sublimation is driven by the difference in water vapor pressure between the frozen product and a condenser, which is kept at a lower temperature.

Energy needs to be supplied to the product during sublimation to compensate for the latent heat of evaporation, to overcome the flow resistance of vapor through the already dried product and to maintain the vapor pressure difference with the condenser. The lower the energy loss through the dried product, the faster the freeze drying process can take place, given the maximum allowable temperature of the product. This maximum allowable temperature is given by the melting point or the glass transition point[2]. In this initial drying phase, about 95 % of the water in the material is sublimed. This phase may take a long time (can be several days in the industry) because the limited allowable temperature limits the energy supply. The bound water or residual moisture is removed by secondary drying.

5.2.3 Secondary drying

Secondary drying is necessary to desorb the remaining moisture in the dried product while the ice was removed in the primary drying phase. In this phase, the temperature is higher and can even be above 273 K, to break any physio-chemical interactions that have taken place between the water molecules and the frozen material, and the pressure is lower than that in the primary drying phase. After the primary drying the residual moisture may be as high as 10% . In secondary drying this is reduced to an optimum value for stability, usually, between 0.5% and 2.7% [133]. After the freeze drying process is complete, the vacuum is usually broken with an inert gas, such as nitrogen, before the container is sealed. Often, the sealing takes place at pressure below the atmospheric pressure.

5.3 Freeze drying in the pharmaceutical industry

Freeze drying is very commonly used in the pharmaceutical industry to increase the shelf life and dry state stabilization of therapeutic agents. The freeze dried material is stored in a container free of oxygen and water

[2]The glass transition temperature (T_g) of a non-crystalline material is the critical temperature at which the material changes its behavior from being 'glassy' to being 'rubbery'. 'Glassy' in this context means hard and brittle (and therefore relatively easy to break), while 'rubbery' means elastic and flexible. Note that the concept of T_g only applies to non-crystalline solids, which are mostly either glasses or rubbers. A glass is defined as a material that has no long-range atomic or molecular order and is below the temperature at which a rearrangement of its atoms or molecules can occur. On the other hand, a rubber is a non-crystalline solid whose atoms or molecules can undergo rearrangement.

and it is reconstituted with water when required. Apart from the parenteral medications, solid oral forms such as tablets and capsules are also freeze dried due the wide acceptability and convenience. Although the technique of freeze drying has already been used in the industries for a long time, its popularity is now increasing due to the increasing use of relatively unstable biopharmaceuticals.

5.4 Polymorphism in freeze dried pharmaceutical products

Polymorphism is the occurrence of multiple possible states of a single entity. In the case of chemical compounds, this refers to the multiple possible crystal structures of the same chemical compound. Polymorphism is well known in the pharmaceutical industry and in freeze dried pharmaceutical products. These polymorphs often can have unique physio-chemical characteristics which can influence their stability, solubility and other performance characteristics [135–139]. For example, paracetamol powder has poor compression properties and it poses a difficulty in making tablets, so a new polymorph of paracetamol was developed which is more compressible. Solubility is very important for ease of reconstitution as some polymorphic forms are more soluble than others. Because of all these reasons, many drugs receive regulatory approval only for a single polymorph. The thermodynamically stable state may not be the one with the desired properties like solubility, so these compounds need to be stabilized against chemical as well as physical degradation, by freeze drying. All this makes it important for the pharmaceutical industry to know which polymorph is formed during the freeze drying process. A phase transformation may occur during any stage of the drug manufacturing process and this is certainly possible in the various stages of the freeze drying process. Ritonavir is a well known example of extreme consequences originating from a sudden appearance of a new polymorph. It was originally formulated as a semi-solid in a soft gelatin capsule using form I , which was the only crystal form identified during crystal development. Suddenly, after 240 lots of capsules had been successfully produced and no stability problems noticed, the capsules started to fail in dissolution tests because of the appearance of a new polymorph, form II, with lower bioavailability[3] [136, 141]. This started a long and expensive process during which

[3]Bioavailability is a measurement of the rate and extent of a therapeutically active drug that reaches the systemic circulation and is available at the site of action [140]

the drug product was reformulated to suit form II, and the preparation of form I was revisited [142]. This example highlights the importance of knowing the possible polymorphs of a compound and their physical properties. Once these are known, there should be some method to monitor the manufacturing and processing of the compound to make sure the desired polymorphs are produced. In the context of freeze drying, the processing stages may have to be optimized for optimum process speed, but at the same time not leading to the unintended formation of undesirable polymorphs.

5.5 Spectroscopic techniques for identification of polymorphs

There exist numerous techniques to characterize the polymorphs, such as powder X-ray diffraction [143, 144], nuclear magnetic resonance [138, 145, 146], Raman spectroscopy, vibrational spectroscopy [147–151] and thermal analysis [152]. X-ray powder diffraction is commonly used, but it is a time consuming process and requires sample preparation. This means that it cannot easily be used as an in-line monitoring tool [153]. Apart from this, X-rays fall into the category of potentially harmful ionizing radiation [154]. Near -infrared (NIR) analysis has been widely used as a tool for studying solid phase transformations [155]. NIR spectra of solid forms consist of overtones and combinations of fundamental vibrations, thus making the spectroscopic analysis more complex in terms of assignments of bands. For the analysis of dehydration and hydrate formation, NIR spectroscopy is a very valuable tool as it can identify the state of water molecules present in the solid sample [156]. In Raman spectroscopy, the sample needs to be excited by shining a laser beam directly onto it. However, Raman spectroscopy is a nonlinear process and requires high light intensities, which can cause phase changes, unwanted photochemical reactions, or even physical damage to the sample. Moreover, fluorescence from the sample can overwhelm Raman signal which is intrinsically weak [157, 158]. However use of the combination of Raman and NIR spectroscopy for in-line and real time monitoring of freeze drying process was demonstrated by two research groups [159, 160].

Recently, it was reported how THz-TDS could be used to identify the different polymorphs of ranitidine hydrochloride [27]. This is possible because many organic molecules in the crystalline or polycrystalline form show distinct absorption spectra in the THz frequency region [109, 161–

166]. The absorption lines in the spectra correspond to lattice vibrations or local molecular vibrations of the crystal, and are different for different polymorphs [114, 167].

5.6 Mannitol

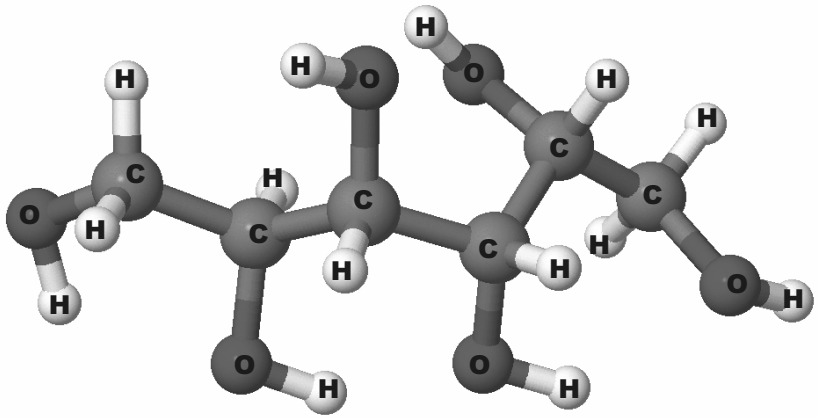

Figure 5.3: Molecular structure of mannitol constructed using Jmol: an open-source Java viewer for chemical structures in 3D. http://www.jmol.org/

Mannitol is an acyclic sugar alcohol with chemical formula [$C_6H_{14}O_6$]. Figure 5.3 shows the molecular structure of mannitol. Mannitol is a frequently used bulking agent to facilitate the production of a mechanically stable dry pellet or cake with a very small amount of active product. It has low hygroscopicity and chemical reactivity. It has a strong tendency to crystallize from frozen aqueous solutions and has a high melting point (260 K) for mannitol ice eutectic mixture [168–170]. So, during freezing, ice crystals and mannitol crystals form concurrently, thus making it a very good candidate to make a pharmaceutically elegant and physically stable freeze dried solid. Its porous crystalline structure allows rapid reconstitution. There exist three polymorphic forms for mannitol; namely α, β and δ [171]. During freeze drying mannitol can crystallize as anhydrous

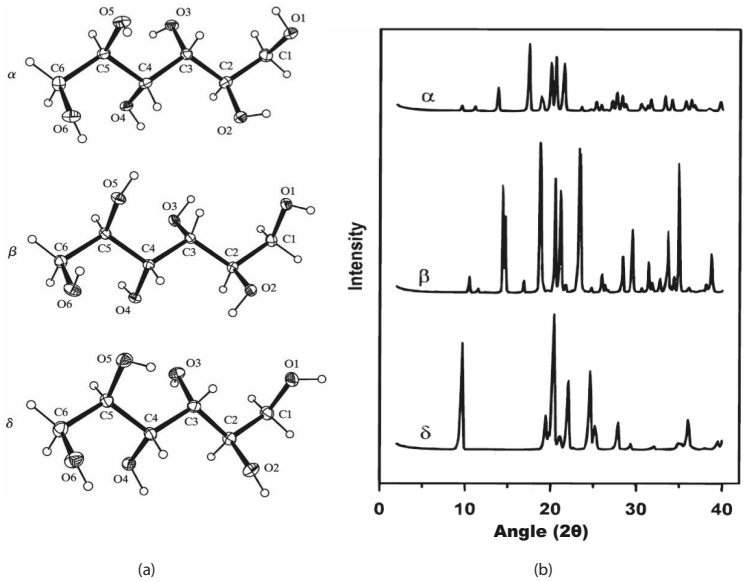

Figure 5.4: (a) Polymorphs of mannitol [172] (b) X-ray diffraction spectra of each of these polymorphs [135]

α, β, δ forms or as mannitol hemi-hydrate[4]. Depending on the concentration and on the specific steps taken during the freeze drying process, often different polymorphs may be present simultaneously [135, 172–174]. The polymorphic form of mannitol in freeze dried formulations has been shown to depend on process and formulation variables [135], thus making it a model compound for studying the effect of freeze drying on molecular structure.

Mannitol is a versatile excipient whose physical state can be engineered to meet the diverse requirements of formulation development. When used as a bulking agent, mannitol is frequently induced to crystallize [175, 176]. When used as a lyoprotactant for the active pharmaceutical ingredient, mannitol must be retained amorphous [177, 178]. Lyoprotectants are molecules used to protect freeze dried material. For example, during the freeze drying process, protein molecules encounter freezing and drying stresses, which can result in their denaturation [179, 180]. Hence, during the design of a freeze dried formulation, several process and formulation factors

[4] A hydrate in which the molecular ratio of water molecules to anhydrous compound is 1:2.

have to be optimized to ensure that the active ingredient does not undergo irreversible physical and chemical changes and also to assure long-term stability during storage [181]. Of the different additives that are used in a freeze dried formulation, lyoprotectants play an active role in protecting proteins from denaturation [181]. It has been postulated that lyoprotectants form hydrogen bonds with proteins, acting as replacement for the hydration shell, and hence maintain the native conformation of the protein. Lyoprotectants have been found to be maximally efficient when they are present in the amorphous state [182]. It is difficult to maintain mannitol in the amorphous state during the freeze drying process, making it a poor choice as a lyoprotectant. This means, whether used as bulking agent or as a lyoprotectant, it is important to know the physical state of mannitol in the freeze dried material.

5.7 Sample preparation

The mannitol test samples we investigate are freeze dried in different ways with the aim to develop new and more efficient freeze drying techniques. A typical freeze drying cycle consists of freezing the product, pulling vacuum until a pressure of typically 100 mTorr (13.2 Pa) is reached, primary drying by sublimation and secondary drying by further heating under vacuum. The heat flow takes place through the bottom of the vials which are in contact with hollow stainless steel shelves. All the freeze dried samples we investigated have gone through the same freeze drying cycle except for the initial freezing stage. The first sample was freeze dried in the manner described above, starting from a 2 ml mannitol solution in a 5 ml vial and going through the typical freeze drying cycle, resulting in a vial filled with the freeze dried mannitol to a height of about 10 mm. During the sublimation process, the crystalline water is removed from the sample, resulting in a highly porous cake-like texture. The second type of sample is prepared by dropping large droplets of mannitol solution (5% w/w) out of a syringe into a small container with liquid nitrogen. The droplets freeze very rapidly and are subsequently inserted into vials which are placed upon pre-cooled shelves (228 K). The remaining sublimation process is similar to the standard sublimation process described before. The third type of sample is prepared by spraying very small droplets of mannitol solution (5% w/w) into a small container with liquid nitrogen. The fine droplets again freeze rapidly. The frozen fine spheres are then collected and inserted into vials. The vials are placed on pre-cooled shelves (228 K).

The remaining sublimation process is again similar to the standard process.

Slow freezing, as in traditional freeze drying, and fast freezing with liquid nitrogen, are expected to give rise to different end results. This is because rapid freezing coincides with the formation of small ice crystals and a potentially different crystallization of mannitol. The drying process in freeze drying can be accelerated by increasing the sublimation area and thus the sublimation rate. One way to increase the effective sublimation surface is to start with frozen spheres. In the case of large frozen droplets, the drying process time was similar to that in the standard process, because, although the sublimation area was increased, the physical contact and thus the heat transfer between the spheres was limited. In the case of fine frozen droplets, the sublimation process was finished earlier than in the large frozen droplet situation because of the better contact between the spheres.

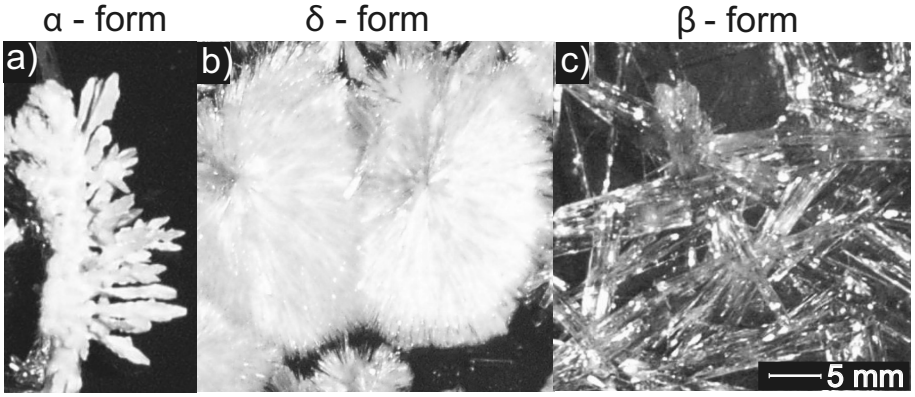

Figure 5.5: Photographs of the three types of mannitol crystals corresponding to the α, δ and β polymorphs. (a) The α form is opaque and resembles vertically growing lichen-like structures. (b) The δ form is translucent and resembles a needle-like structure in spherulite morphology. (c) The β form consists of translucent parallelepiped structures.

Individual polymorphs of mannitol are prepared in the lab from mannitol powder purchased from Sigma Aldrich, which consists predominantly of the β polymorph. All three known polymorphs of mannitol were prepared by the Walter-Levi method [183]. Solutions of 0.4, 0.8 and 1.2 Molar (M) are prepared and 10 ml of each solution is placed in a watch glass and allowed to evaporate at room temperature. The evaporation results in

three distinct crystal forms. The first form is mainly observed at the edge of the watch glass. It is opaque and looks like lichen and grows vertically. This kind of morphology is known to be typical for the α polymorph. The second crystalline form was created in 0.4 and 0.8 M solutions. It has a translucent needle-like structure in spherulite morphology and this is typical for δ form. The third form was obtained from the 1.2 M solutions and consists of translucent parallelepipeds, and this is known to be the β polymorph. Figures 5.5 (a), (b) and (c) show the morphology of the three distinct crystal forms of the α, δ and β form, respectively.

5.8 X-ray diffraction measurements

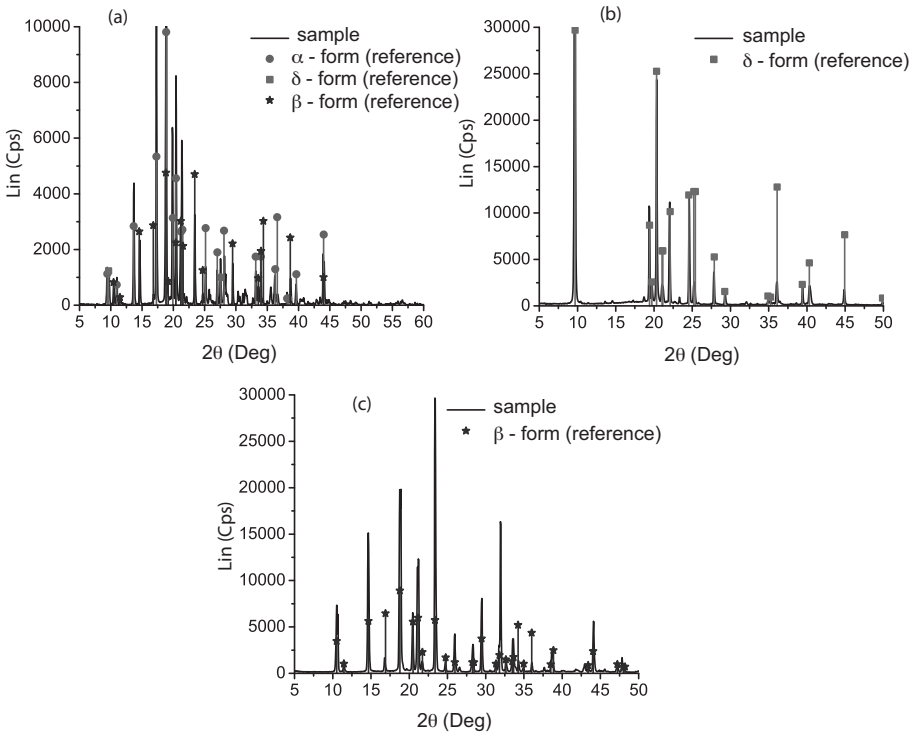

Figure 5.6: X-ray diffraction data of (a) sample shown in Fig. 5.5 (a). (b) sample shown in Fig. 5.5 (b). (c) sample shown in Fig. 5.5 (c).

X-ray scattering technique is an analytical technique which can reveal information about the crystallographic structure, chemical composition,

and physical properties of materials. This technique is based on observing the scattered intensity of an X-ray beam hitting a sample as a function of incident and scattered angle, polarization, and wavelength or energy. X-ray powder diffraction (XRD) is a technique used to characterize the crystallographic structure, crystallite size (grain size), and preferred orientation in polycrystalline or powdered solid samples. Powder diffraction is commonly used to identify unknown substances, by comparing diffraction data against a database maintained by the International Centre for Diffraction Data (ICDD).

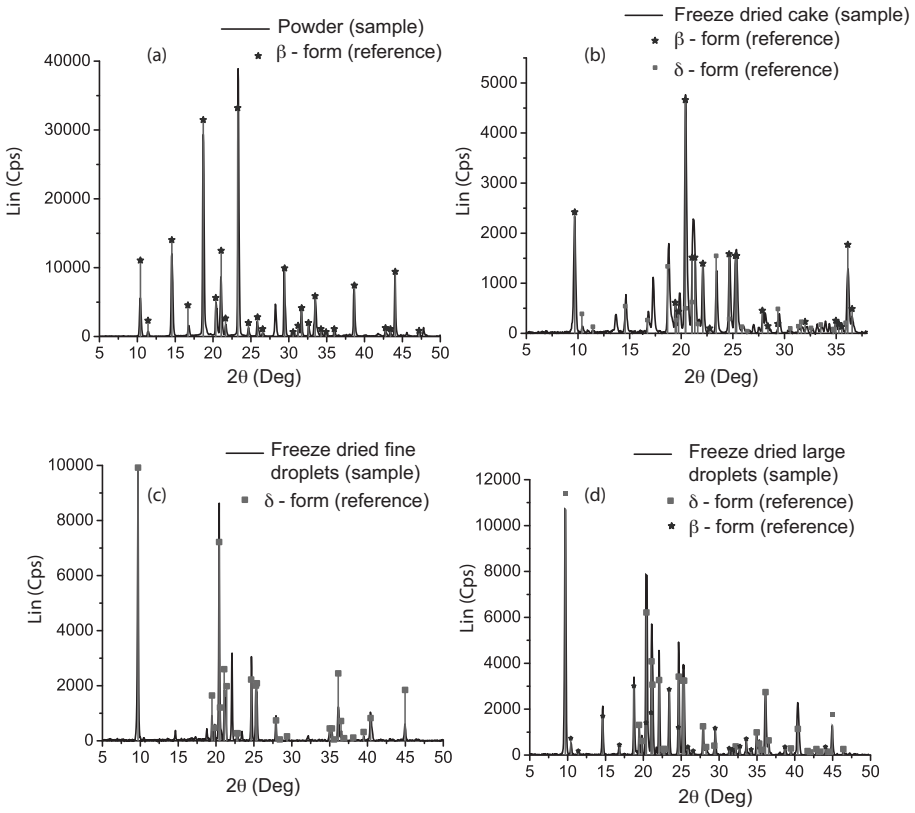

Figure 5.7: X-ray diffraction data of (a) mannitol powder (b) traditionally freeze dried mannitol in the form of a cake (c) mannitol freeze dried as fine droplets and (d) mannitol freeze dried as large droplets.

Before measuring the terahertz absorption spectrum of the freeze dried samples, it is important to know the polymorphic state of the samples. We therefore measured the X-ray diffraction pattern of each of these samples.

X-ray diffraction patterns of the samples are compared with the data from the ICDD to identify the constituents. Figures 5.6 (a), (b) and (c) show the XRD of the samples shown in Fig. 5.5 (a), (b) and (c) respectively [1]. The markers in these figures indicate the known peak positions of each polymorph, taken from the ICDD. The comparison with the data from ICDD shows that, the sample shown in Fig. 5.5 (a) is a mixture of α and β polymorphs. We were unable to make pure α polymorph in the lab. The sample shown in Fig. 5.5 (b) is identified to be pure β form and the sample in Fig. 5.5 (c) is identified to be δ form. Figures 5.7 (a), (b), (c), and (d) show the measured X-ray diffraction pattern of mannitol powder, freeze dried cake, freeze dried fine droplets and freeze dried large droplets respectively. Again, the markers in these figures indicate the known peak positions of each polymorph, taken from the ICDD database. By comparing the X-ray diffraction pattern of the samples with the data from ICDD, the original mannitol powder was shown to consist of the β polymorph. Mannitol freeze dried as fine droplets consists of the δ polymorph whereas mannitol freeze dried as large droplets contains mostly the β polymorph with traces of the δ polymorph. The traditionally freeze dried mannitol cake contains a mixture of both δ and β polymorphs. X-ray diffraction analysis shows that the end product of different freeze drying techniques results in different polymorphs, and is different from the polymorphic state of the initial mannitol powder.

5.9 Terahertz measurements

The quasi-near field spectrometer described in Chapter 3 is used for the spectroscopic measurement of the samples. The samples are first ground using a mortar and pestle, to reduce the particle size, so that light scattering is reduced to a minimum in the frequency range of interest. Then, polyethylene powder of particle size ≤ 30 μm (Mipelon XM-220, Mitsui Chemicals America, Inc) is mixed with the ground sample such that the sample forms 20 % of the total mass of the mixture. This is done to dilute the sample so that the peak absorption is not too strong and is within the measurement dynamic range of our system. The mixture is pressed into a pellet with a hydraulic press (Specac Ltd, UK) to a thickness of ≈ 0.6 mm.

In order to calculate the absorption spectrum of the sample pellet, we measure the THz electric fields with and without the sample pellet

[1] R. W. A. Hendrikx at the Department of Materials Science and Engineering of the Delft University of Technology is acknowledged for the X-ray analysis

in between the generation and detection crystals. The influence of pure polyethylene powder on the absorption spectrum is evident as a back ground absorption which increases with frequency. Figure 4.3 in chapter 4 shows the absorption spectrum of a pure polyethylene pellet.

5.10 Results and discussions

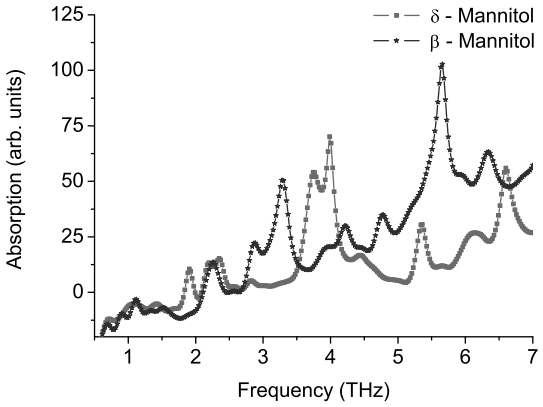

Figure 5.8: THz absorption spectra of the β and δ forms of mannitol. The spectra are very different from each other, especially in the frequency region from 2.5 - 6 THz.

Figure 5.8 shows the measured terahertz absorption spectra of the β and δ forms of mannitol. The β form shows absorptions peaks at 1.12, 2.26, 2.88, 3.28, 4.22, 4.77 and 5.66 THz. Of these, the absorption peaks at 2.88, 3.28 and 5.66 THz are the strongest. The overall appearance of the absorption spectrum of the β form is comparable to an earlier published absorption spectrum of D-mannitol measured by terahertz attenuated total reflection (ATR) spectroscopy from 0.3 - 3.6 THz [184]. Although not explicitly mentioned in that paper, this resemblance suggests, that their sample was made of β mannitol. The peak positions, however, are slightly different. The reason for this is not exactly known, but may be related to the wavenumber-dependent penetration depth into the sample and the resulting comparatively more difficult data analysis in the case of the ATR technique. The δ form spectrum in Fig. 5.8 shows absorption peaks at 1.9 THz, two peaks at 2.19, and 2.3 THz nearly merged together and three

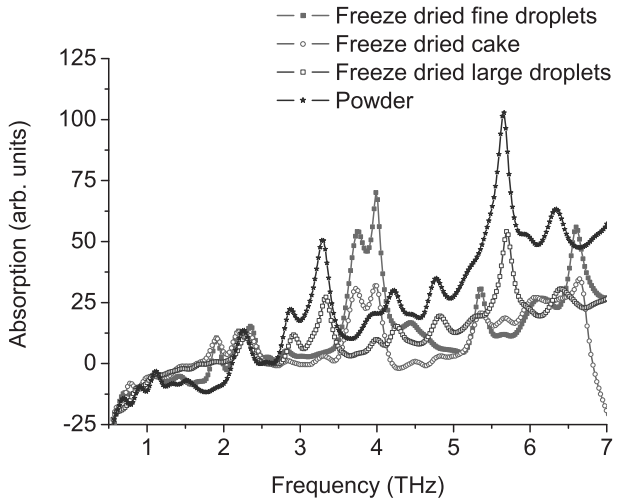

Figure 5.9: THz absorption spectra of freeze dried mannitol samples.

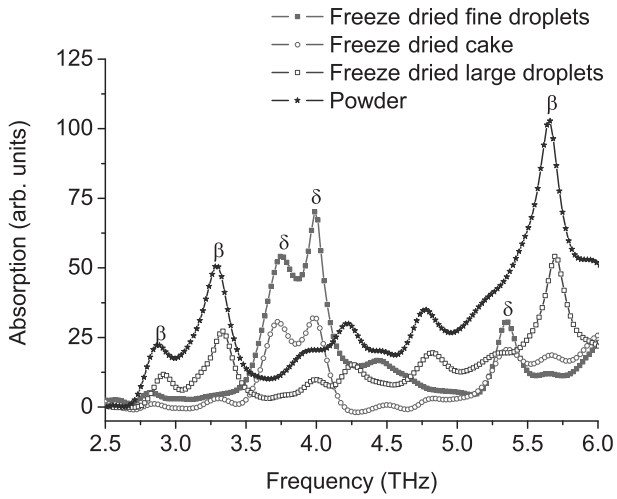

Figure 5.10: THz absorption spectra of freeze dried mannitol samples in the range from 2.5 - 6 THz. The main features are identified as δ and β by comparing with the absorption spectra of individual β and δ form of mannitol shown in Fig. 5.8

stronger peaks at 3.74, 3.98 and 5.36 THz. There is also a small peak at 4.4 THz. From these results, it is clear that for the purpose of identifying and distinguishing the β and δ polymorphs, the absorption peaks at 2.88, 3.28 and 5.66 THz for the β polymorph, and the peaks at 3.74, 3.98 and 5.36 THz of the δ polymorph are ideally suited.

We now proceed with the results for the freeze dried samples. The THz absorption spectra of mannitol samples freeze dried using three different methods as discussed above, along with that of mannitol powder, are shown in Fig. 5.9 and a slightly zoomed-in version is shown in Fig. 5.10. The region with distinct features is from 2.5 - 6 THz and is shown in Fig. 5.10. Using the results of Fig. 5.8, in which the absorption spectra of the pure β and δ polymorphs are shown, we are now in a position to identify the polymorphs in the freeze dried samples. In the 2.5 - 6 THz region, the freeze dried cake has two small peaks at 2.88 THz and 3.28 THz, and large peaks at 3.74, 3.98 and 5.36 THz. The two small peaks correspond to the β form and the large peaks to the δ form. Looking at the relative intensity of these peaks it can be concluded that the freeze dried cake contains mostly the δ form with some traces of the β form. This result is in agreement with the results from X-ray diffraction measurements shown in Fig. 5.7.

Similarly, the sample made of frozen fine droplets has three large peaks at 3.74, 3.98 and 5.36 THz corresponding to that of the δ form, whereas no β form peaks at 2.88, 3.28 and 5.66 THz are observed. Rapidly freezing fine mannitol droplets, followed by regular freeze drying therefore, predominantly gives rise to the formation of the δ polymorph with no indication of the presence of the β form. Remarkably, in the case of large droplets, we observe peaks at positions corresponding to both the β and the δ form. By comparing the relative amplitudes of these peaks, we can conclude that the sample consists mainly of the β polymorph with some traces of the δ form. Again, these results are confirmed by X-ray diffraction measurements. Results of these measurements are summarized in Table 5.1.

Different freeze drying methods resulted in different polymorphs or a mixture of polymorphs. As mentioned before, mannitol can crystallize in different polymorphic forms depending on the concentration of mannitol solution and the freezing rate. In our case, both the samples consisting of fine droplets and large droplets were frozen very fast with liquid nitrogen, but this resulted in different polymorphs of the end product. Since all three samples are going through the same sublimation process, this suggests that the polymorphs are formed during the freezing stage. The

samples	X-ray diffraction	THz absorption spectra
Powder	purely β form	purely β form
freeze dried cake	δ with traces of β	δ with traces of β
freeze dried fine droplets	purely δ form	purely δ form
freeze dried large droplets	β with traces of δ form	β with traces of δ form

Table 5.1: Identification of polymorphs by studying THz absorption spectra and X-ray diffraction patterns.

fine droplets are generated using a plant-spray nozzle. The mist of small droplets is directed into the liquid nitrogen container. During the flight of the droplets, some evaporation of water can take place, resulting in a higher concentration of mannitol in each droplet. Also, since the droplets are small, they have a high specific surface area and thus freeze faster than the large droplets thus favoring the formation of the δ polymorph [135]. The large droplets are created using a syringe. The liquid drops fall into the liquid nitrogen and, immediately, a crust of ice forms. The insulating properties of ice will lead to a slowdown of the freezing of the core of the material. Therefore, a mixture of 'crust'-form and 'core'-form will be generated resulting in a mixture of polymorphs.

The relative intensities of these peaks in principle be used to determine the weight percentage of each of these polymorphs in the mixture [148, 185].

Our results clearly show that depending on the freezing method used, different mannitol polymorphs can easily be formed. This strongly suggests that an in-line monitoring tool may be required during freezing of pharmaceutical products to study the formation and presence of polymorphs. The ability to check the presence of required polymorphs using THz radiation is clearly an advantage compared to the use of X-rays which have a photon energy large enough to pose a health hazard and to induce molecular changes.

5.11 Conclusions

We have measured the THz absorption spectra of the β and δ polymorphs of mannitol from 0.5 THz to 7 THz. The two polymorphs have distinct THz absorption spectra, especially between 2.5 and 6 THz. We have shown

that, for mannitol, changes in the way the material is frozen can result in the formation of different polymorphs or a mixture of polymorphs. Because THz-TDS can be used to identify the polymorphs of mannitol, we have subsequently used this technique to study the effect of various freeze drying techniques on the formation of these polymorphs. Our results are confirmed by X-ray analysis. THz-TDS has the added advantage that it may be easily employed as an in-line and, almost, real time monitoring tool, unlike X-ray diffraction analysis. Apart from the ability to identify the polymorphs, the relative intensities of the peaks in the THz absorption spectra of these samples can potentially be used to determine the weight percentage of each of these polymorphs in the mixture.

6
Conclusions and outlook

In the preceding chapters we have discussed the generation of THz radiation using a PCA, a quasi-near field THz spectrometer and some of their applications. THz generation using SI-GaAs PCA and detection using electro-optic method gives a very good SNR in a measurement time of 10 ms. For a semi-large aperture PCA, increasing the pump fluence on the emitter results in the saturation and even decrease in the emitted THz amplitude. The advantage of having an oscillator with a high peak power is ensured by keeping the pump spot size on the emitter relatively large. The saturation in the PCA under high pump fluences is explained using a phenomenological model. Space charge screening and radiation field screening of the applied bias field are the two major reasons behind the saturation effects. Using a 50 fs pulse and a SI-GaAs PCA, the generation bandwidth was limited to about 2.5 THz, so, to generate more broadband pulses, we focussed our attention on the generation of THz radiation using optical rectification.

Generation and detection of THz radiation using (110) oriented GaP crystals allowed us to generate frequencies up to 6 THz, after dry-nitrogen gas flushing to avoid absorption of THz radiation by water vapor and after difficult alignment of the parabolic mirrors. Keeping the generation and detection crystals less than a millimeter apart gave a significant improvement in the quality of the THz signal, both in terms of amplitude and bandwidth and eliminated the need for dry-nitrogen gas flushing.

This quasi-near field THz generation and detection setup simplifies the conventional THz generation and detection setup. The bandwidth of the generated THz radiation was 7.5 THz. The pulse width of the laser was the major factor limiting the bandwidth. The observed spectra of the generated THz pulses are explained with a simple model which takes into account the effects of phase-matching and absorption of THz radiation in the generation and detection crystals. We have also shown that the effect of counter propagation of THz pulse and probe pulse in the detection crystal is negligible above 0.5 THz.

Usage of modulation techniques and lock-in detection should further improve the the SNR of the system. However, pump modulation techniques may create their own problems such as mechanical vibrations or pulse lengthening. If these problems can be minimized, then modulating the pump beam with consecutive lock-in detection, may lead to further improvements of the signal-to-noise ratio. To prove the applicability of such a quasi-near field spectrometer, we measured the absorption spectra of certain materials. Some of the materials we used have known THz absorption spectra which were measured with techniques other than THz-TDS. This enabled us to compare the absorption spectra measured with the quasi-near field spectrometer to what is measured with these techniques. Our results show very good agreement with the earlier measurements of the absorption spectra of D-tartaric acid, lactose, sucrose, cuprous oxide, silver oxide, and amino acids. This agreement proves the applicability of the quasi-near field spectrometer in measuring the THz absorption spectrum of materials in the frequency range of 0.5 - 7 THz.

We have also shown that such a compact and easy to use THz spectrometer can be used to identify polymorphs in freeze dried mannitol. We have shown that, for mannitol, changes in the way the material is frozen can result in the formation of different polymorphs or a mixture of polymorphs. Our results are confirmed by X-ray analysis. THz-TDS has the added advantage that it may be easily employed as an in-line and, almost, real time monitoring tool unlike X-ray diffraction analysis, even though it's clear that further technical developments are needed to turn this into a practical instrument. Apart from the ability to identify the polymorphs, the relative intensities of the peaks in the THz absorption spectra of these samples can potentially be used to determine the weight percentage of each of these polymorphs in the mixture.

The ability of THz-TDS to be used as an in-line monitoring tool makes it attractive to study the freezing behavior of mannitol or other materials

in general. The measurement of absorption spectra of a (pharmaceutical) compound as a function of temperature makes it possible to find the temperatures at which the phase/polymorphic transitions occur, *if* they are any. The quasi-near field spectrometer does not require nitrogen flushing. Therefore a high throughput of consecutive samples can be expected. The number of optical components used in the setup is reduced to a minimum, because the THz optical components are essentially removed from the setup, resulting in a compact experimental setup. The only "component" with a big footprint will be the femtosecond laser. The possibility of delivering the pump pulses in the future using a fiber, will increase the ease of use of this spectrometer. The compactness and ease of use makes it a very good candidate for other industrial applications.

Bibliography

[1] N. Nagai, M. Sumitomo, M. Imaizumi, and R. Fukasawa, "Characterization of electron-or proton-irradiated Si space solar cells by THz spectroscopy," Semicond. Sci. Technol. **21**, 201 (2006).

[2] S. Nashima, O. Morikawa, K. Takata, and M. Hangyo, "Temperature dependence of optical and electronic properties of moderately doped silicon at terahertz frequencies," J. Appl. Phys. **90**, 837 (2001).

[3] D. Mittleman, S. Hunsche, L. Boivin, and M. Nuss, "T-ray tomography," Opt. Lett. **22**, 904 (1997).

[4] M. Beard, G. Turner, and C. Schmuttenmaer, "Subpicosecond carrier dynamics in low-temperature grown GaAs as measured by time-resolved terahertz spectroscopy," J. Appl. Phys. **90**, 5915 (2001).

[5] R. Woodward, B. Cole, V. Wallace, R. Pye, D. Arnone, E. Linfield, and M. Pepper, "Terahertz pulse imaging in reflection geometry of human skin cancer and skin tissue," Phys. Med. Biol. **47**, 3853 (2002).

[6] B. M. Fischer, M. Hoffmann, H. Helm, G. Modjesch, and P. U. Jepsen, "Chemical recognition in terahertz time-domain spectroscopy and imaging," Semicond. Sci. Technol **20**, 246 (2005).

[7] M. . Kemp, P. F. Taday, . E. Cole, J. A. Cluff, A. J. Fitzgerald, and W. R. Tribe, "Security applications of terahertz technology," Proc. SPIE **5070**, 45 (2003).

[8] M. Choi, A. Bettermann, and D. Van Der Weide, "Potential for detection of explosive and biological hazards with electronic terahertz systems," Philos. Trans. R. Soc. London, Ser. A **362**, 337 (2004).

[9] J. Lu, L. Chen, T. Kao, H. Chang, H. Chen, A. Liu, Y. Chen, R. Wu, W. Liu, J. Chyi, *et al.*, "Terahertz microchip for illicit drug detection," IEEE Photonics Technol. Lett. **18**, 2254 (2006).

[10] B. B. Hu and M. C. Nuss, "Imaging with terahertz waves," Opt. Lett. **20**, 1716 (1995).

[11] B. Ferguson, S. Wang, D. Gray, D. Abbot, and X. C. Zhang, "T-ray computed tomography," Opt. Lett. **27**, 1312 (2002).

[12] T. Yasuda, T. Yasui, T. Araki, and E. Abraham, "Real-time two-dimensional terahertz tomography of moving objects," Opt. Commun. **267**, 128 (2006).

[13] M. Nagel, P. H. Bolivar, M. Brucherseifer, H. Kurz, A. Bosserhoff, and R. Büttner, "Integrated THz technology for label-free genetic diagnostics," Appl. Phys. Lett. **80**, 154 (2002).

[14] H. Zhong, J. Xu, X. Xie, T. Yuan, R. Reightler, E. Madaras, and X. Zhang, "Nondestructive defect identification with terahertz time-of-flight tomography," IEEE Sens. J. **5**, 203 (2005).

[15] M. Brucherseifer, M. Nagel, P. Bolivar, H. Kurz, A. Bosserhoff, and R. Büttner, "Label-free probing of the binding state of DNA by time-domain terahertz sensing," Appl. Phys. Lett. **77**, 4049 (2000).

[16] S. Mickan, A. Menikh, H. Liu, C. Mannella, R. MacColl, D. Abbott, J. Munch, and X. Zhang, "Label-free bioaffinity detection using terahertz technology," Phys. Med. Biol. **47**, 3789 (2002).

[17] K. Kawase, Y. Ogawa, Y. Watanabe, and H. Inoue, "Non-destructive terahertz imaging of illicit drugs using spectral fingerprints," Opt. Express **11**, 2549 (2003).

[18] A. G. Markelz, A. Roitberg, and E. J. Heilweil, "Pulsed terahertz spectroscopy of DNA, bovine serum albumin and collagen between 0.1 and 2.0 THz," Chem. Phys. Lett. **320**, 42 (2000).

[19] M. Walther, B. Fischer, M. Schall, H. Helm, and P. U. Jepsen, "Far-infrared vibrational spectra of all-trans, 9-cis and 13-cis retinal measured by THz time-domain spectroscopy," Chem. Phys. Lett. **332**, 389 (2000).

[20] A. Menikh, R. MacColl, C. A. Mannella, and X. C. Zhang, "Terahertz biosensing technology: Frontiers and progress," Chem. Phys. Chem. **3**, 655 (2002).

[21] M. C. Beard, G. M. Turner, and C. A. Schmuttenmaer, "Terahertz spectroscopy," J. Phys. Chem. B **106**, 7146 (2002).

[22] P. H. Bolivar, M. Brucherseifer, J. G. Rivas, R. Gonzalo, I. Ederra, A. L. Reynolds, M. Holker, and P. de Maagt, "Measurement of the dielectric constant and loss tangent of high dielectric-constant materials at terahertz frequencies," IEEE Trans. Microwave Theory Tech. **51**, 1062 (2003).

[23] T. G. Phillips and J. Keene, "Submillimeter astronomy [heterodyne spectroscopy]," Proc. IEEE **80**, 1662 (1992).

[24] N. D. Whyborn, "The HIFI heterodyne instrument for FIRST: Capabilities and performance," Proc. ESA Symb.: The far infrared and submillimetre universe. **401**, 19 (1997).

[25] G. J. Melnick, J. R. Stauffer, M. L. N. Ashby, E. A. Bergin, G. Chin, N. R. Erickson, P. F. Goldsmith, M. Harwit, J. E. Howe, S. C. Kleiner, *et al.*, "The submillimeter wave astronomy satellite: Science objectives and instrument description," Astro. Phys. J. Lett. **539**, 77 (2000).

[26] D. P. Woody, J. Mather, N. S. Nishioka, and P. L. Richards, "Measurement of the spectrum of the submillimeter cosmic background," Phys. Rev. Lett. **34**, 1036 (1975).

[27] P. F. T. I. V. Bradley, D. D. Arnone, and M. Pepper, "Using terahertz pulse spectroscopy to study the crystalline structure of a drug: A case study of the polymorphs of ranitidine hydrochloride," J. Pharm. Sci **92**, 831 (2003).

[28] R. Beringer, "The absorption of one-half centimeter electromagnetic waves in oxygen," Phys. Rev. **70**, 53 (1946).

[29] W. Gordy, "Microwave spectroscopy," Rev. Mod. Phys. **20**, 668 (1948).

[30] D. J. Gardiner, P. R. Graves, and H. J. Bowley, *Practical Raman spectroscopy* (Springer-Verlag, Berlin, 1989).

[31] M. van Exter, C. Fattinger, and D. Grischkowsky, "Terahertz time-domain spectroscopy of water vapor," Opt. Lett **14**, 1128 (1989).

[32] C. H. Townes and A. L. Schawlow, *Microwave spectroscopy* (Courier Dover Publications, 1975).

[33] J. M. Hollas, *High resolution spectroscopy* (John Wiley, New York, 1998).

[34] G. Herzberg and B. L. Crawford Jr, "Infrared and Raman spectra of polyatomic molecules." J. Phys. Chem. **50**, 288 (1946).

[35] N. B. Colthup, L. H. Daly, and S. E. Wiberley, *Introduction to infrared and Raman spectroscopy* (Academic Press, New York, 1964).

[36] J. E. Stewart, *Infrared spectroscopy: Experimental methods and techniques* (Books on Demand, 1970).

[37] R. K. Khanna, D. D. Stranz, and B. Donn, "A spectroscopic study of intermediates in the condensation of refractory smokes: Matrix isolation experiments of SiO," J. Chem. Phys. **74**, 2108 (1981).

[38] D. I. Ellis and R. Goodacre, "Metabolic fingerprinting in disease diagnosis: biomedical applications of infrared and Raman spectroscopy," The Analyst **131**, 875 (2006).

[39] J. C. Bellows, F. P. Chen, and P. N. Prasad, "Determination of drug polymorphs by laser Raman Spectroscopy. I. Ampicillin and Griseofulvin," Drug Dev. Ind. Pharm. **3**, 451 (1977).

[40] D. A. Long, *Raman spectroscopy* (McGraw-Hill, NewYork, 1977).

[41] P. Hendra, "Fourier transform Raman spectroscopy," Lab. Pract. **39**, 61 (1990).

[42] B. D. Cullity, *Elements of X-ray Diffraction* (Addison-Wesley, 1978).

[43] P. R. Griffiths and J. A. De Haseth, *Fourier transform infrared spectrometry* (Wiley-Interscience, 2007).

[44] D. Shaw, *Fourier transform NMR spectroscopy* (Elsevier, 1976).

[45] A. Hadni, "A short history of 50 years of research in the far-infrared: 1952–2002," Int. J. Infrared Millimeter Waves **24**, 91 (2003).

[46] M. F. Kimmitt, "Restrahlen to T-rays–100 years of terahertz radiation," J. Biol. Phys. **29**, 77 (2003).

[47] W. Benedict, M. Pollack, and W. Tomlinson III, "The water-vapor laser," IEEE J. Quantum Electron. **5**, 108 (1969).

[48] D. H. Auston, K. P. Cheung, and P. R. Smith, "Picosecond photoconducting Hertzian dipoles," Appl. Phys. Lett. **45**, 284 (1984).

[49] D. H. Auston and M. C. Nuss, "Electrooptical generation and detection of femtosecond electrical transients," IEEE J. Quantum Electron. **24**, 184 (1988).

[50] X. C. Zhang, X. F. Ma, Y. Jin, T. M. Lu, E. P. Boden, P. D. Phelps, K. R. Stewart, and C. P. Yakymyshyn, "Terahertz optical rectification from a nonlinear organic crystal," Appl. Phys. Lett. **61**, 3080 (1992).

[51] H. Dember, "Photoelectromotive force in cuprous oxide crystals," Phys. Z. **32**, 554 (1931).

[52] T. Dekorsy, H. Auer, H. J. Bakker, H. G. Roskos, and H. Kurz, "THz electromagnetic emission by coherent infrared-active phonons," Phys. Rev. B: Condens. Matter **53**, 4005 (1996).

[53] X. C. Zhang, B. B. Hu, J. T. Darrow, and D. H. Auston, "Generation of femtosecond electromagnetic pulses from semiconductor surfaces," Appl. Phys. Lett. **56**, 1011 (1990).

[54] M. Bass, P. A. Franken, J. F. Ward, and G. Weinreich, "Optical rectification," Phys. Rev. Lett. **9**, 446 (1962).

[55] M. Saglam, B. Schumann, V. Müllerwiebus, A. Megej, U. Auer, M. Rodriguez-Girones, R. Judaschke, F. J. Tegude, and H. L. Hartnagel, "450 GHz millimetre-wave signal from frequency tripler with heterostructure barrier varactors on gold substrate," Electron. Lett **38**, 657 (2002).

[56] H. Eisele, A. Rydberg, and G. I. Haddad, "Recent advances in the performance of InP Gunn devices and GaAsTUNNETT diodes for the 100-300-GHz frequency range and above," IEEE Trans. Microwave Theory Tech. **48**, 626 (2000).

[57] S. Martin, B. Nakamura, A. Fung, P. Smith, J. Bruston, A. Maestrini, F. Maiwald, P. Siegel, E. Schlecht, and I. Mehdi, "Fabrication of 200 to 2700 GHz multiplier devices using GaAs and metal membranes," IEEE MTT-S Int. Micro. Symp. Dig. **3**, 1641 (2001).

[58] J. Bruston, A. Maestrini, D. Pukala, S. Martin, B. Nakamura, and I. Mehdi, "A 1.2 THz planar tripler using GaAs membrane based chips," Proc. 12th Int. Symp. Space Terahertz Technol. p. 310 (2001).

[59] D. W. Van Der Weide, J. S. Bostak, B. A. Auld, and D. M. Bloom, "All-electronic generation of 880 fs, 3.5 V shockwaves and their application to a 3 THz free-space signal generation system," Appl. Phys. Lett. **62**, 22 (1993).

[60] R. Kompfner and N. T. Williams, "Backward-wave tubes," Proc. IRE. **41**, 1602 (1953).

[61] F. Maiwald, S. Martin, J. Bruston, A. Maestrini, T. Crawford, and P. H. Siegel, "2. 7 THz waveguide tripler using monolithic membrane diodes," IEEE MTT-S Int. Micro. Symp. Dig. **1**, 1637 (2001).

[62] J. R. Morris and Y. R. Shen, "Theory of far-infrared generation by optical mixing," Phys. Rev. A: At. Mol. Opt. Phys. **15**, 1143 (1977).

[63] E. R. Brown, K. A. McIntosh, K. B. Nichols, and C. L. Dennis, "Photomixing up to 3.8 THz in low-temperature-grown GaAs," Appl. Phys. Lett. **66**, 285 (1995).

[64] J. Faist, F. Capasso, D. L. Sivco, C. Sirtori, A. L. . Hutchinson, and A. Y. Cho, "Quantum cascade lasers," Science **264**, 553 (1994).

[65] R. Köhler, A. Tredicucci, F. Beltram, H. E. Beere, E. H. Linfield, A. G. Davies, D. A. Ritchie, R. C. Iotti, and F. Rossi, "Terahertz semiconductor-heterostructure laser," Nature **417**, 156 (2002).

[66] F. Capasso, R. Paiella, R. Martini, R. Colombelli, C. Gmachl, T. L. Myers, M. S. Taubman, R. M. Williams, C. G. Bethea, K. Unterrainer, *et al.*, "Quantum cascade lasers: ultrahigh-speed operation, optical wirelesscommunication, narrow linewidth, and far-infrared emission," IEEE J. Quantum Electron. **38**, 511 (2002).

[67] K. Faist, D. Hofstetter, M. Beck, T. Aellen, M. Rochat, and S. Blaser, "Bound-to-continuum and two-phonon resonance, quantum-cascade lasersfor high duty cycle, high-temperature operation," IEEE J. Quantum Electron. **38**, 533 (2002).

[68] M. Dragoman, *Advanced optoelectronic devices* (Springer-Verlag, Berlin, 1999).

[69] G. Williams, "FAR-IR/THz radiation from the Jefferson Laboratory, energy recovered linac, free electron laser," Rev. Sci. Instrum. **73**, 1461 (2002).

[70] E. Grosse, "THz radiation from free electron lasers and its potential for cell and tissue studies," Phys. Med. Biol. **47**, 3755 (2002).

[71] M. Tretyakov, S. Volokhov, G. Golubyatnikov, E. Karyakin, and A. Krupnov, "Compact tunable radiation source at 180–1500 GHz frequency range," Int. J. Infrared Millimeter Waves **20**, 1443 (1999).

[72] J. T. Darrow, X. C. Zhang, D. H. Auston, and J. D. Morse, "Saturation properties of large-aperture photoconducting antennas," IEEE J. Quantum Electron. **28**, 1607 (1992).

[73] B. J. Baliga, R. Ehle, J. R. Shealy, and W. Garwacki, "Breakdown characteristics of gallium arsenide," IEEE Electron. Device Lett. **2**, 302 (1981).

[74] G. Zhao, R. N. Schouten, N. C. J. Van der Valk, W. T. Wenckebach, and P. C. M. Planken, "Design and performance of a THz emission and detection setup based on a semi-insulating GaAs emitter," Rev. Sci. Instrum. **73**, 1715 (2002).

[75] N. Katzenellenbogen and D. Grischkowsky, "Efficient generation of 380 fs pulses of THz radiation by ultrafast laser pulse excitation of a biased metal-semiconductor interface," Appl. Phys. Lett. **58**, 222 (1991).

[76] R. A. Kaindl, F. Eickemeyer, M. Woerner, and T. Elsaesser, "Broadband phase-matched difference frequency mixing of femtosecond pulses in GaSe: experiment and theory," Appl. Phys. Lett. **75**, 1060 (1999).

[77] A. Bonvalet, M. Joffre, J. L. Martin, and A. Migus, "Generation of ultrabroadband femtosecond pulses in the mid-infrared by optical rectification of 15 fs light pulses at 100 MHz repetition rate," Appl. Phys. Lett. **67**, 2907 (1995).

[78] R. Huber, A. Brodschelm, F. Tauser, and A. Leitenstorfer, "Generation and field-resolved detection of femtosecond electromagnetic pulses tunable up to 41 THz," Appl. Phys. Lett. **76**, 3191 (2000).

[79] N. C. J. Valk, "Toward terahertz microscopy." Ph.D. thesis, Delft university of technology (2005).

[80] C. Fattinger and D. Grischkowsky, "Point source terahertz optics," Appl. Phys. Lett. **53**, 1480 (1988).

[81] R. Williams, *Gallium arsenide processing techniques* (Artech House Norwood, MA, 1985).

[82] L. Duvillaret, F. Garet, J. F. Roux, and J. L. Coutaz, "Analytical modeling and optimization of terahertz time-domain spectroscopy experiments using photoswitches as antennas," IEEE J. Sel. Top. Quantum Electron. **7**, 615 (2001).

[83] P. U. Jepsen, R. H. Jacobsen, and S. R. Keiding, "Generation and detection of terahertz pulses from biased semiconductor antennas," J. Opt. Soc. Am. B **13**, 2424 (1996).

[84] S. Hughes and T. Kobayashi, "Ultrafast carrier-carrier scattering in wide-gap GaN semiconductor laser devices," Semicond. Sci. Technol. **12**, 733 (1997).

[85] G. Zhao, M. ter Mors, W. T. Wenckebach, and P. C. M. Planken, "Terahertz dielectric properties of polystyrene foam," J. Opt. Soc. Am. B **19**, 1476 (2002).

[86] P. C. M. Planken, H. K. Nienhuys, H. J. Bakker, and W. T. Wenckebach, "Measurement and calculation of the orientation dependence of terahertz pulse detection in ZnTe," J. Opt. Soc. Am. B: Opt. Phys. **18**, 313 (2001).

[87] D. S. Kim and D. S. Citrin, "Coulomb and radiation screening in photoconductive terahertz sources," Appl. Phys. Lett. **88**, 161,117 (2006).

[88] Y. R. Shen, "Far-infrared generation by optical mixing," Progr. Quant. Electron. **4**, 207 (1976).

[89] Y. C. Shen, P. C. Upadhya, E. H. Linfield, H. E. Beere, and A. G. Davies, "Ultrabroadband terahertz radiation from low-temperature-grown GaAs photoconductive emitters," Appl. Phys. Lett. **83**, 3117 (2003).

[90] C. Kubler, R. Huber, and A. Leitenstorfer, "Ultrabroadband terahertz pulses: Generation and field-resolved detection," Semicond. Sci. Technol. **20**, S128 (2005).

[91] A. Leitenstorfer, S. Hunsche, J. Shah, M. C. Nuss, and W. H. Knox, "Detectors and sources for ultrabroadband electro-optic sampling: Experiment and theory," Appl. Phys. Lett. **74**, 1516 (1999).

[92] A. Yariv, *Optical electronics* (Oxford University Press, 1990).

[93] B. Hu, X. Zhang, D. Auston, and P. Smith, "Free-space radiation from electro-optic crystals," Appl. Phys. Lett. **56**, 506 (1990).

[94] J. Faure, J. Van Tilborg, R. A. Kaindl, and W. P. Leemans, "Modelling laser-based table-top THz sources: optical rectification, propagation and electro-optic sampling," Opt. and Quantum Electron. **36**, 681 (2004).

[95] A. Nahata, A. S. Weling, and T. F. Heinz, "A wideband coherent terahertz spectroscopy system using optical rectification and electro-optic sampling," Appl. Phys. Lett. **69**, 2321 (1996).

[96] Q. Wu, "Broadband detection capability of ZnTe electro-optic field detectors," Appl. Phys. Lett. **68**, 2924 (1996).

[97] K. Liu, J. Xu, and X. C. Zhang, "GaSe crystals for broadband terahertz wave detection," Appl. Phys. Lett. **85**, 863 (2004).

[98] E. D. Palik, ed., *Handbook of optical constants of solids II* (Academic Press, Boston, 1991).

[99] H. J. Bakker, G. C. Cho, H. Kurz, Q. Wu, and X. C. Zhang, "Distortion of terahertz pulses in electro-optic sampling," J. Opt. Soc. Am. B **15**, 1795 (1998).

[100] A. N. Pikhtin, V. T. Prokopenko, and A. D. Yaskov, "Refraction of light in Gallium Phosphide." Zhurnal Prikladnoi Spektroskopii. **27**, 308 (1977).

[101] M. van Exter, C. Fattinger, and D. Grischkowsky, "High-brightness terahertz beams characterized with an ultrafast detector," Appl. Phys. Lett. **55**, 337 (1989).

[102] P. U. Jepsen, C. Winnewisser, M. Schall, V. Schyja, S. R. Keiding, and H. Helm, "Detection of THz pulses by phase retardation in lithium tantalate," Phys. Rev. E **53**, R3052 (1996).

[103] N. C. J. van der Valk, P. C. M. Planken, A. N. Buijserd, and H. J. Bakker, "Influence of pump wavelength and crystal length on the phase matching of optical rectification," J. Opt. Soc. Am. B **22**, 1714 (2005).

[104] G. Gallot and D. Grischkowsky, "Electro-optic detection of terahertz radiation," J. Opt. Soc. Am. B **16**, 1204 (1999).

[105] C. Dahl, L. Genzel, P. Goy, G. Gruner, J. P. Kotthaus, G. Kozlov, M. C. Nuss, J. Orenstein, and A. Volkov, *Millimeter and submillimeter wave spectroscopy of solids, Terahertz time-domain spectroscopy* (Springer-Verlag, Berlin, 1998).

[106] D. M. Mittleman, R. H. Jacobsen, and M. C. Nuss, "T-ray imaging," IEEE J. Sel. Top. Quantum Electron. **2**, 679 (1996).

[107] D. M. Mittleman, M. Gupta, R. Neelamani, R. G. Baraniuk, J. V. Rudd, and M. Koch, "Recent advances in terahertz imaging," Appl. Phys. B **68**, 1085 (1999).

[108] D. M. Mittleman, R. H. Jacobsen, R. Neelamani, R. G. Baraniuk, and M. C. Nuss, "Gas sensing using terahertz time-domain spectroscopy," Appl. Phys. B **67**, 379 (1998).

[109] M. Walther, B. M. Fischer, and P. U. Jepsen, "Noncovalent intermolecular forces in polycrystalline and amorphous saccharides in the far infrared," Chem. Phys. **288**, 261 (2003).

[110] C. Rønne and S. R. Keiding, "Low frequency spectroscopy of liquid water using THz-time domain spectroscopy," J. Mol. Liq. **101**, 199 (2002).

[111] D. S. Venables, A. Chiu, and C. A. Schmuttenmaer, "Structure and dynamics of nonaqueous mixtures of dipolar liquids. I. Infrared and far-infrared spectroscopy," J. Chem. Phys. **113**, 3243 (2000).

[112] R. A. Cheville and D. Grischkowsky, "Far-infrared foreign and self-broadened rotational linewidths of high-temperature water vapor," J. Opt. Soc. Am. B: Opt. Phys. **16**, 317 (1999).

[113] P. U. Jepsen, U. Møller, and H. Merbold, "Investigation of aqueous alcohol and sugar solutions with reflection terahertz time-domain spectroscopy," Opt. Express **15**, 14717 (2007).

[114] P. F. Taday, "Applications of terahertz spectroscopy to pharmaceutical sciences," Philos. Trans. R. Soc. London, Ser. A **362**, 351 (2004).

[115] E. Hecht, *Optics* (Pearson education, India, 2002).

[116] M. Franz, B. M. Fischer, and M. Walther, "The Christiansen effect in terahertz time-domain spectra of coarse-grained powders," Appl. Phys. Lett. **92**, 021107 (2008).

[117] B. M. Fischer, H. Helm, and P. U. Jepsen, "Chemical recognition with broad band THz spectroscopy," Proc. IEEE **95**, 1592 (2007).

[118] C. A. Beevers, T. R. R. McDonald, H. J. Robertson, and F. Stern, "The crystal structure of sucrose," Acta Cryst. **5**, 689 (1952).

[119] P. C. Upadhya, Y. C. Shen, A. G. Davies, and E. H. Linfield, "Far-infrared vibrational modes of polycrystalline saccharides," Vib. Spectrosc. **35**, 139 (2004).

[120] L. Yang, H. Sun, S. Weng, K. Zhao, L. Zhang, G. Zhao, Y. Wang, Y. Xu, X. Lu, C. Zhang, *et al.*, "Terahertz absorption spectra of some saccharides and their metal complexes," Spectrochim. Acta, Part A **69**, 160 (2008).

[121] S. K. Husain, J. B. Hasted, D. Rosen, E. Nicol, and J. R. Birch, "FIR spectra of amino acids and related molecules," Infrared Phys. **24**, 201 (1984).

[122] L. Yang, S. Weng, J. R. Ferraro, and J. Wu, "Far infrared study of some mono-and disaccharides," Vib. Spectrosc. **25**, 57 (2001).

[123] R. Nossal and H. Lacar, *Molecular and cell biophysics* (Addison-Wesley, California, 1991).

[124] K. Yamamoto, K. Tominaga, H. Sasakawa, A. Tamura, H. Murakami, H. Ohtake, and N. Sarukura, "Far-infrared absorption measurements of polypeptides and cytochrome c by THz radiation," Bull. Chem. Soc. Jpn. **75**, 1083 (2002).

[125] P. G. Jonsson and A. Kvick, "Precision neutron diffraction structure determination of protein and nucleic acid components. III. The crystal and molecular structure of the amino acid-glycine," Acta Crystallogr., Sect. B: Struct. Sci **28**, 1827 (1972).

[126] T. M. Korter, R. Balu, M. B. Campbell, M. C. Beard, S. K. Gregurick, and E. J. Heilweil, "Terahertz spectroscopy of solid serine and cysteine," Chem. Phys. Lett. **418**, 65 (2006).

[127] A. Matei, N. Drichko, B. Gompf, and M. Dressel, "Far-infrared spectra of amino acids," Chem. Phys. **316**, 61 (2005).

[128] M. Yamaguchi, F. Miyamaru, K. Yamamoto, M. Tani, and M. Hangyo, "Terahertz absorption spectra of L-, D-, and DL-alanine and their application to determination of enantiometric composition," Appl. Phys. Lett. **86**, 053903 (2005).

[129] N. T. McDevitt and A. D. Davidson, "Infrared study of Ag2O in the low-frequency region," J. Opt. Soc. Am. **55**, 209 (1965).

[130] C. Carabatos and B. Prevot, "Rigid ion model lattice dynamics of cuprite (Cu_2O)," Phys. Status Solidi B **44**, 701 (1971).

[131] D. Banerjee, W. von Spiegel, M. D. Thomson, S. Schabel, and H. G. Roskos, "Diagnosing water content in paper by terahertz radiation," Opt. Express **16**, 9060 (2008).

[132] S. Hadjiloucas, L. S. Karatzas, and J. W. Bowen, "Measurements of leaf water content using terahertz radiation," IEEE Trans. Microwave Theory Tech. **47**, 142 (1999).

[133] W. G. Terence, F. Rowe, and J. W. Snowman, *Edwards freeze drying handbook* (1976).

[134] X. Tang and M. J. Pikal, "Design of freeze-drying processes for pharmaceuticals: practical advice," Pharm. Res. **21**, 191 (2004).

[135] A. I. Kim, M. J. Akers, and S. L. Nail, "The physical state of mannitol after freeze-drying: effects of mannitol concentration, freezing rate, and a noncrystallizing cosolute," J. Pharm. Sci. **87**, 931 (1998).

[136] J. Haleblian and W. McCrone, "Pharmaceutical applications of polymorphism." J. Pharm. Sci. **58**, 911 (1969).

[137] D. Singhal and W. Curatolo, "Drug polymorphism and dosage form design: A practical perspective," Adv. Drug Delivery Rev. **56**, 335 (2004).

[138] J. D. Dunitz, "Phase transitions in molecular crystals from a chemical viewpoint," Pure Appl. Chem. **63**, 177 (1991).

[139] T. Yoshinari, R. T. Forbes, P. York, and Y. Kawashima, "Moisture induced polymorphic transition of mannitol and its morphological transformation," Int. J. Pharm. **247**, 69 (2002).

[140] L. Shargel and A. B. Yu, *Applied biopharmaceutics and pharmacokinetics* (McGraw-Hill, New York, 1999).

[141] J. Bauer, S. Spanton, R. Henry, J. Quick, W. Dziki, W. Porter, and J. Morris, "Ritonavir: An extraordinary example of conformational polymorphism," Pharm. Res. **18**, 859 (2001).

[142] S. R. Chemburkar, J. Bauer, K. Deming, H. Spiwek, K. Patel, J. Morris, R. Henry, S. Spanton, W. Dziki, W. Porter, *et al.*, "Dealing with the impact of ritonavir polymorphs on the late stages of bulk drug process development," Org. Proc. Res. Dev. **4**, 413 (2000).

[143] R. Suryanarayanan and C. S. Herman, "Quantitative analysis of the active tablet ingredient by powder X-Ray diffractometry," Pharm. Res. **8**, 393 (1991).

[144] N. V. Phadnis, R. K. Cavatur, and R. Suryanarayanan, "Identification of drugs in pharmaceutical dosage forms by X-ray powder diffractometry," J. Pharm. Biomed. Anal. **15**, 929 (1997).

[145] J. Anwar, S. E. Tarling, and P. Barnes, "Polymorphism of sulfathiazole." J. Pharm. Sci. **78**, 337 (1989).

[146] G. Bettinetti, F. Giordano, G. Fronza, A. Italia, R. Pellegata, M. Villa, and P. Ventura, "Sobrerol enantiomers and racemates: Solid-state spectroscopy, thermal behavior, and phase diagrams," J. Pharm. Sci. **79**, 470 (1990).

[147] L. S. Taylor and F. W. Langkilde, "Evaluation of solid-state forms present in tablets by Raman spectroscopy," J. Pharm. Sci. **89**, 1342 (2000).

[148] S. N. Campbell Roberts, A. C. Williams, I. M. Grimsey, and S. W. Booth, "Quantitative analysis of mannitol polymorphs. FT-Raman spectroscopy," J. Pharm. Biomed. Anal. **28**, 1135 (2002).

[149] C. M. Deeley, R. A. Spragg, and T. L. Threlfall, "A comparison of Fourier transform infrared and near-infrared Fourier transform Raman spectroscopy for quantitative measurements: an application in polymorphism," Spectrochim. Acta **47**, 1217 (1991).

[150] A. M. Tudor, S. J. Church, P. J. Hendra, M. C. Davies, and C. D. Melia, "The qualitative and quantitative analysis of chlorpropamide

polymorphic mixtures by near-infrared Fourier transform Raman spectroscopy," Pharm. Res. **10**, 1772 (1993).

[151] M. E. Auer, U. J. Griesser, and J. Sawatzki, "Qualitative and quantitative study of polymorphic forms in drug formulations by near infrared FT-Raman spectroscopy," J. Mol. Struct. **661**, 307 (2003).

[152] B. Shah, V. K. Kakumanu, and A. K. Bansal, "Analytical techniques for quantification of amorphous/crystalline phases in pharmaceutical solids." J. Pharm. Sci. **95**, 1641 (2006).

[153] R. K. Cavatur and R. Suryanarayanan, "Characterization of phase transitions during freeze drying by in situ X-ray powder diffractometry," Pharm. Dev. Technol. **3**, 579 (1998).

[154] A. B. de González and S. Darby, "Risk of cancer from diagnostic X-rays: estimates for the UK and 14 other countries," Lancet **363**, 345 (2004).

[155] E. Rasanen and N. Sandler, "Near infrared spectroscopy in the development of solid dosage forms," J. Pharm. Pharmacol. **59**, 147 (2007).

[156] G. X. Zhou, Z. Ge, J. Dorwart, B. Izzo, J. Kukura, G. Bicker, and J. Wyvratt, "Determination and differentiation of surface and bound water in drug substances by near infrared spectroscopy," J. Pharm. Sci. **92**, 1058 (2003).

[157] R. G. Messerschmidt and D. B. Chase, "FT-Raman microscopy: Discussion and preliminary results," Appl. Spectrosc. **41**, 1125 (1987).

[158] F. J. Bergin and H. F. Shurvell, "Applications of fourier transform Raman spectroscopy in an industrial laboratory," Appl. Spectrosc. **43**, 516 (1989).

[159] T. R. M. De Beer, P. Vercruysse, A. Burggraeve, T. Quinten, J. Ouyang, X. Zhang, C. Vervaet, J. P. Remon, and W. R. G. Baeyens, "In-line and real-time process monitoring of a freeze drying process using Raman and NIR spectroscopy as complementary process analytical technology (PAT) tools," Anal. Chem. **79**, 7992 (2009).

[160] S. Romero-Torres, H. Wikström, E. R. Grant, and L. S. Taylor, "Monitoring of mannitol phase behavior during freeze drying using noninvasive Raman spectroscopy." PDA J. Pharm. Sci. Technol. **61**, 131 (2007).

[161] A. Fitch, P. N. Gates, K. Radcliffe, F. N. Dickson, and F. F. Bently, *Chemical Applications of Far Infrared Spectroscopy* (Academic Press, New York, 1970).

[162] W. Chantry, *Submillimetre spectroscopy* (Academic Press, New York, 1971).

[163] M. B. Johnston, L. M. Herz, A. L. T. Khan, A. Köhler, A. G. Davies, and E. H. Linfield, "Low-energy vibrational modes in phenylene oligomers studied by THz time-domain spectroscopy," Chem. Phys. Lett. **377**, 256 (2003).

[164] A. M. Fedor and T. M. Korter, "Terahertz spectroscopy of 7-azaindole clusters in solution," Chem. Phys. Lett. **429**, 405 (2006).

[165] J. Barber, D. E. Hooks, D. J. Funk, R. D. Averitt, A. Taylor, and D. Babikov, "Temperature-dependent far-infrared spectra of single crystals of high explosives using terahertz time-domain spectroscopy," J. Phys. Chem. A **109**, 350 (2005).

[166] Y. C. Shen, P. C. Upadhya, E. H. Linfield, and A. G. Davies, "Temperature-dependent low-frequency vibrational spectra of purine and adenine," Appl. Phys. Lett. **82**, 2350 (2003).

[167] C. J. Strachan, P. F. Taday, D. A. Newnham, K. C. Gordon, J. A. Zeitler, M. Pepper, and T. Rades, "Using terahertz pulsed spectroscopy to quantify pharmaceutical polymorphism and crystallinity," J. Pharm. Sci. **94**, 837 (2005).

[168] R. K. Cavatur, N. M. Vemuri, A. Pyne, Z. Chrzan, D. Toledo-Velasquez, and R. Suryanarayanan, "Crystallization behavior of mannitol in frozen aqueous solutions," Pharm. Res. **19**, 894 (2002).

[169] C. Telang, R. Suryanarayanan, and L. Yu, "Crystallization of d-mannitol in binary mixtures with NaCl: Phase diagram and polymorphism," Pharm. Res. **20**, 1939 (2003).

[170] A. Pyne, R. Surana, and R. Suryanarayanan, "Crystallization of mannitol below T_g during freeze drying in binary and ternary aqueous systems," Pharm. Res. **19**, 901 (2002).

[171] A. Burger, J. O. Henck, S. Hetz, J. M. Rollinger, A. Weissnicht, and H. Stottner, "Energy / temperature diagram and compression behavior of the polymorphs of D-mannitol," J. Pharm. Sci. **89**, 457 (2000).

[172] F. R. Fronczek, H. N. Kamelb, and M. Slattery, "Three polymorphs (α, β, and δ) of d-mannitol at 100 K," Acta Crystallogr., Sect. C: Cryst. Struct. Commun. **C59**, 567 (2003).

[173] L. Yu, N. Milton, E. G. Groleau, D. S. Mishra, and R. Vansickle, "Existence of a mannitol hydrate during freeze drying and practical implications," J. Pharm. Sci. **88**, 196 (1999).

[174] H. M. Berman, G. A. Jeffrey, and R. D. Rosenstein, "The crystal structures of the α and β forms of d-mannitol," Acta Crystallogr., Sect. B: Struct. Sci. **24**, 442 (1968).

[175] M. G. Fakes, M. V. Dali, T. A. Haby, K. R. Morris, S. A. Varia, and A. Serajuddin, "Moisture sorption behavior of selected bulking agents used in lyophilized products," PDA J. Pharm. Sci. Technol. **54**, 144 (2000).

[176] H. R. Costantino, J. D. Andya, P. A. Nguyen, N. Dasovich, T. Sweeney, S. Shire, C. Hsu, and Y. Maa, "Effect of mannitol crystallization on the stability and aerosol performance of a spray-dried pharmaceutical protein, recombinant humanized anti-IgE monoclonal antibody," J. Pharm. Sci. **87**, 1406 (1998).

[177] K. I. Izutsu, S. Yoshioka, and T. Terao, "Effect of mannitol crystallinity on the stabilization of enzymes during freeze-drying," Chem. Pharm. Bull. **42**, 5 (1994).

[178] I. Ki, S. Yoshioka, and T. Terao, "Decreased protein-stabilizing effects of cryoprotectants due to crystallization," Pharm. Res. **10**, 1232 (1993).

[179] M. J. Pikal, "Freeze-drying of proteins: Part I. Process design." Biopharm. **3**, 18 (1990).

[180] E. Y. Shalaev and F. Franks, "Changes in the physical state of model mixtures during freezing and drying: Impact on product quality," Cryobiology **33**, 14 (1996).

[181] J. F. Carpenter, M. J. Pikal, B. S. Chang, and T. W. Randolph, "Rational design of stable lyophilized protein formulations: some practical advice," Pharm. Res. **14**, 969 (1997).

[182] J. F. Carpenter and J. H. Crowe, "An infrared spectroscopic study of the interactions of carbohydrates with dried proteins," Biochemistry **28**, 3916 (1989).

[183] L. Walter-Levi, "The crystalline varieties of d-mannitol (in French)," C. R. Acad. Sci. Paris **267**, 1779 (1968).

[184] D. A. Newnham and P. F. Taday, "Pulsed terahertz attenuated total reflection spectroscopy," Appl. Spectrosc. **62**, 394 (2008).

[185] Y. Watanabe, K. Kawase, T. Ikari, H. Ito, Y. Ishikawa, and H. Minamide, "Component analysis of chemical mixtures using terahertz spectroscopic imaging," Opt. Commun. **234**, 125 (2004).

Summary

Everyday we see around us many materials that are different from one another. We identify them on the basis of their shape, texture, smell, taste, color, etc with the help of our senses. Many times it is almost impossible to identify materials only with our senses. Then, one has to look into more fundamental aspects of the materials such as their atomic or molecular constituents. Different techniques exist to identify and characterize materials. Spectroscopy is one such technique. Spectroscopy relies on the frequency selective emission or absorption of electromagnetic radiation by the materials to get information about their physical/chemical properties. There are different spectroscopic techniques to study materials and their interaction with electromagnetic radiation.

Terahertz (THz) radiation is the part of electromagnetic spectrum, which lies between the microwave and infrared regions of the electromagnetic spectrum. It is loosely defined as the frequency range from 0.1 to 10 THz. Terahertz radiation can penetrate a wide range of materials: paper, wood, plastics, fabric, ceramics, semiconductors, and many others that are often opaque to visible and near-infrared (NIR) radiation. Many materials have characteristic absorption bands in the THz region. Thus, in THz imaging applications, apart from getting a THz image, the measurement can also give spectroscopic information on the samples under study, which can be used to identify the materials. In principle, this spectroscopic imaging makes it possible to identify the contents inside a package without even opening it.

There exist various techniques to generate terahertz (THz) radiation. In photo-conductive antennas (PCAs), a time-dependent polarization is formed when charge carriers, created by a femtosecond laser pulse, are accelerated in an externally applied electric field. PCAs are capable of generating broadband pulses with a fairly high power. The THz generation and detection setup with the photo-conductive antenna as the THz source and electro-optic sampling as the THz detector as described in Chapter 2 gives a very high SNR of ~15000 in a measurement time of 10 ms. Even though our femtosecond laser pulses have a very high peak power, the generated THz power could not be increased further with increasing laser pump power on the emitter, because of emitter saturation. Increasing the laser spot size on the emitter gives a higher THz peak power than in the case of a tightly focused pump beam.

Among the different techniques to generate THz radiation, the tech-

nique using the optical conversion of extremely short pulses of light into THz pulses at a high repetition rate is very popular. These short laser pulses are partially converted into THz light in certain non-linear optical media. By using coherent detection techniques, the amplitude and phase of the THz pulse can be detected in the time domain. This spectroscopic technique is called terahertz time domain spectroscopy (THz-TDS).

A typical THz-TDS setup has a long THz beam path. Atmospheric water vapor, present also in the beam path, has many strong absorption bands in the THz region, which makes it difficult to perform spectroscopy on samples. Such a setup should therefore be flushed with dry N_2 gas to reduce absorption of the THz radiation by water vapor molecules in the atmosphere. Typically, a THz-TDS setup also requires parabolic mirrors to collimate, steer and focus the THz radiation onto the detection crystal which is complicated by the fact that THz radiation is invisible. Furthermore, the THz beam diffraction and absorption at the reflecting surfaces in the THz beam path will lead to reduction of the THz power. One way to overcome all these problems is by placing the THz source and detector very close to each other. Apart from its simplicity, the advantage of such a quasi-near field terahertz spectrometer is that it can also provide a broad bandwidth (0.5-7 THz) and a good signal-to-noise ratio even without the use of lock-in detection.

THz radiation is generated by optical rectication of 50 fs, 800 nm pulses from a Ti:sapphire oscillator in suitable nonlinear optical crystals such as GaP. The shape and bandwidth of the spectra of the THz pulses generated in this way, are explained with a simple model, which takes into account the effects of phase-matching and absorption of THz radiation in the generation and detection crystals. If one wants to increase the generated bandwidth to frequencies above the phonon resonance frequency, then very short laser pulses (~10 fs) and very thin crystals (~50 μm) should be used. An important point to note is that the probe and the THz pulses are initially counter propagating and, after reflecting, co-propagating in the detection crystal. Both the calculations and the experimental results show that the effect of counter propagation of the THz pulse and the probe pulse in the detection crystal is negligible at higher frequencies, above a few hundred GHz.

Samples can be inserted between the generation and detection crystals, and their absorption spectra can be measured. As the THz beam propagates, it is expected to show a frequency-dependent divergence. This changes when a sample is placed between the generation and detection

crystals, making it more difficult to obtain the absolute absorption coefficient. However, this has no effect on the ability of the setup to identify materials by their spectral fingerprint. This is shown in Chapter 4, which contains measured absorption spectra of, D-tartaric acid, certain amino acids, sugars and metal oxides, in the frequency range of 0.5-7 THz.

Another exciting application of THz-TDS, as described in this thesis, is the identification of polymorphs in freeze dried mannitol. Freeze drying is very commonly used in the pharmaceutical industry to increase the shelf life and dry state stabilization of the therapeutic agents, where polymorphism is identified as a serious problem. These polymorphs often can have unique physical and chemical characteristics that can influence their stability, solubility and other performance characteristics. It is important for the pharmaceutical industry to know which polymorph is formed during the freeze drying process.

The measured THz absorption spectra of the β and δ polymorphs of mannitol from 0.5 THz to 7 THz, have distinct THz absorption spectra as shown in Chapter 5, especially between 2.5 and 6 THz. Because THz-TDS can be used to identify the polymorphs of mannitol, we have subsequently used this technique to study the effect of various freeze drying techniques on the formation of these polymorphs. The results show that, for mannitol, changes in the way the material is frozen can result in the formation of different polymorphs or a mixture of polymorphs, as supported by X-ray diffraction measurements performed on these samples. The THz-TDS has the added advantage that it may be relatively easy to employ as an in-line and, almost, real time monitoring tool, unlike X-ray diffraction analysis.

Reshmi Chakkittakandy.
Delft, December 2009.

Samenvatting

Iedere dag zien we om ons heen materialen die van elkaar verschillen. We onderscheiden ze met onze zintuigen op basis van vorm, textuur, geur, smaak, kleur, enz. Vaak is het echter onmogelijk om materialen van elkaar te onderscheiden door alleen onze zintuigen te gebruiken. Om dit wel te bereiken moet er naar de fundamentele aspecten van de materialen gekeken worden zoals de atomaire of moleculaire structuur. Er bestaan verschillende technieken om materialen te identificeren of te karakteriseren. Spectrosopie is zon techniek. Spectroscopie gebruikt frequentie selectieve emissie of absorptie van elektromagnetische straling om informatie over de fysische / chemische eigenschappen van materialen te verkrijgen. Er bestaan verschillende spectroscopische technieken om materialen en hun interactie met elektromagnetische straling te bestuderen.

Terahertz (THz) straling is het deel van het elektromagnetisch spectrum dat ligt tussen het gebied van de microgolven en het infrarood. Het is grofweg gedefinieerd als het frequentiegebied van 0.1 tot 10 THz. Terahertz straling gaat door een heel scala aan materialen, zoals papier, hout, plastic, stof, ceramiek, halfgeleiders en nog vele andere die vaak ondoorzichtig zijn voor zichtbaar licht en nabij-infrarood straling. Veel materialen hebben karakteristieke absorptiebanden in het THz gebied. In THz imaging applicaties kan de meting daarom, naast een THz beeld, ook spectroscopische informatie opleveren van de bestudeerde samples die gebruikt kan worden om de materialen te identificeren. In principe maakt de spectroscopie het dus mogelijk om de inhoud binnen een verpakking te identificeren zonder die te moeten openen.

Er zijn verschillende manieren om Terahertz straling te genereren. In photo-geleidende antennes (PCAs) wordt een tijdsafhankelijke polarisatie gevormd wanneer ladingsdragers, die gecreerd worden door een femtoseconde laser puls, versneld worden in een extern aangelegd elektrisch veld. PCAs zijn in staat een breedbandige puls te leveren met een aanzienlijk vermogen. De opstelling voor detectie en opwekking van THz straling, met de foto-geleidende antenne als bron en de electro-optische bemonstering als THz detector, zoals beschreven in hoofdstuk 2, geeft een zeer hoge SNR van ~15000 binnen een totale meettijd van 10 ms. Hoewel onze femtoseconde laser pulsen een relatief hoog piekvermogen hebben, kon het THz vermogen niet eenvoudig verder worden verhoogd het laser pompvermogen op de emitter te verhogen, vanwege optische verzadiging van de emitter. Vergroten van de laserspotgrootte aan de emitterzijde

geeft een hoger THz piekvermogen dan in het geval van een sterk gefocusseerde pompbundel.

Onder de verschillende technieken om THz straling op te wekken is de optische conversiemethode erg populair. Hierbij worden, kort op elkaar volgend, extreem korte lichtpulsen omgezet in THz pulsen. Deze korte lichtpulsen worden gedeeltelijk omgezet in THz licht in een niet-lineair optisch medium. Door gebruik te maken van coherente detectietechnieken kan de amplitude en fase van de THz puls gedetecteerd worden in het tijddomein. Deze spectroscopische techniek wordt Terahertz tijddomein spectroscopie (THz-TDS) genoemd.

Een typische THz-TDS opstelling heeft een lang pad voor de THz bundel. Atmosferische waterdamp, die aanwezig is in het pad van de bundel, heeft sterke absorptiebanden in het THz gebied, wat het moeilijk maakt om spectroscopie aan de samples te doen. Zon opstelling moet daardoor gespoeld worden met droog stikstof gas om de absorptie van de THz straling door de aanwezige waterdampmoleculen te verlagen Een typische THz-TDS opstelling heeft ook parabolische spiegels nodig om de THz straling te kunnen collimeren, sturen en te focusseren op het detectie kristal, wat weer moeilijk is vanwege het feit dat THz straling onzichtbaar is. Bovendien leidt diffractie en absorptie van de THz bundel op reflecterende oppervlakken, aanwezig in het pad van de THz bundel, tot verlaging van het THz vermogen. Een methode om al deze problemen te voorkomen is door de THz bron en detector erg dicht bij elkaar te plaatsen. Afgezien van de eenvoud van deze oplossing, is het voordeel van zon quasi nabije veld Terahertz spectrometer dat deze een brede bandbreedte oplevert (0.5 -7 THz) en een goede signaal-ruisverhouding, zelfs zonder het gebruik van lock-in detectie technieken.

THz straling wordt gegenereerd door optische rectificatie van 50 fs, 800 nm pulsen van een Ti:saffier oscillator in bruikbare niet-lineaire optische kristallen zoals GaP. De vorm en de bandbreedte van de spectra van de op deze manier gegenereerde THz pulsen worden met behulp van een eenvoudig model verklaard. Dit model houdt rekening met de effecten van verschillende fasesnelheden van THz licht en 800 nm licht en met absorptie van de THz straling in de kristallen tijdens de opwekking en gedurende de detectie. Wanneer men de opgewekte bandbreedte wil vergroten tot frequenties boven de fononresonantiefrequentie dan moeten zeer korte laserpulsen (~10 fs) en erg dunne kristallen (~50 μm) gebruikt worden. Een belangrijk punt om op te merken is dat de probe en de THz pulsen in het begin contra-propagerend zijn en na reflectie co-propagerend zijn

in het detectie kristal. Zowel berekeningen als experimenten laten zien dat het effect van contra-propagatie van de THz puls en de probe puls in het detectiekristal verwaarloosbaar is voor frequenties hoger dan een paar honderd GHz,

De samples kunnen tussen het generatie en detectie kristal geplaatst worden waarna de absorptiespectra gemeten kunnen worden. We verwachten dat de THz bundel een frequentie-afhankelijke divergentie vertoont wanneer deze propageert. Dit verandert echter wanneer een sample geplaatst wordt tussen het generatie- en detectiekristal, omdat het dan moeilijk wordt de absolute waarde van de absorptiecoefficient te meten. Voor de toepasbaarheid van de methode om de materialen te identificeren op basis van hun spectrale vingerafdruk heeft dit echter geen consequenties. Dit wordt aangetoond in hoofdstuk 4, waar gemeten absorptie spectra van D-tartaric acid, verschillende aminozuren, suikers en metaaloxiden te zien zijn in het frequentiegebied van 0.5-7 THz.

Een andere belangrijke toepassing van THz-TDS, zoals beschreven in dit proefschrift, is de identificatie van polymorfen in gevriesdroogd mannitol. Vriesdrogen wordt veelvuldig gebruikt in de farmaceutische industrie om de levensduur van produkten te verhogen. Stabilisatie van de droge toestand van de therapeutische middelen waar polymorfisme is gedentificeerd is een serieus probleem. Deze polymorfen hebben vaak unieke fysische en chemische karakteristieken die van invloed zijn op hun stabiliteit, oplosbaarheid en andere eigenschappen. Voor de farmaceutische industrie is het dus belangrijk te weten welk polymorf gevormd wordt tijdens het vriesdroogproces.

De gemeten THz absorptie spectra van β en δ polymorfen van mannitol zijn in het gebied van 0.5-7 THz verschillend, vooral tussen de 2.5 en 6 THz. Doordat THz-TDS gebruikt kan worden om de polymorfen van mannitol te identificeren hebben we deze techniek gebruikt om het effect van verschillende vriesdroogmethoden op de formatie van polymorfen te bestuderen. De resultaten laten zien dat verandering van de manier van bevriezen resulteert in de formatie van verschillende polymorfen of mengsels van polymorfen. Deze resultaten werden bevestigd door Röntgendiffractie metingen aan dezelfde samples. Echter, THz-TDS heeft als voordeel dat het relatief makkelijk te realiseren is in een productielijn en bovendien bijna real-time monitoring toelaat in tegenstelling tot de Röntgen diffractieanalyse.
Reshmi Chakkittakandy.
Delft, December 2009.

Acknowledgements

Many people have contributed to this thesis in many different ways and those I mention here are only a few faces from that large crowd.

I am indebted to Paul Planken for accepting me as a PhD student and giving me the opportunity to be part of the Optica. His door has always been open for questions and problems. His criticisms always lead to improved understanding and better quality. Many thanks to Paul, for his confidence in me, for helping me to complete this PhD research and for investing enormous effort and time with reading and correcting the manuscripts.

I would like to extend my words of gratitude to the past and present group leaders Joseph Braat and Paul Urbach for all the encouragements and support they have provided.

I am grateful to FOM for employing me as a PhD student and providing all the support and for offering various courses on improving professional and personal skills. A special word of gratitude goes to Ms. Annette Bor for taking care of all those paperwork.

Let me score my very best sense of gratitude to all the committee members for their time in reading my thesis and for suggestions.

I take this opportunity to place on record commendable help received from Jos Corver. His enthusiasm in doing experiments was really very motivating.

I am very thankful to Ruud Hendrix for the X-ray analysis on our samples. His help is greatly appreciated.

It is with great pleasure, I record my sincere thanks to Raymond for all the time he had invested in solving various experimental problems related to electronics. The questions he asked when approached with problems were always to the point and forced me to think further. This thesis would have been impossible without the help from Rob in designing and making various components for the experimental setup. I would like to acknowledge Marnix and Thim for taking care of all the safety issues of working in the lab. I thankfully bear in mind the help extended by Roland especially taking care of the computer hardware and software problems. Yvonne and Lucia deserve special words of gratitude for providing all the organizational help.

Aurele is always there to discuss the issues in the research or anything under the Sun, and he has always surprised me with his remarkable social skills. I remember the great time attending conferences together. Many

thanks to Aurele for all the help. I am thankful to Joe for all the help with experiments and for his willingness to discuss problems.

It is with great pleasure, I express my wholehearted thanks to Man for being a great office mate and a friend. She has been very helpful and supportive all these years and was the first person for me to ask for anything. Aura was one of the most welcoming faces in the group during my initial days in the group. Special thanks goes to Man and Aura for supporting me as paranymphs.

One of the fun makers of the group was Julien. He was the one who introduced me or at times persuaded me to the coffee breaks and helped me to be more sociaal. He was a real Matlab helpdesk for me. Many thanks Julien for all the help and also for the good time in San Francisco.

I am indebted to Gopakumar for all the support he has offered me since he joined the group. He is a great googler for information and is ever willing to discuss results. I enjoyed doing experiments with him. I thankfully remember help, support and company from Sven especially during the very last and difficult stages of this thesis. I am grateful to Omar for being very open for any questions and his willingness to help. Thanks to Maarten and Pascal for all the good times in the group and bravo to Maarten for trying out Indian food at my home. I will keep in mind Mounir's generosity, for sparing my life even though I did not attend all the PhD lunches. Thanks to Gopika for the good time and her help in the difficult task of spiral binding.

Sincere thanks are due to Silvania and Nandini for being very warmhearted and helpful. I remember with thanks, the help rendered by Florian. I could always count on Peter Somers and Willeke for the dinners at my home. I remember their presence, help in cooking, and of course, the cakes they always brought.

I express my gratitude to ex-officemate Nick van der Valk for his help and support. Sincere gratitude to the past and present members of Optica, Edgar, Arthur, Oana, Wouter, Janne, Cas, Bas, Nitish, Wouter, Wanhua, Morris, Alberto, Sjoerd, Haiyan, Milija, Robert and students for contributing toward the good atmosphere in Optica all the time.

I am grateful to my all time pal Vidya for taking so much interest and enthusiasm in helping me with the cover design of this thesis. Her expertise made the cover design much better than what I had imagined. Let me thank Frank Pasveer for the translation of the propositions and summary.

My stay in Netherlands was enriched with many good Indian friends also. I am indebted to Archana for her friendship and support in all those

matters in which she could help. She has been the person to run into for any help. Thanks to Aravind for the friendship and help during difficult times. I am grateful to Subha, Deepa, Deepu, Jinesh for all the great time and fun we had together. I would like to extend my heartfelt thanks to Gayatri, Padmakumar, Sudarshan, Pappu, Leena, Priti, Arvind, Rajesh Pillai, Krishnamohan, Sheeba and Rajesh for all the good moments we shared. Thanks to Sarita and Thomas for the friendship and entertainment episodes to Sreyas.

I am indebted to my parents, Sukumaran Nair and Chandralekha, for everything I have now. It is the result of their hard work and struggles that made me up to this far. I am unable express my gratitude towards you in words. I am very proud of being your daughter. I remember with gratitude the love and support from my Grandma, Radha. I find myself extremely lucky to have sisters like Deepthi and Rani and equally great brother-in-law, Biju Gopalakrishnan and Jaysankar. Words are not sufficient to express my gratefulness towards them. I am grateful to the families of Jayachandrakumar and Harichandrakumar, my father-in-law, Sreedharan Nair for all the love and support they have given. I wish my mother-in-law, Thankom was with us to see this finished thesis.

I express my gratefulness to my husband Biju for everything. I realize that language is not that powerful enough to express all of the human emotions. Without him I would have never accomplished this. Nothing can be compared to the joy being the mother of my son Sreyas. He cherishes each and every moment of my life.

Reshmi Chakkittakandy
Delft, December 2009.

About the author

Reshmi Chakkittakandy was born on 15 March 1979 in Melady, Kerala (India). She was fascinated by science and physics in particular during her studies in the high school. She obtained her bachelors degree in physics from University of Calicut in 1999 and Masters degree in physics from Cochin University of Science and Technology (CUSAT) in 2001. During her masters studies, her special interests in optics persuaded her to join Master of Technology (M. Tech) in applied optics program at Indian Institute of Technology (IIT) Delhi. She graduated from IIT Delhi in 2004. In 2005, she joined optics research group at Technical University of Delft to pursue PhD research. During this period she was employed by the foundation for fundamental research on matter (Stichting for Fundamenteel onderzoek der Materie(FOM)). The research conducted during her PhD study in Optics group is the basis of this thesis. Various parts of this thesis have been published in refereed journals and presented in many national and international conferences.

List of publications

1. R. Chakkittakandy, J. A. W. M. Corver, P. C. M. Planken, "Terahertz spectroscopy to identify the polymorphs in freeze-dried Mannitol.", J. Pharm. Sci. **99**, 932 (2010).

2. R. Chakkittakandy, J. A. W. M. Corver, P. C. M. Planken, "Quasi-near field terahertz generation and detection.", Opt. Express **16**, 12794 (2008).

3. G. Ramakrishnan, R. Chakkittakandy, P. C. M. Planken, "Terahertz generation from graphite., Opt. Express **17**, 16092 (2009).

4. R. Chakkittakandy, P. C. M. Planken, "Terahertz spectroscopy of amino acids.", in preparation.

Conference contributions

1. R. Chakkittakandy, J. A. W. M. Corver, P. C. M. Planken, "The effects of freeze drying on the polymorphic state of Mannitol studied with THz spectroscopy.", oral presentation, International Workshop on Optical Terahertz Science and Technology 2009 (OTST-2009), Santa Barbara, USA March 7-11, 2009.

2. R. Chakkittakandy, J. A. W. M. Corver, P. C. M. Planken, "Spectroscopy of the polymorphs of D-mannitol using a quasi-near field terahertz generation and detection setup.", oral presentation, Frontiers in optics 2008/Laser Science XXIV, Rochester, USA, October 19-23, 2008.

3. R. Chakkittakandy, P. C. M. Planken, "Quasi-near field terahertz time domain spectroscopy.", oral presentation, 33 rd International Conference on Infrared, Millimeter, and Terahertz Waves (IRMMW-THz), California, USA, Sept 15-19, 2008.

4. R. Chakkittakandy, J. A. W. M. Corver, P. C. M. Planken, "Quasi-near field terahertz generation and detection.", poster presentation, 2nd Medical Delta conference, Delft, The Netherlands, May 23, 2008.

5. R. Chakkittakandy, P. C. M. Planken, "Quasi-near field terahertz generation and detection.", oral presentation, EOS Topical meeting on Photonic devices, Utrecht, The Netherlands, March 31- April 02, 2008.

6. G. Ramakrishnan, R. Chakkittakandy, P. C. M. Planken, "Terahertz generation from graphite.", oral presentation, 34th International Conference on Infrared, Millimeter, and Terahertz Waves (IRMMW-THz), Busan, Korea, Sept 21-25, 2009.